Schweizerische Eidgenossenschaft
Confédération suisse
Confederazione Svizzera
Confederaziun svizra

Federal Department of the Environment, Transport, Energy and Communications DETEC

Swiss Federal Office of Energy SFOE
Energy Research and Cleantech Division

Final report dated 13.05.2022

REAL

Research on Alternative Combustion Concepts for Efficient Gas Engines

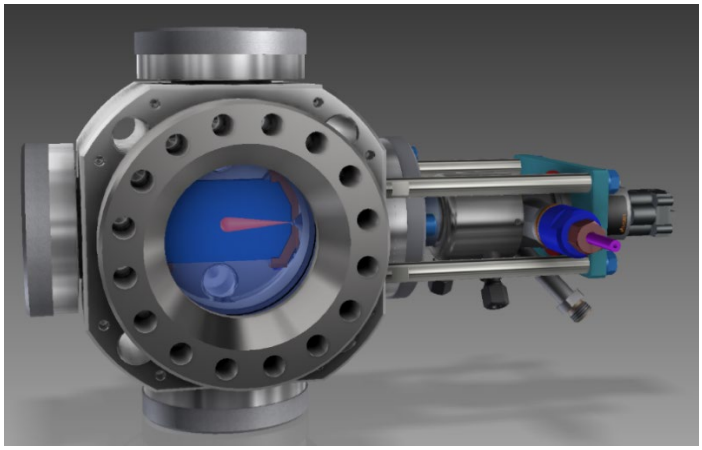

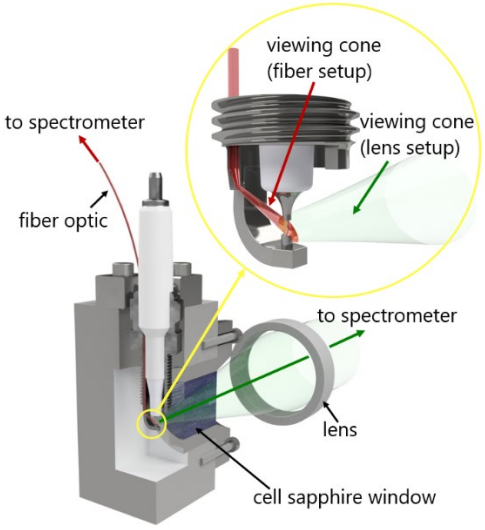

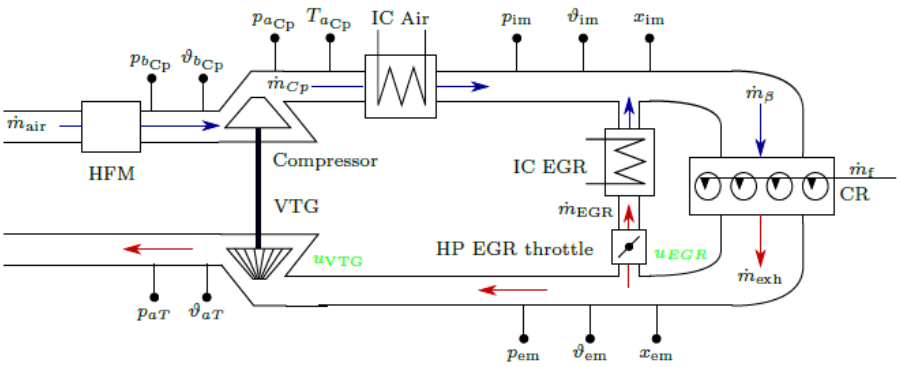

Source: ETH LAV, ETH IDSC, Empa

Date: 13.05.2022

Location: Bern

Publisher:
Swiss Federal Office of Energy SFOE
Energy Research and Cleantech
CH-3003 Bern
www.bfe.admin.ch

Co-financing:
FVV | Forschungsvereinigung Verbrennungskraftmaschinen e.V.
Lyoner Straße 18, 60528 Frankfurt am Main, Germany
http://www.fvv-net.de

DFG | Deutsche Forschungsgemeinschaft e.V.
Kennedyallee 40, 53175 Bonn, Germany
www.dfg.de

Subsidy recipients:
Empa, Automotive Powertrain Technologies Laboratory
Überlandstrasse 129, CH-8600 Dübendorf
www.empa.ch/abt504
www.empa.ch/web/s504

ETH, Institute for Dynamic Systems and Control (IDSC)
Sonneggstrasse 3, CH-8092 Zürich
idsc.ethz.ch

ETH, Aerothermochemistry and Combustion Systems Laboratory (LAV)
Sonneggstrasse 3, CH-8092 Zürich
ipe.ethz.ch

Authors:
Patrik Soltic, Empa, patrik.soltic@empa.ch
Laura Merotto, Empa, laura.merotto@empa.ch
Walter Vera-Tudela, LAV ETH
Christophe Barro, LAV ETH
Davide Sakellarakis, LAV, ETH
Yuri Wright, LAV ETH, ywright@ethz.ch
Severin Hänggi, IDSC ETH, shaenggi@idsc.mavt.ethz.ch

SFOE project coordinators:
Carina Alles, carina.alles@bfe.admin.ch
Luca Castiglioni, luca.castiglioni@bfe.admin.ch

SFOE contract number: SI/501755-01

The authors bear the entire responsibility for the content of this report and for the conclusions drawn therefrom.

Schweizerische Eidgenossenschaft
Confédération suisse
Confederazione Svizzera
Confederaziun svizra

Federal Department of the Environment, Transport, Energy and Communications DETEC

Swiss Federal Office of Energy SFOE
Energy Research and Cleantech Division

Zusammenfassung

Methan ist ein hervorragender Treibstoff für Verbrennungsmotoren. Er ist sehr klopffest und unbedenkliche Schadstoffemissionsniveaus sind mit weniger komplexem Abgasnachbehandlungsaufwand realisierbar als bei Kohlenwasserstoffen mit langkettiger oder zyklischer Struktur. Fossiles Erdgas hat, aufgrund seines höchsten Wasserstoffanteiles aller Kohlenwasserstoffe, bereits einen deutlichen CO_2 Vorteil gegenüber Benzin oder Diesel. Zudem kann Methan, was für zukünftige Anwendungen besonders wichtig ist, vergleichsweise einfach und wirtschaftlich aus erneuerbaren Quellen erzeugt werden.

Heutige Serien-Gasmotoren basieren üblicherweise auf Benzinmotoren im PW-Bereich oder auf Dieselmotoren im LKW- sowie Stationär-Bereich und sind nur bedingt auf die Eigenschaften von Methan angepasst. Stand der Technik ist die vorgemischte Verbrennung von Methan, gezündet mit einem klassischen induktiven Zündsystem. Im Rahmen dieses Projektes werden neue Zünd-, Brenn- und Regelungsverfahren erforscht welche Grundlagen für eine Entwicklung von effizienteren und schadstoffarmen Gasmotoren in verschiedensten Anwendungen ermöglichen. Entsprechend viel Wert wurde im Projekt auch auf wissenschaftliche Veröffentlichungen gelegt.

Das Projekt ist in drei Arbeitspakete (WP) gegliedert: WP1 behandelt neue Zündverfahren sowie spektroskopische Methoden zur Diagnostik, WP2 behandelt regelungstechnische Aspekte von Abgasrückführung (AGR) mit Fokus auf transienten Motorbetrieb und WP3 behandelt Grundlagen der Gemischbildung und Verbrennung inklusiv der Betrachtung von diffusionskontrollierten Prozessen.

Das Schlüsselelement zur Effizienzsteigerung bei Gasmotoren ist die Realisierung einer dieselähnlichen Verbrennung, welche durch Verdünnung (Luftüberschuss oder AGR) in Kombination mit hohen Verdichtungsverhältnissen charakterisiert wird. Bleibt man bei gut vorgemischten Systemen ist die Verdünnung für fremdgezündete Systeme sehr anspruchsvoll. Einerseits ist die Zündung selbst schwierig und andererseits muss die Verdünnung sehr genau kontrolliert werden damit, besonders im transienten Betrieb, keine Verbrennungsaussetzer erfolgen. Verlässt man den klassischen Ansatz der gut vorgemischten Systeme sind die in-Zylinder Gemischbildung (Strahlphysik, Ladungsbewegung, Diffusion) sowie die Selbstzündungseigenschaften von essentieller Bedeutung.

Im Bereich der Zündverfahren (WP1) zeigte ein Nanosekunden-Zündsystem, welches in verschiedenen Versuchsträgern (inkl. einem Vollmotor) eingesetzt wurde, deutliche Vorteile bei der Zündung verdünnter Gemische. Durch die Zündung mittels extrem kurzer repetitiver Pulse, welche sogenannte nicht-thermische Plasmen erzeugen, können solche schwer entflammbare Gemische robust gezündet werden. Für die Erforschung der Flammausbreitung bei Nanosekunden-Zündung konnten aussagekräftige Versuche an einer Zündungszelle sowie an einer optisch zugänglichen Vorkammer durchgeführt werden. Vergleichende Untersuchungen haben gezeigt welche Pulsenergien, welche Anzahl von Pulsen sowie welche Pulswiederholfrequenz eine vorteilhafte Flammkernentwicklung unter verdünnten Bedingungen ermöglichen. Die erarbeiteten Grundlagen geben neue Freiheitsgrade für die Auslegung zukünftiger effizienterer Verbrennungssysteme. Im Rahmen des Projektes wurden zudem minimalinvasive spektroskopische Methoden entwickelt um Informationen über die Gemischzusammensetzung aus der Lichtemission des gepulsten nicht-thermischen Plasmas zu extrahieren. Diese Methodik kann für die zukünftige Gemischbildungsauslegung ein wichtiges Werkzeug sein. Zudem konnte das elektrische System modelliert und validiert werden, inklusive eines neuen Ansatzes für die Detektion einer erfolgreichen Zündung.

Im Bereich der Ladungsverdünnung (WP2) wurde im Projekt Grundlagen zur modellprädiktive Regelung der Abgasrückführung erarbeitet. Abgasrückführung kann hochdruck- und/oder niederdruckseitig des Turboladers erfolgen. Beide Rückführpfade unterscheiden sich sehr in Bezug auf Dynamik sowie Linearität, wie auch bezüglich ihrer Anwendbarkeit je nach Motorbetriebspunkt. Die Anwendung einfacher und etablierter (d.h. single-input/single-output) Regelungsverfahren ist hier nicht zielführend. Solche einfachen Ansätze berücksichtigen einerseits Querkopplungen nicht und führen dadurch zu grossen Abweichungen. Andererseits bedürfen sie einem enormen experimentellen Anpassungsaufwand und sind praktisch nicht von einem Motor auf einen anderen übertragbar. Im Rahmen dieses Projektes wurden deshalb erfolgreich modellprädiktive Ansätze entwickelt und an

verschiedenen Versuchsträgern validiert welche die physikalischen Zusammenhänge in den Luft- und Abgaspfaden berücksichtigen und eine sehr gute Regelungsgüte mit minimalem Anpassungsaufwand ermöglichen.

Für die Hochdruckgaseinblasung wurden in WP3 umfangreiche Untersuchungen durchgeführt in der Hochdruck-Hochtemperatur-Zelle unter nichtreaktiven als auch bei selbstzündenden Bedingungen. Hierzu gelangte ein Prototypen-Injektor zum Einsatz in Kombination mit einem Druckverstärker, welcher maximale Einspritzdrücke bis 500 bar ermöglichte. Die Spraymorphologie wurde experimentell mittels bildgebenden Schlieren Verfahren für zahlreiche Einspritz- und Gegendruck-kombinationen charakterisiert; mittels Tracer-LIF konnten ausserdem quantitative Verteilungen der Kraftstoffkonzentration gemessen werden. Die Verwendung einer Vorverbrennung gestatte es auch selbstzündende Bedingungen zu erreichen. Parallel dazu wurden Simulationsverfahren für die Hochdruck-Gaseinblasung bei motorischen Bedingungen entwickelt und anhand der Experimente ausgiebig validiert. Dabei stellte sich die Berücksichtigung des Realgasverhaltens als absolut zentral heraus für die korrekte Vorhersage des Eindringverhaltens des Sprays, des Mischungsfelds und auch bzgl. der für die Zündung wichtige Temperaturverteilung.

Summary

Methane is an excellent fuel for internal combustion engines. It is very knock resistant and harmless pollutant emission levels can be achieved with less exhaust gas aftertreatment effort than with hydrocarbons which have a long-chain or a cyclic structure. Fossil natural gas, due to its highest hydrogen content of all hydrocarbons, already has a significant CO_2 advantage over gasoline or diesel. In addition, methane, which is particularly important for future applications, can be produced comparatively easily and economically from renewable sources.

Today's series-produced gas engines are usually based on gasoline engines in the passenger car sector or on diesel engines in the truck and stationary sectors and are only adapted to the properties of methane to a limited extent. State of the art is the premixed combustion of methane, ignited with a classical inductive ignition system. Within the framework of this project, new ignition, combustion and control processes are being researched which will provide the basis for the development of more efficient and low-emission gas engines in a wide range of applications. Accordingly, great importance was given to scientific publications.

The project is divided into three work packages (WP): WP1 deals with new ignition processes as well as spectroscopic methods for diagnostics, WP2 deals with control aspects of exhaust gas recirculation (EGR) with a focus on transient engine operation, and WP3 deals with fundamentals of mixture formation and combustion including the consideration of diffusion-controlled processes.

The key element to increase efficiency in gas engines is the realization of a diesel-like combustion, which is characterized by dilution (excess air or EGR) in combination with high compression ratios. Staying with well-premixed systems, dilution for spark-ignited systems is very challenging. On the one hand, ignition itself is difficult and, on the other hand, dilution must be very precisely controlled to avoid combustion misfires, especially in transient operation. Leaving the classical approach of well-premixed systems, the in-cylinder mixture formation (jet physics, charge motion, diffusion) as well as the auto-ignition properties are of essential importance.

In the field of ignition processes (WP1), a nanosecond ignition system, which was used in different test vehicles (including a full engine), showed clear advantages in the ignition of diluted mixtures. Ignition by means of extremely short repetitive pulses, which generate so-called non-thermal plasmas, enables robust ignition of such mixtures that are difficult to ignite. For the investigation of flame propagation with nanosecond ignition, meaningful experiments could be carried out on an ignition cell as well as on an optically accessible prechamber. Comparative investigations have shown which pulse energies, which number of pulses as well as which pulse repetition frequency enable an advantageous flame

core development under diluted conditions. The project also developed minimally invasive spectroscopic methods to extract information about the mixture composition from the light emission of the pulsed non-thermal plasma. This methodology can be an important tool for future mixture formation design. In addition, the electrical system could be modeled and validated, including a new approach for the detection of successful ignition.

In the field of charge dilution (WP2), the project developed basic principles for model-predictive control of exhaust gas recirculation. Exhaust gas recirculation can take place on the high-pressure and/or low-pressure side of the turbocharger. Both feedback paths differ greatly in terms of dynamics and linearity, as well as in terms of their applicability depending on the engine operating point. The application of simple and established (i.e. single-input/single-output) control methods is not expedient here. On the one hand, such simple approaches do not consider cross-couplings and thus lead to large deviations. On the other hand, they require an enormous experimental adaptation effort and are practically not transferable from one engine to another. Within the scope of this project, model predictive approaches were therefore successfully developed and validated on various test vehicles, which take into account the physical interrelationships in the air and exhaust gas paths and enable very good control quality with minimal adaptation effort.

For high-pressure gas injection, extensive investigations were carried out in WP3 in the high-pressure, high-temperature cell under non-reactive as well as self-igniting conditions. For this purpose, a prototype injector was used in combination with a pressure booster, which allowed maximum injection pressures of up to 500 bar. The spray morphology was characterized experimentally by means of imaging Schlieren techniques for numerous injection and backpressure combinations; tracer LIF was also used to measure quantitative distributions of fuel concentration. The use of precombustion also allowed self-igniting conditions to be achieved. In parallel, simulation procedures for high-pressure gas injection at engine conditions were developed and extensively validated on the basis of experiments. The consideration of the real gas behavior turned out to be absolutely central for the correct prediction of the spray penetration behavior, the mixing field and also with regard to the temperature distribution, which is important for ignition.

Main findings

The main findings are structured along the three major work packages of the project and are as follows.

WP1 (Ignition process investigations, including experiments on a multi-cylinder engine):

- A comprehensive characterization of the nanosecond repetitively pulsed discharge (NRPD) was performed to characterize the influence of pulse rise rate and pulse duration. These findings enable assessing the parameters for optimizing the ignition process.
- The factors affecting the breakdown have been understood. This has allowed the development of a strategy for ignition success prediction based on the breakdown voltage.
- It could be shown that NRPD ignition extends the ignition limits for EGR diluted mixtures in a constant volume cell configuration.
- Tests on a four-cylinder engine using a classical inductive ignition system show stable ignition until λ=1.6.The engine test bench was successfully adapted for NRPD ignition with a 4-channels pulse generator.
- NRPD allows a reliable ignition (no misfire) of very lean mixtures (λ above 2) and high EGR dilution (35%).
- Higher pulse repetition frequency results in higher combustion stability, lower ignition timing, and faster inflammation.
- NRPD ignition has been experimentally investigated on the engine testbench with different sparkplugs geometries in diluted conditions (both EGR and Air dilution).

WP2 (Model predictive control of EGR, including experiments on multi-cylinder engines):

- A systematic and generic approach for air path control based on nonlinear model predictive control and grey-box models of individual air path components was successfully developed.
- Tthe efficiency-optimal tracking of intake manifold gas conditions for an air path with dual-loop EGR could be demonstrated.
- Superior control performance compared to a linear control approach could be experimentally validated on a heavy-duty engine.

WP3 (Optical an Numerical Investigations):

- Non-reactive and auto-igniting underexpanded jets could be expermentaly characterized in an optically accessible constant volume combustion cell for a wide variety of conditions. For certain combinations of injection/back pressure ratios re-condensation of the gaseous was observed. At engine relevant conditions, such effects were found to be irrelevant.
- Computational reactive fluid dynamics simulations of underexpanded jets were carried out for a wide range of conditions and validated by means of the optical experimental data. Taking into account real-gas effects proved to be instrumental for accurate predictions and a corresponding framework was developed showing very good agreement.
- In the field of optical diagnostics of premixed flame development, robust ignition in pre-chamber in leaner conditions is obtained when standard inductive ignition is replaced by NRPD.

Contents

Abbreviations

BMEP	Brake Mean Effective Pressure
CFD	Computational Fluid Dynamics
CMC	Conditional Moment Closure
CNG	Compressed Natural Gas
COC	Center of Combustion
COV	Coefficient of Variance
CVC	Constant Volume Cell
DEG	Delay Generator
EGR	Exhaust Gas Recirculation
Empa	Eidgenössische Materialprüfungs- und Forschungsanstalt
ETH	Eidgenössische Technische Hochschule
FOSP	Fiber-Optic Spark Plug
IDSC	Institute for Dynamic Systems & Control of ETH
IMEP	Indicated Mean Effective Pressure
LAV	Aerothermochemistry and Combustion Systems Laboratory of ETH
MPC	Model Predictive Control
NMPC	Nonlinear Model Predictive Control
NRPD	Nanosecond Repetitively Pulsed Discharge
OPC	Optical Pre-chamber
PRF	Pulse Repetition Frequency
RANS	Raynolds-Averaged Navier Stokes
RCEM	Rapid Compression and Expansion Machine
RCP	Rapid Control Prototyping
SIBS	Spark Induced Breakdown Spectroscopy
SST	Shear Stress Transport

1 Introduction

1.1 Background information and current situation

Natural gas is an important primary energy carrier for the power industry since combined-cycle power plants are highly efficient and natural gas is widely available at comparably low costs. Natural gas is also an attractive fuel for decentralized power and heat generation using stationary internal combustion engines as the primary energy converters. For marine applications, liquefied natural gas has become an important fuel in recent years [1], mainly because it is an ideal fuel to fulfil pollutant emission regulations that are in place in certain sea areas and such gas is available worldwide. As natural gas, with its main component methane, has the lowest carbon content of all fossil sources, its direct CO_2 burden is comparably low. Additionally and importantly, natural gas can be blended by any amount with renewable methane, which can be produced for example in biogas- or power-to-gas plants [2]. This makes natural gas an attractive fuel for all applications with exergy-demand and which face high pressure to reduce CO_2. One sector which is strongly affected by increasingly stricter CO_2 regulations is the highly relevant mobility sector where renewable methane as a fuel in classical or hybrid powertrains can have an ecologic and economic long-term perspective, as pure electrification does not necessarily lead to advantages for all use cases [3][4]. Non-fossil solutions for the very demanding heavy-duty on- and off-road applications, shipping and air traffic are important to be deployed over the next few centuries [5] in order to contribute to net zero greenhouse gas goals. Also in the power sector, decentralized conversion of methane to power and heat is very likely to be amongst the best solution in a future electricity grid with high shares of fluctuating renewables [6]. Therefore it is very likely, that methane (possibly also in a blended for with hydrogen for certain applications) will play an important role in the future energy, mobile machinery and mobility system

Natural gas as a vehicle fuel is established in many regions and current statistics indicate that more than 28 million natural gas vehicles are in operation, with strong growth rates worldwide [7]. The Swiss gas industry has invested in a re-fueling infrastructure with more than 140 CNG filling stations and provides at least 20% renewable methane so that methane-powered vehicles are also a viable approach to reduce, or even omit, CO_2 emissions for the Swiss situation. However, as renewable chemical energy carriers are precious, an efficient use is essential from an ecological as well as from an economical point of view.

1.2 Purpose of the project

Most of todays mass-produced natural gas engines are adapted gasoline or diesel engines. Typical adaptations are adjusted compression ratios to meet the knock resistance of methane, increased boost pressure levels to compensate for the reduced volumetric efficiency of the gaseous fuel, as well as adapted valves, valve seats and turbine materials to cope with increased temperature levels. Those adaptations do not exploit the full potential of methane as an alternative fuel. This project aims at expanding the knowledge on possibilities to enhance efficiency levels and to reduce pollutant emissions for methane-fueled engines. This is done in close cooperation of different research groups working on numerical and experimental research on combustion fundamentals (LAV ETH), ignition fundamentals (Empa) and control (IDSC ETH).

1.3 Objectives

The classical approach for methane combustion in on-road engines is the spark ignition of a premixed stoichiometric methane-air-mixture using an inductive ignition system. To increase efficiency, diesel-like process parameters would be favorable which means lean combustion in combination with a high compression ratio. However, lean combustion of a very stable (and therefore hard-to-ignite) fuel as methane is not a straightforward task. To trigger combustion in a controlled and predictable way and to establish a robust flame which then propagates fast through the cylinder are the main challenges. For this task in challenging conditions, alternatives to the classical spark plug, placed in the open combustion chamber, have to be used. One alternative is to inject a small amount of a high reactivity fuel such as diesel oil, DME or OME which is compression-ignited and which then triggers then the combustion of the premixed diluted methane-air mixture [8][9]. Another approach is to use a pre-chamber with gas injection and to decouple the flow and stoichiometry of the main- and of the pre-chamber [10][11][12]. Both approaches proved to have a large efficiency-increase-potential. However, as long as the premixed charge is diluted with air, the excess air prevents the use of established exhaust gas aftertreatment technologies for the unburnt hydrocarbons. This can be overcome with a dilution using exhaust gases instead of air while remaining at premixed stoichiometric conditions [13] or with the avoidance of premixed combustion. Both paths are examined within this project. Additionally, alternatives to the classical inductive ignition systems are investigated. This, with the following objectives:

- Understand the fundamental aspects of spark ignition with special focus on innovative non-thermal ignition systems using nanosecond repetitive pulsing, (WP1, Empa and WP3, LAV).
- Find ignition systems, which are able to initiate a robust flame propagation in premixed lean mixtures, with special focus on EGR-dilution, (WP1, Empa and WP3, LAV).
- Find spectroscopic methods for the quantification of the relevant conditions around the spark plug, (WP1, Empa).
- Find ways to precisely control the amount of EGR, also under highly transient load conditions, (WP2, IDSC).
- Understand the fundamentals of diffusion-controlled methane combustion using high-pressure direct injection, both with numerical and experimental methods (WP3, LAV).

2 Procedures and methodology

2.1 WP1: Electrical Ignition Methods

2.1.1 Ignition Cell

In a previous project, an optically accessible ignition cell was set up with which ignition spark spectroscopy (Spark Induced Breakdown Spectroscopy, SIBS) can be operated. It could be shown that the local air-fuel equivalence ratio (λ) of the spark plug can be derived from the spectral signal using SIBS on classical inductive ignition systems for methane/air mixtures [14]–[16]. Figure 1, left, shows the ignition cell with spectral emissions measurements via a lens system.

Within the framework of this project, the ignition cell was expanded to allow precise gas mixtures to be filled with several components. The gas supply was equipped with corresponding cylinders, lines and mass flow controllers (Figure 1, right), including the possibility for operation with inert gases simulating exhaust gas recirculation. In addition, the test bench has been adapted so that it is now possible to preselect mixture compositions and final pressure, and the system then fills the cell automatically.

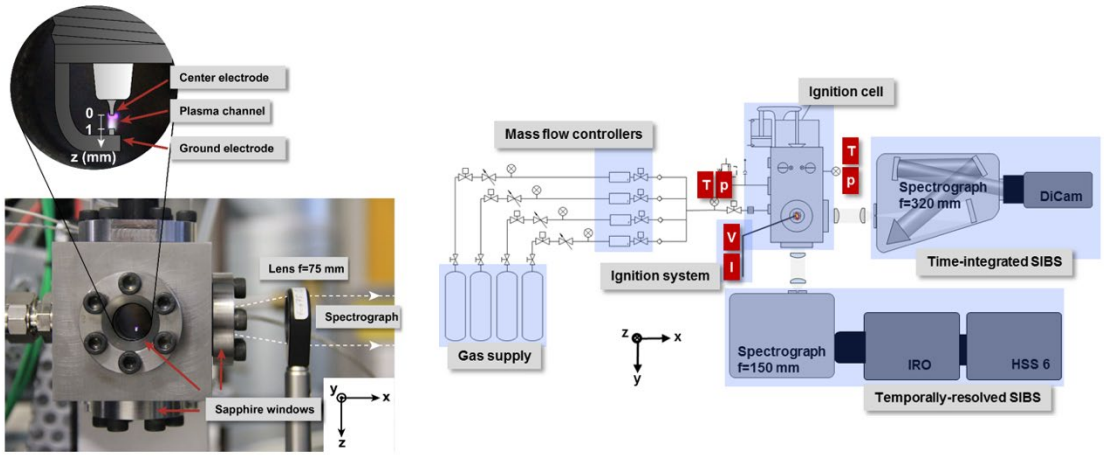

Figure 1: Left: optically accessible ignition cell used for quiescent conditions SIBS tests. Right: sketch of the test bench structure.

This SIBS measurement technology, in addition to classical ignition systems with so-called thermal plasmas, was adapted for operation with an alternative ignition system using non-equilibrium plasmas (nanosecond ignition). With this aim, a nanosecond pulse generator (FID 15-10NK) was acquired to be used to generate high-energy discharges at 10 kHz repetition rate. The device delivers Nanosecond Repetitively Pulsed Discharge (NRPD), resulting in a non-thermal plasma ignition. To extend the SIBS applicability to NRPD ignition, a modification of the test bench configuration was performed to ensure simultaneous control of several sensors/devices responding with different times. With this aim, a Berkley Nucleonics 577 delay generator (DEG) with 8 Channels (250ps Delay & Width Resolution & 50 ps Internal Channel to Channel Jitter) was integrated in the configuration. The Control Unit generates a signal that triggers the DEG. The DEG sends the selected pattern of triggering signals to the nanosecond-pulser for sparking, and to the camera for image acquisition. Therefore, the ignition system and the camera are triggered independently and with a known and adjustable starting time, thus allowing a precise control of the timing of all the events.

An alternative system of light extraction via fiber optic cables embedded in the spark plug was previously tested in the INSIDE setup. In principle, this can also be used in a running engine. Within the framework of the REAL project, a non-resistive fiber-optics equipped spark plug (FOSP, Figure 2) was designed and manufactured to be used with NRPD ignition systems.

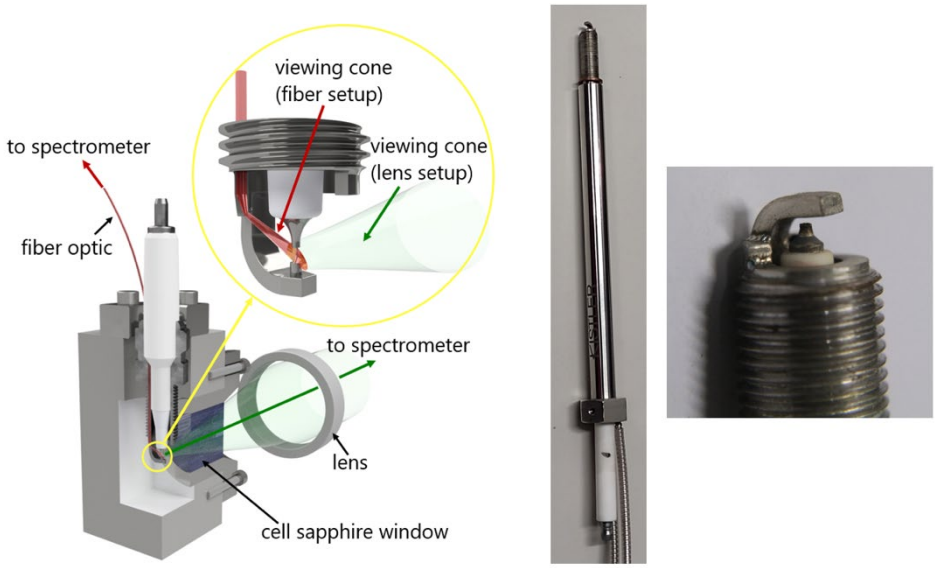

Figure 2: Fiber-optics equipped spark plug (FOSP) to be used with NRPD ignition. Schematics of the spectral acquisition (left) and pictures of the spark plug used (right).

Towards the end of the project, the ignition cell setup was used for the electrical characterization of the NRPD discharge (see Section 3.1.1) and for preliminary testing of the newly acquired 4-channel pulse generator needed for engine testing presented in Section 2.1.2.

2.1.2 Full engine

The full engine is based on a Volkswagen EA288 diesel engine but with a completely redesigned cylinder head as well as a redesigned air-path, exhaust path, turbocharger and pistons. As shown in Figure 3, the cylinder head can hold inserts for a classical spark plug (green). Alternatively, this insert can be changed for a pre-chamber insert (not shown here and not part of this project). As Figure 3 also shows, the piston is designed with a hemispheric bowl, which is regarded to be optimal for premixed combustion concepts in an engine setup with a flat roof.

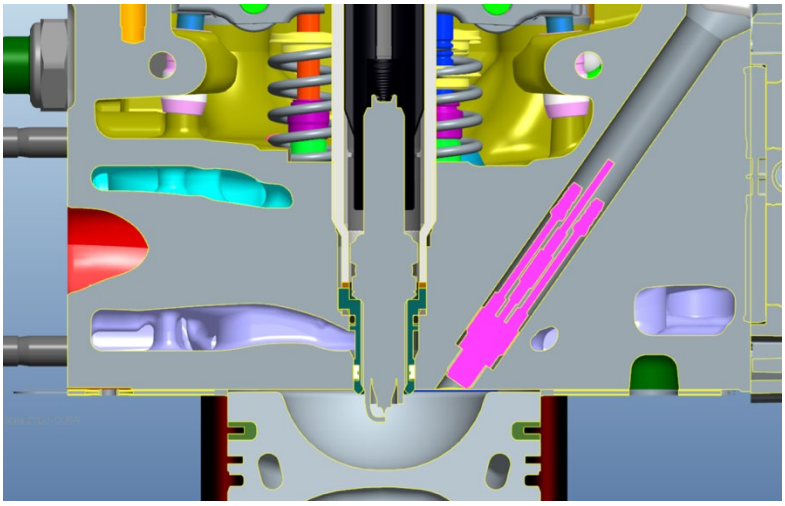

Figure 3: Rendering of the engine's combustion chamber configuration
(including the central spark plug insert and the cylinder pressure sensor).

Additionally, a high- and a low-pressure EGR path was built-up. Figure 4 shows a schematic of the engine setup; Figure 5 shows the corresponding pictures. The engine is mounted on a state-of-the art transient engine test bench, including conditioning of the engine / intercooler / EGR and certification-grade exhaust gas analysis (Horiba Mexa One).

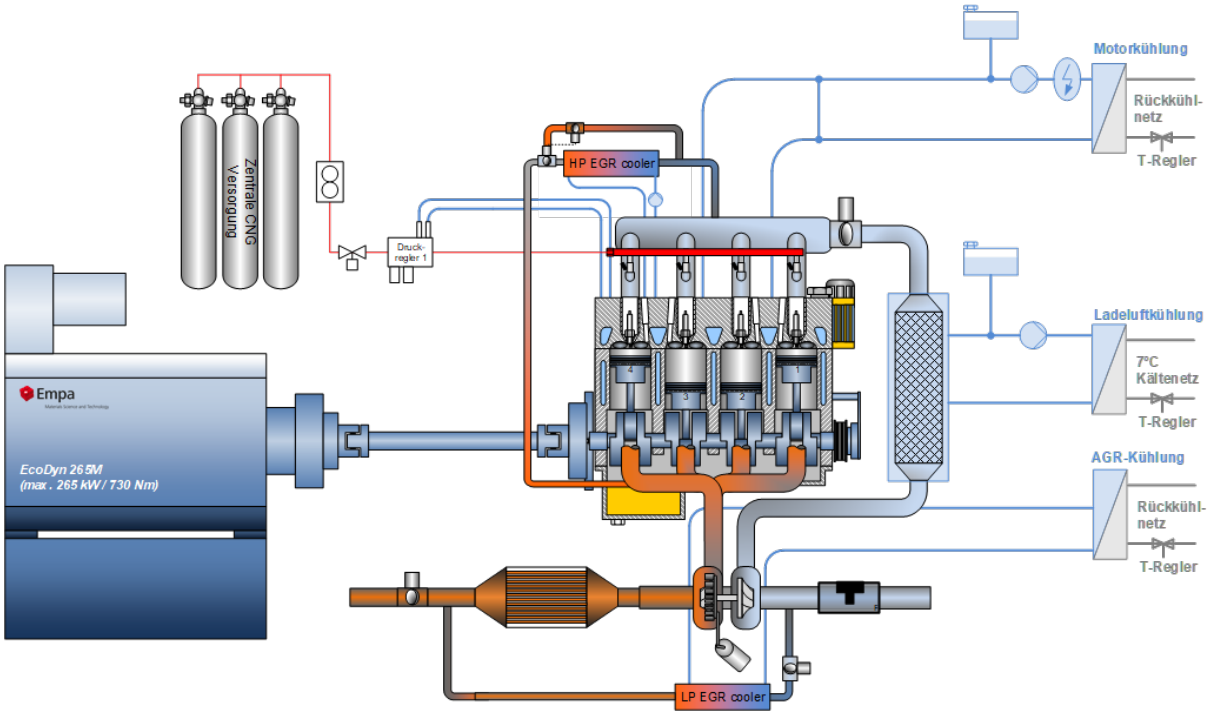

Figure 4: Schematic of the engine's setup at the test bench.

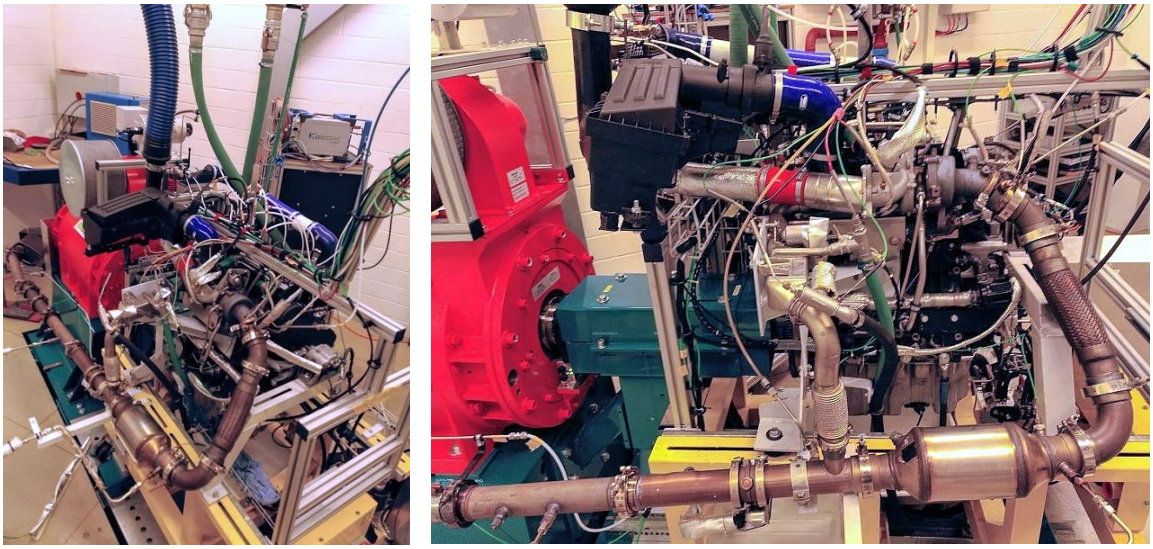

Figure 5: Pictures of the engine in its basic setup with classical ignition.

The engine setup was adapted for operation with a NRPD system. A 4-channel pulse generator (Megaimpulse NPG18N14) was acquired, which is able to deliver short pulses (<10 ns duration at 50%, rise time < 4 ns) with energy up to 30 mJ per pulse and a maximal repetition frequency of 100kHz. The engine control system was adapted to control the 4-channel NRPD system. Unfortunately, sparkplugs used with inductive ignition systems cannot be used directly with the NRPD ignition due to their electrical characteristics: Most OEM sparkplugs are fitted with a resistor to reduce the discharge's radio frequency interference. Using such sparkplugs with NRPD won't work because the very short energy pulses would be reflected at the resistor. Therefore new sparkplugs connectors and insert were designed and modified to fit the engine geometry while ensuring negligible electrical resistance to the nanosecond discharge and adequate insulation and electromagnetic shielding. The engine setup, including the 4-channel pulse generator, is shown in Figure 6. Figure 7 shows the pulse generator (left) and the geometry of the new spark plug (right).

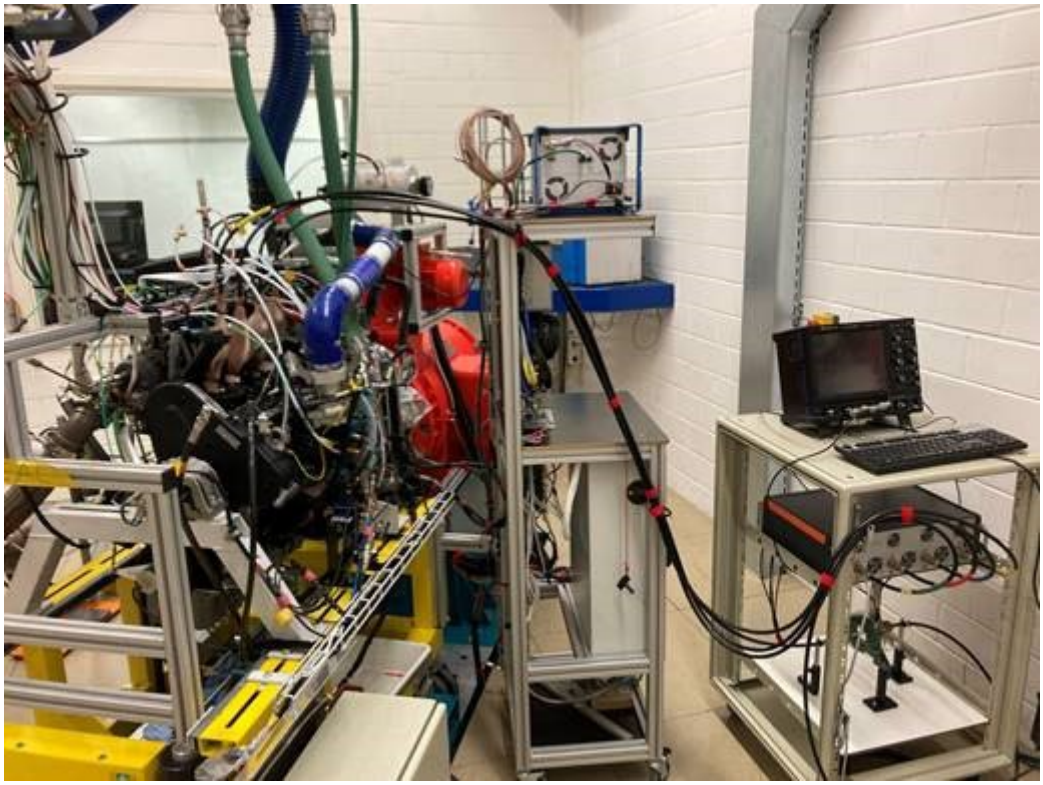

Figure 6: Engine setup with 4-channel pulse generator for NRPD ignition.

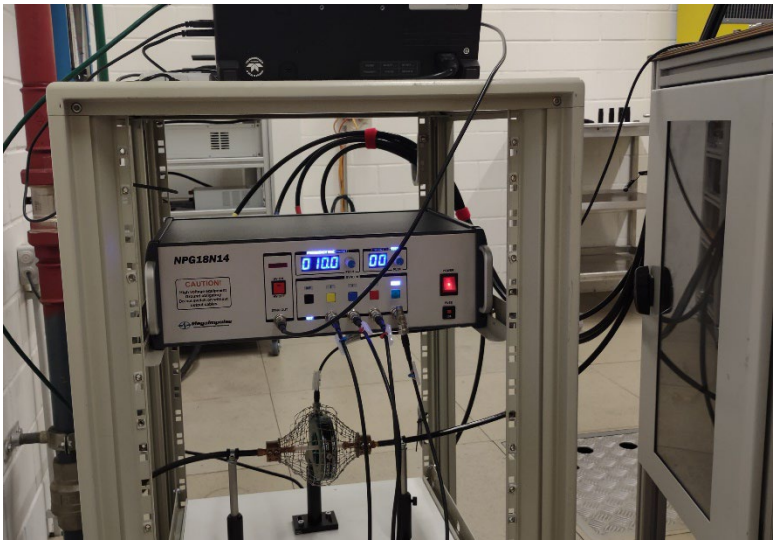

Figure 7: Detail of the 4-channel pulse generator (left) and the spark plug designed for the engine setup (right).

2.2 WP2: EGR Control

2.2.1 Broader Context

Reducing greenhouse gas emissions and preserving air quality in the face of a steadily growing economy and world population are the challenges of the coming decades. For the mobility sector, the main measures proposed are the introduction of new powertrain technologies as well as the further development of existing technologies in combination with the introduction of alternative fuels. Since there are still no competitive alternatives to the internal combustion engine for a large number of high-power mobility applications, its further development in terms of efficiency, pollutant emissions and fuel flexibility will continue to play an important role for climate targets and air quality. Additionally, combined heat and power production as well as fast-reacting combustion-based emergency generators are likely to gain on importance.

Besides the exhaust gas aftertreatment, the engine downsizing and the recirculation of exhaust gas are two efficiency-enhancing and emission-reducing measures that have been introduced in gasoline and diesel engines in recent decades in all mobility sectors. Together with various coolers, these are used to set the gas conditions (pressure, temperature and oxygen concentration) in the intake manifold, which themselves define the gas conditions in the cylinder during the combustion process and thus have a decisive impact on emissions and efficiency.

In order to precisely control these conditions in transient operation, the air paths in today's engines are highly complex and diverse. Depending on the application, they can consist of several EGR paths and turbochargers, often with either a waste gate or a variable turbine geometry (VTG). Due to the numerous actuators present and the complexity and nonlinear behavior of individual components, the control of the intake manifold gas conditions poses a challenge. The standard approach in industry is to use a system of proportional-integral-derivative (PID) controllers, which are tuned with extensive calibration effort on an engine test bench for every operation point individually. In near future, the need for a further reduction in pollutant emissions and the need for a certain fuel flexibility is expected to additionally increase the calibration effort. Given these developments, a systematic control approach suited for such complex systems could offer significant benefits in terms of engine performance as well as engine calibration.

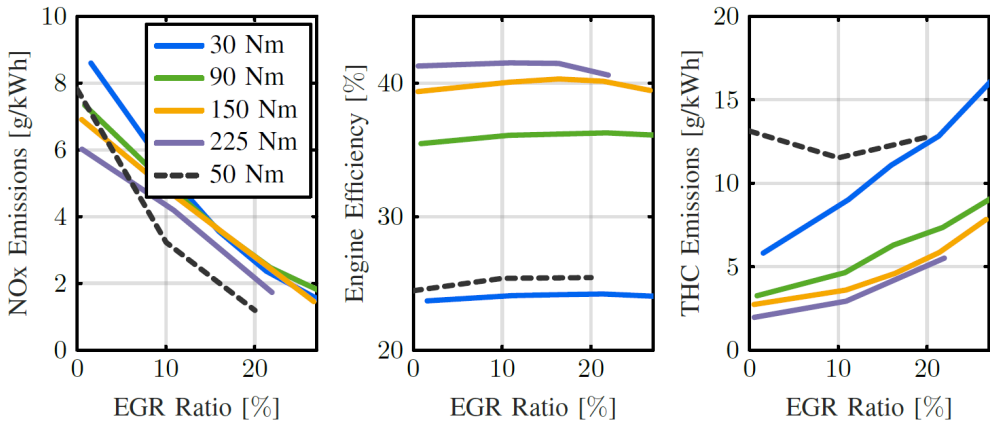

Figure 8: Effects of EGR on engine-out pollutant emissions and engine efficiency, measured once with the full engine (see Section 2.1.2) equipped with a standard ignition system at stoichiometric operation and a speed of 1500 rpm (solid lines), and once with a diesel ignited CNG engine of the same size at stoichiometric operation and a speed of 1400 rpm (dashed lines).

The application of EGR in today’s compressed natural gas (CNG) engines offers a limited potential compared to the diesel or gasoline engine. Figure 8 shows that with a standard ignition system, the

recirculation of exhaust gas can significantly reduce NO_x emissions while increasing the engine efficiency, but at the expense of hydrocarbon emissions. However, experimental results from a diesel-ignited CNG research engine of ETH IDSC show that with an increase of the ignition energy, hydrocarbon emissions do not increase, but can even be reduced with the application of EGR[1].

2.2.2 Work Package Objectives and Challenges

The main objective of ETH IDSC within the REAL project is the development of a novel control algorithm, which allows to precisely and dynamically set the intake manifold gas conditions of an internal combustion engine. This algorithm has to be applicable to various engines with different air path structures and actuators. It has to be a systematic and intuitive approach, which requires very low calibration effort. For engine air paths that offer multiple possibilities to set the intake manifold gas conditions, the control algorithm further has to find the best possibility based on additional control objectives such as the improvement of the engine efficiency or pollutant emissions.

While the algorithm that is developed within the project is formulated in a generic way and can be applied to a variety of control problems, the focus concerning its application was set to the control of air paths that consist of a turbocharger and multiple EGR paths. This corresponds to the air path layout of the full engine at Empa and the one of the light-duty engine at ETH IDSC as described and illustrated in Section 2.2.3. The control of such a setup offers a considerable number of challenges:

- The oxygen concentration in the intake manifold can either be derived with low-pressure or high-pressure EGR (overactuated system). The control algorithm has to be able to find a strategy that optimally combines these two paths in terms of engine efficiency (see Figure 9, left).
- The derivation of control strategies for overactuated systems requires precise knowledge of the system behaviour.
- The application of high-pressure EGR reduces the enthalpy flow through the turbine of the turbocharger and thus considerably affects the intake manifold gas pressure. Hence, in an air path consisting of a high-pressure EGR path and a turbocharger, the intake manifold gas pressure and oxygen concentration are highly coupled (see Figure 9, right).
- Nearly all air path components have a highly nonlinear behaviour.
- The gas transport though the components of the air path introduces time delays, which cannot be neglected.
- The resulting algorithm has to be real-time capable and updated within short time intervals (In order to be able to react to changes in the reference values and disturbances, it has to be re-evaluated within 50ms or less.).

[1] The general level of the hydrocarbon emissions is higher for the diesel-ignited CNG engine because the engine geometry is not optimized for the CNG combustion, as it is the case for the full engine.

- Various system limits, such as a maximum turbocharger speed or a minimum air-to-fuel ratio have to be considered within the control algorithm.

Signal	Unit	HP EGR	LP EGR
Intake pressure	bar	1.34	1.35
Intake temperature	°C	45	45
Burnt-gas ratio	%	4.6	5.0
Exhaust pressure	bar	2.03	1.92
IMEP gas exchange	bar	−0.86	−0.74
IMEP combustion	bar	4.29	4.23
Engine efficiency	%	23.6	24.7

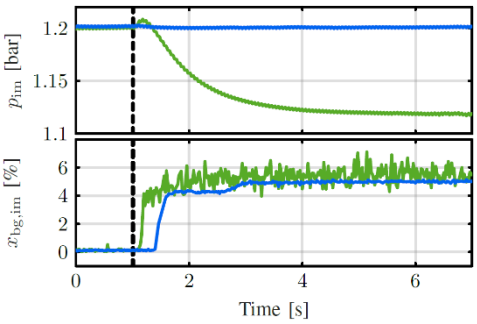

Figure 9: Steady-State (left) and dynamic (right) comparison of high-pressure and low-pressure EGR. The table lists steady-state measurement data of an engine at a fixed operation point, where the oxygen concentration in the intake manifold is derived once with high-pressure EGR and once with low-pressure EGR. The plot on the right compares the dynamic behavior of the intake manifold pressure and burnt gas ratio for a step of the high-pressure EGR throttle (green) to a step of the low-pressure EGR throttle (blue). Both the table and the plot are taken from [17].

A further shared objective of Empa and ETH IDSC is to investigate the potential of EGR in a CNG engine with increased ignition energy (NRPD ignition). Therefore, the initial plan was to directly use the full engine described in Section 2.1.2 for the development and validation of the control algorithm and then to use it for these evaluation of the EGR potential. However, due to long delivery delays attributed to the pandemic and other hardware issues, the project did not progress as fast as planned, which resulted in some changes in the initial definition of the project tasks:

- Instead of the full engine, a considerably larger engine with a different air path structure was chosen as one of two engines used to develop the control algorithm. This choice additionally allowed the demonstration of the proposed algorithm for heavy-duty applications. In order to still be able to investigate the potential of EGR with the full CNG engine at Empa, a simple control structure was implemented that allows both high and low pressure EGR to be used in steady-state operation.
- As by the end of the project there was no measurement data of the full CNG engine with NRPD ignition and EGR available, the project task to evaluate the potential of EGR for a CNG engine with increased ignition energy could not be completed. Instead, the focus was set to the derivation of an automated workflow for the generation of embedded controllers with by the further development of open-source software.

2.2.3 Experimental Setup

Two laboratory engines of ETH IDSC of different size and air path configuration are used for the development and validation of a generic control algorithm. As the main development platform, an adapted light-duty 2L industrial diesel engine is used. The engine air-path is equal to the one of the full CNG engine at Empa and contains a variable-geometry turbocharger and two EGR paths. The second development platform is a 7L heavy-duty diesel engine that has a turbocharger with a waste-gate, a

high-pressure EGR path, and an exhaust brake. Figure 10 lists the main characteristics and shows an air path scheme of the two engines.

Property	Value
Number of cylinders	4
Displacement	1968 cm^3
Bore	81 mm
Stroke	95.5 mm
Speed Range	830-3400 rpm
Max. Power	75 kW at 3000 rpm
Max. Torque	285 Nm at 1750 rpm

Property	Value
Number of cylinders	4
Displacement	7 L
Bore	122 mm
Stroke	150 mm
Speed Range	650-2200 rpm
Nominal Power	200 kW at 1900 rpm
Nominal Torque max.	1260 Nm

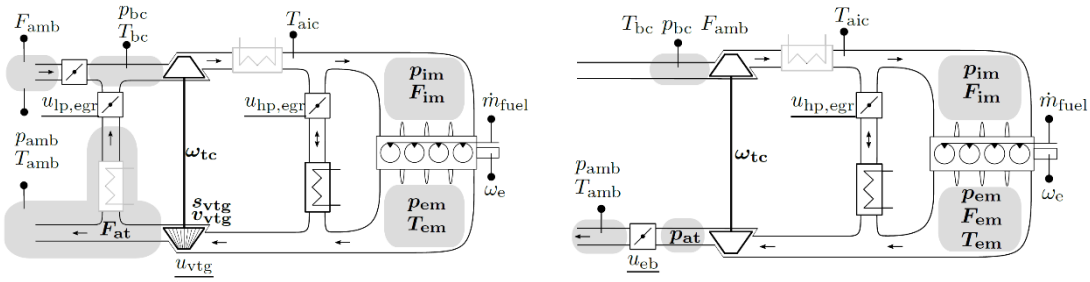

Figure 10 Characteristics (top) and air path schemes (bottom) of the two engines used for the development and validation of the control algorithm. The left engine is further referred to as light-duty engine or engine A. The right engine is further referred to as heavy-duty engine or engine B. Control inputs are underlined, states are bold, and signals modeled as known disturbances are marked with pins. Graphics are taken from [17].

Both engines are equipped with a rapid control prototyping (RCP) system, which acts as a freely programmable engine control platform. It contains all the sensor information and is connected to all the actuators of the engine. It includes an own control software, and handles all the tasks necessary to safely operate and control the engine. Due to the computational demand of optimization based control strategies, a second RCP is acquired specifically for the air-path control tasks. The complete engine control setup is depicted in Figure 11.

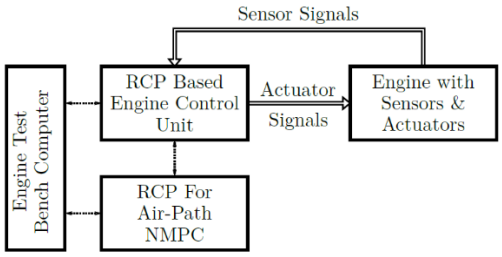

Figure 11: General engine control structure with extended computation power for the air-path control implementation. Graphic is taken from [18].

Both laboratory engines can be equipped with various measurement systems that allow to measure engine efficiency as well as engine emissions.

2.2.4 Approach

One of the few algorithms that is able to cope with the described system characteristics and control requirements is nonlinear model predictive control (NMPC). As illustrated in Figure 12, this method uses a nonlinear model of the system together with an optimization algorithm in order to predict the

best possible system actuation over a fixed time horizon. In order to account for model errors and disturbances in real-time, the algorithm is implemented on an embedded processor and re-evaluated with a fixed sample time under consideration of the newest system sensor data.

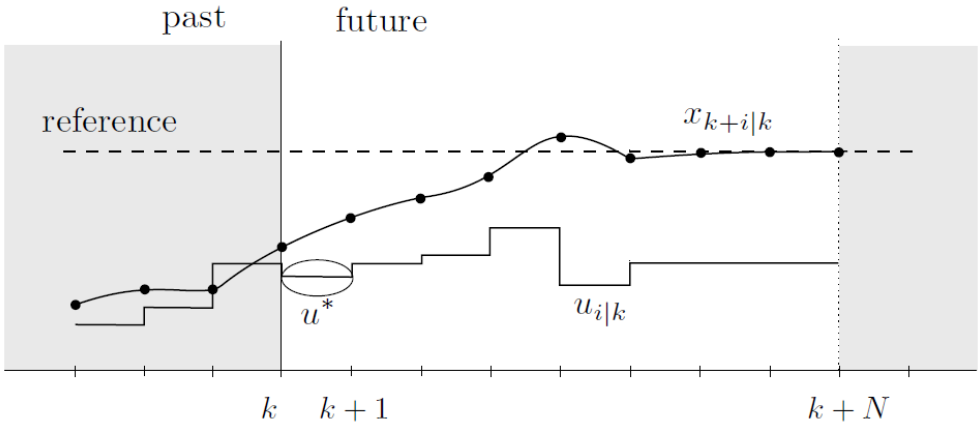

Figure 12: Function principle of a model predictive controller.

With the aim to develop a toolchain for the derivation of highly dynamic and precise control algorithms for arbitrary and possibly overactuated air path systems, the following specific design choices are made:

- Instead of a data-based model of the complete air path, a model library of individual air path components is developed. These models are based on first principles and specifically designed functions in order to capture the component behavior with a low number if identification parameters (grey-box models). With the combination of these component models, complete air path models for various air path configurations can be derived. This modular approach ensures that the model contains a large number of physical signals of the system, which can all be used for the formulation of the control algorithm (cost function and/or constraints of optimization problems). Further, it considerably simplifies the transfer of an existing algorithm to another engine, due to the fact that all model components exist already and just have to be connected and re-identified according to the new engine setup.
- A complete air path model is identified by identifying each component separately, which keeps the number of identification parameters per identification process low. This strategy together with the fact that the number of identification parameters in the component models is kept low, prevents overfitting and allows to identify complex engine air paths with a low amount of measurement data.
- In order to properly handle overactuated systems, a two-layer NMPC approach as described in [19] and depicted in Figure 13 is chosen. It consists of a target selector (TS) that calculates the optimal steady state depending on multiple objectives, which is then used as a reference for the nonlinear model predictive control algorithm. As an example, for a dual-loop EGR air path the target selector first calculates the split between high-pressure and low-pressure EGR, and then uses it as a reference, which is tracked by the NMPC algorithm.
- In order for the target selector to derive optimal reference values, the underlying model has to be highly accurate. For this reason, the model library developed within the REAL project consists of more complex approaches, but also has a lower model error compared to the models published in recent publications.

- In most engine air path setups, the intake manifold gas temperature can only be controlled with the intercooler after the compressor, which is very slow compared to other actuators. Therefore, the control of the temperature with the intercooler is not integrated within the developed control structure depicted in Figure 13, but controlled separately with a simple control approach. The NMPC algorithm considers the temperature of the gas exiting the intercooler as a known disturbance.

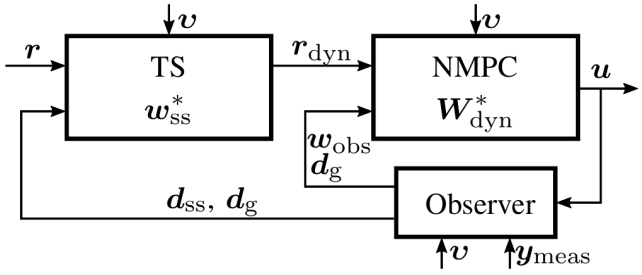

Figure 13: Schematic of the developed control structure, consisting of an observer that corrects the model, a nonlinear steady-state optimization (TS) which derives the optimal steady state, and the calculation of the optimal actuation trajectories in order to drive the system to the optimal steady state (NMPC). The graphic is taken from [17].

The development of the complete algorithm including its evaluation on two engines is completed in two steps:

1. In a first step, controllers for simple air path configurations, which are not overactuated, were developed. For the air path of the light-duty engine, only high-pressure EGR is used. The target selector is omitted for both engines.
2. In a second step, the algorithm is extended with the ability to derive reference values for overactuated systems, such as the dual-loop EGR air path setup of the light-duty engine.

For both steps, the following procedure was applied for the development of the controllers:

a. Derivation of optimization oriented grey-box models for each individual air path component.
b. Identification of the air path components for two different engines.
c. Derivation of a control structure suited for air path control (final result depicted in Figure 13).
d. Derivation of controllers for both engines based on the derived models and the control structure. Tuning of the controllers in simulation.
    - ➢ If simulation results are unsatisfying, repeat procedure (go to step a)
e. Implementation of a workflow, which allows to auto-generate C code for the implemented control structure and deploy it to the RCP platform.
f. Experimental validation of the control performance for the derived controllers on two engines.
    - ➢ If experimental results are unsatisfying, repeat procedure (go to step a)

The completion of the second step based on this procedure implies the successful completion of the scientific tasks of ETH IDSC within the REAL project.

2.3 WP3: Optical and Numerical Methods

One part of the work performed by LAV ETH focused on the experimental study of the injection process, spray development, mixture formation and ignition of a methane jet under steady and transient conditions. Different experimental campaigns were carried out in a constant volume chamber and in an optical engine while applying diverse visualization techniques. Methane was injected at up to 500 bar into air while changing the chamber pressure to obtain pressure ratios ranging from 5 to 25. The influence of different parameters on the spray processes is presented in this chapter. The second part was the development of a numerical simulation framework for high-pressure gas injection.

Optical Setup

In this section, the experimental approach will be described. The test benches used will be presented, along with the possible conditions that can be achieved, and subdivision of the test runs based on these possibilities will be defined. Then the prototype gas injector used for the experiments and the relevant high-pressure gas circuit will be described in detail.

The injections were investigated based on the pressure/volume conditions and whether or not an ignition reaction was expected. As such, two different test rigs were used. First, a constant volume cell (CVC, high-pressure temperature cell) with several possible optical accesses and multiple modes of operation. Second, an optical engine with a modified cylinder head, through which optical access is possible, offering variable (increasing and decreasing) pressures, similar to a real engine. These options result in the following matrix of experiments dividing the injection cases between inert and reactive conditions as well as between constant and variable pressure/volume shown in Table 1.

Table 1: Main division of the experiments based on the required in-cylinder conditions.

	Steady environment	**Transient environment**
Inert conditions	Cell	Engine
Reactive conditions	Cell	*Future work* (Engine)

2.3.1 Constant Volume Cell

The experiments under a steady environment were performed in the high-pressure high-temperature combustion chamber, which is a constant volume cell (CVC). The CVC was designed as a test-rig in which spray combustion could be studied [20]–[23]. It has a combustion chamber with a diameter of 110mm and a depth of 60mm. The CVC is equipped with a large frontal optical access of 85mm of diameter, and four smaller lateral optical accesses, each of 42mm of diameter; these give excellent access for the application of various optical diagnostic techniques of single- and multi-orifice sprays and jets. It has four electrical heaters inside the body and two more attached to the back, and two valves, one for the inlet of fresh air and another for the outlet of exhaust gases. The cell can be operated in two modes:

- **Electrical heating:** In this mode, the body can be heated up to 650K and is usually filled with air up to 80 bar. This mode is ideal for cases with low temperature or low pressure, also for non-reactive injection events in which an inert environment of nitrogen or other gas mixtures is required.
- **Pre-combustion:** In this mode, the cell body is heated up to 500K and filled up to 30 bar, then an additional charge of fuel and oxidant are injected into the chamber and ignited by a spark

plug. This combustion causes the chamber pressure and temperature to rise to over 100 bar and 1000 K, respectively. Then, a trigger signal is sent and the desired conditions.

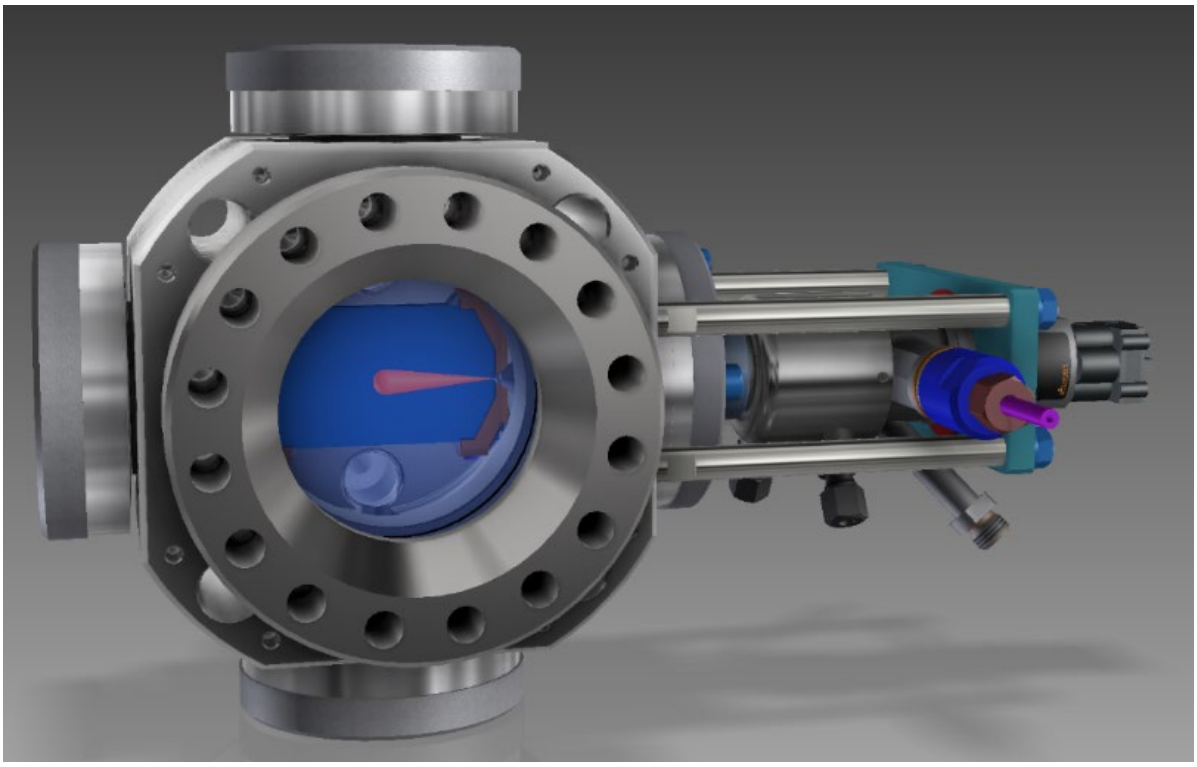

Figure 14: Constant Volume Cell with the injector mounted on the side.

The measurement conditions (pressure, temperature) are very well controlled and reproducible on both operational modes. The high pressure chamber is ideal for studies of diffusion flames, including spray propagation (liquid and vapor). Compared to similar facilities [24], it is possible to obtain nearly quiescent and steady thermodynamic conditions in the test chamber [20], [25], [26]. Figure 14 shows the CVC with the injector mounted on the side, in order to take advantage of the main window for visualization. It can also be seen that a mirror is mounted inside the chamber to allow the application of the schlieren technique.

2.3.2 Optical engine

The experiments under transient conditions have been performed in the Flex-OeCoS optical engine. The Flex is an electrically driven modified engine crankcase based on a Liebherr D944 engine with 4 cylinders, a cylinder diameter of 130 mm and a stroke of 150 mm equaling a per cylinder volume of 2 liters. Cylinders 1,2 and 4 are deactivated while the working cylinder 3 possesses the instrumented variable volume chamber, capable of safe operation at a maximum of 150 bar chamber pressure. Its modified cylinder head has 2 60 mm diameter windows in line, which allow for optical access into the volume. The injector is mounted on top of the cylinder head and fires downwards into the field of view. The flexible engine has a working speed of 600 rpm. Injection was triggered by the pressure inside the chamber during the compression stage, as the cylinder approached top dead center. This results in a

rising pressure during a given injection event and a decreasing pressure ratio, if the injector pressure is kept constant.

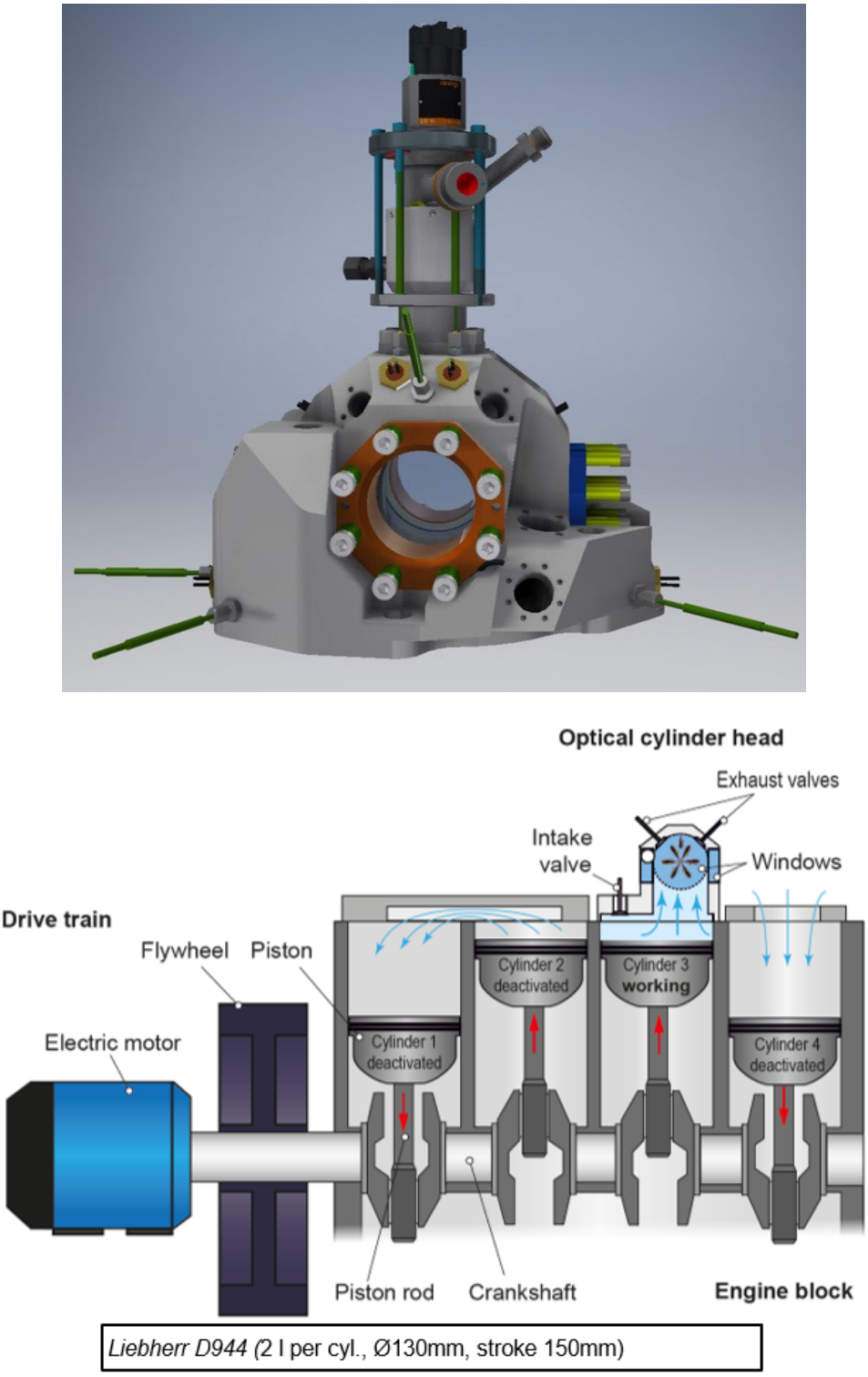

Figure 15: Optical engine test rig. Model of the optical cylinder head with the injector mounted above (*Top*). Overview of the motored engine crankcase (*Bottom*).

2.3.3 High-pressure gas injector

The injector used for the experiments is a prototype derived from a series heavy-duty diesel injector designed and built for research purposes by Woodward L'Orange GmbH. Figure 16 shows the different sections of the injector. Represented in blue is the compartment used for the injection fluid, which was methane during this experimental campaign; in red the control fluid, which was diesel for these experiments, is represented. The function of the control fluid is to keep the needle closed while keeping pressure in the sac; this is achieved through the piston rod as this keeps both compartments isolated from each other. The injector is designed to work up to 500 bar of gas pressure on the injection side, while the pressure of the control fluid should be 50 bar above the injection pressure during normal operation. The injector has a single-hole axial orifice with an exit diameter of 0.7mm. This prototype injector is instrumented in order to monitor the injection pressure and temperatures, as well as the needle and magnet pin movement. The pressure and temperature are recorded using a Type 4065B piezoresistive sensor by Kistler Instruments AG, while the needle movements is measured on the piston rod depicted in red in Figure 16. To accomplish that, a sensor manufactured by Micro-Epsilon GmbH accurately measures the distance to a surface. The anchor movements is measured inductively with a pin attached to the anchor and moves inside the coil.

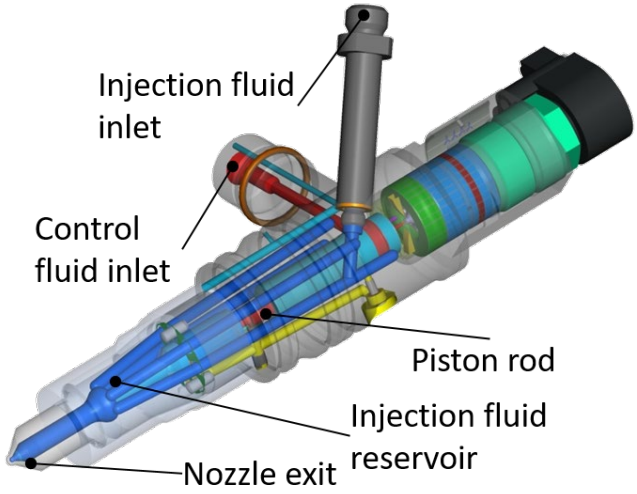

Figure 16: Prototype gas injector.

In order to quantify the spray behavior and development inside the chamber, different optical techniques were applied. The digital images have been analyzed by means of purpose-developed processing software, which delivers the spray/flame geometrical parameters. Examples of schlieren, Mie-scattering and OH* chemiluminescence images are shown in Figure 19, Figure 20, Figure 22, Figure 23 and Figure 24.

2.3.4 Optical pre-chamber

The original plan in this project was to use a Rapid-Compression-Expansion Machine (RCEM) for experiments with optical diagnostics of ignition and flame propagation. Due to unforeseen problems

with the RCEM, the project team decided to use another test rig instead: the optical pre-chamber (OPC) which has been designed and built to allow the study of turbulent jet ignition under different operating conditions. The test-rig contains two volumes, which are connected through a single interchangeable nozzle. The smaller of the two volumes (pre-chamber) contains an ignition source (sparkplug), which allows the ignition of the mixture. The orifice connecting the pre-chamber to the main chamber can be changed in shape and diameter, and can fit a nozzle with a maximum diameter of 4 mm. In the configuration used in this investigation, the volume of the main chamber is 187 cm^3, whereas the pre-chamber is 36 cm^3 (~16% of the total volume).

Both chambers have windows to allow optical access into the respective volumes, which enable optical measurements during the combustion event as shown in Figure 17. The pre-chamber is fitted with two opposing windows, which allow optical access through the complete pre-chamber volume. The main chamber also has two opposing windows, allowing optical access from the nozzle exit to the bottom of the chamber. A removable opposing wall is placed 40 mm away from the nozzle exit.

The operation and control sequences of the OPC allow the accurate setting of conditions in both chambers prior to ignition (pressure, temperature, air to fuel ratio, dwell time). The charge air pressure and temperature are feedback controlled through a pressure regulator and an electrical heating system. The fuel in the main chamber is injected using a hollow-cone piezo injector, and the mixture composition is determined using the pressure signal and a partial pressure calculation. Then a purge valve is opened to allow the pre-chamber air out while allowing the air-fuel mixture from the main chamber to flow through the nozzle into the pre-chamber. A graphical sequence of the processes is shown in Figure 18. The fuel used in this study is pure methane (N45, ≥ 99,995 mol %). This filling process create a dynamic air movement inside the pre-chamber that could be classified as turbulent. Therefore, the dwell time controls how much turbulence is dissipated before sparking, and is used as an indicator of laminar or turbulent conditions in the chamber.

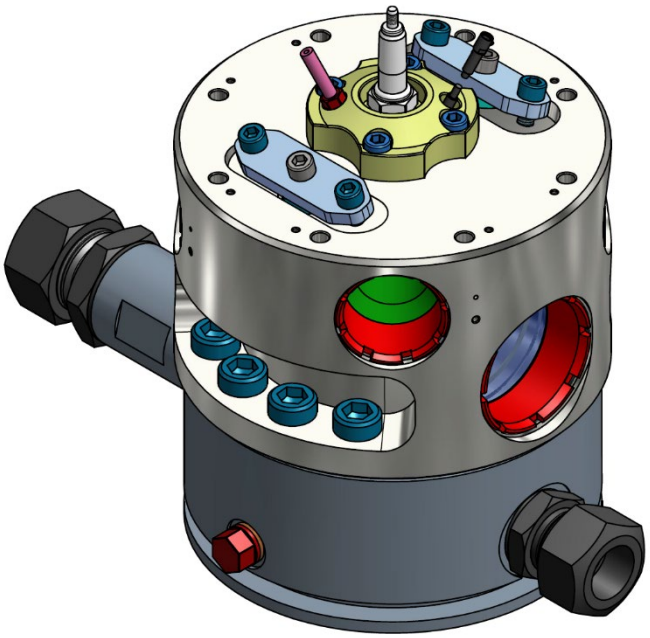

Figure 17: Overview of the Optical Pre-Chamber (OPC) setup.

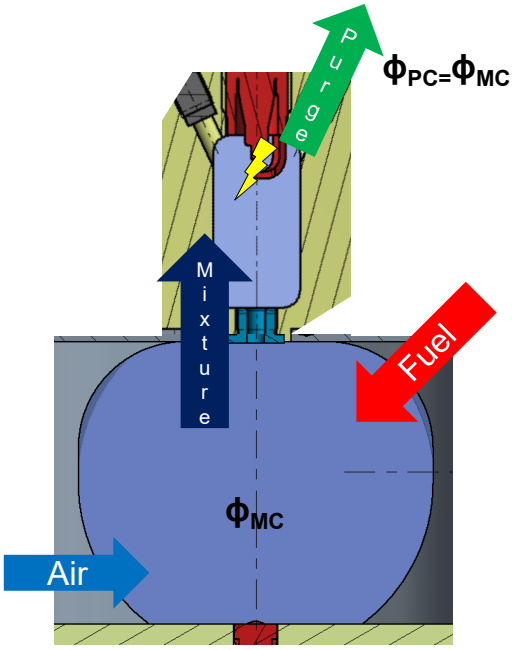

Figure 18: Sequence of the filling process (right). (1) The main chamber is filled with air, (2) the fuel is injected into the main chamber, (3) a purge valve is opened, (4) the air-fuel mixture flows into the pre-chamber, (5) the spark is sent after the dwell time.

2.3.5 Schlieren visualization technique

The spray evolution inside the combustion chamber and the OPC has been recorded by schlieren imaging [27]. This technique is sensitive to the first spatial derivative of density within the combustion chamber, which makes it useful to detect spray boundaries and thus evaluate macroscopic spray scales. This technique shows the boundary between vaporized liquid and background gas because of the refractive index differences that exist between them. Additionally, density gradients are also created in the chamber as the vaporized liquid cools the ambient gas [28]; such refractive index gradients are also present during combustion, as the high temperature creates low density regions. Therefore, this method is valid for inert and reactive conditions. For this technique, the spray has to be illuminated from one side by a collimated light beam. The shadow produced by the spray is then gathered with a lens and at its focal length, a diaphragm is positioned to produce the schlieren effect by eliminating the diverted light beams. A high-speed camera then captures the image produced in order to obtain a time resolved evolution of the spray.

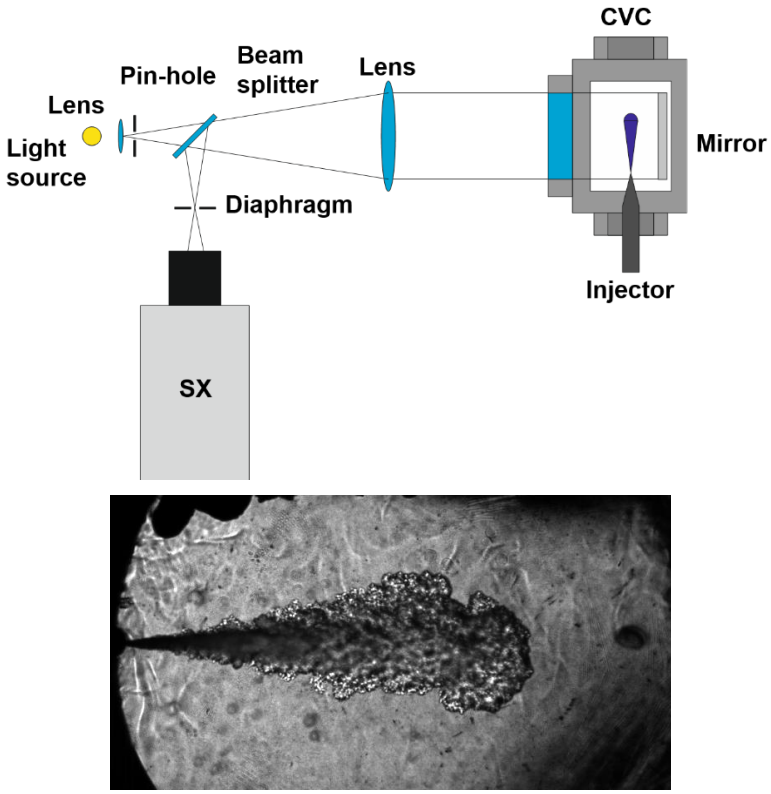

Figure 19: Double-pass schlieren setup on the Constant Volume Cell.

A schematic of the optical arrangement for the double-pass schlieren technique is shown in Figure 19. The jet is illuminated from the front side of the cell, while the shadow is reflected on the mirror and recorded from the same optical access by means of a camera. The mirror used is a fused silica high-reflection single coating, built for high temperature and designed for the visible light in the wavelength range of 420-750 nm. Illumination is achieved by means of a continuous Xenon lamp; in order to reduce the size of the light source and improve sensitivity, a pin-hole is placed just at the bundle exit, in order to form a light source with a diameter of 1 mm. The pinhole was placed at the focal length of a Plano-convex lens to generate collimated light beams. This lens also works to focus the collimated light of the reflected image onto the camera lens and then be recorded by the camera sensor. A diaphragm is placed at the focal point of the beam to filter the light beams that have been diverted from their original parallel direction due to density gradients. The camera used for the experiments was 12bit Photron SX CMOS high-speed camera equipped with a Sigma 50mm f/1.4 lens were used; image acquisition frequency was 40000FPS with a exposure time of 5 µs and 10 of pixel/mm ratio.

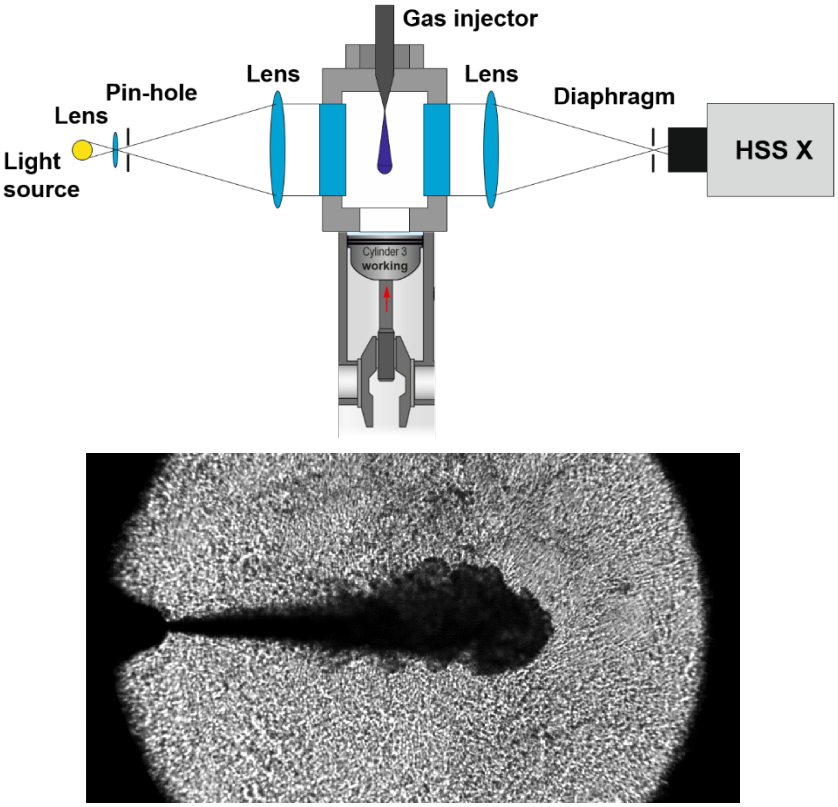

Figure 20: Single-pass schlieren setup on the optical engine.

Figure 20 shows the schematic layout of the single-pass schlieren setup that was used on the optical engine. Light from a continuous Xenon lamp is focused onto a pinhole to create a close to point-like light source at the focal point of a primary plano-convex lens. Consequently, a collimated light beam is created that enters the modified cylinder head through the first optical access and into the test area. It then exits through the second optical access and is focused onto a cut-off diaphragm by a secondary plano-convex lens identical to its counterpart on the other side of the test area. Ideally, the cut-off diaphragm is closed so that its size is equal to that of the pinhole at the light source assuming no deviations of the light beam are present. The sensitivity of the setup can be decreased or increased by opening or closing the cut-off diaphragm, cutting off light beams that have deviated because of a change in refractive index in the test region. The schlieren image hits the sensor of a HSS-X high-speed camera, having its position after the cutoff and its lens adjusted so that the region of interest covers the sensor array. As the engine runs at 600RPM at a temporal resolution of 0.1° crank angle (CA) a frame rate of 36000FPS is reached. With this setup a pixel resolution of 13 px/mm was reached at a field of view of about 45 mm. Due to the turbulent gas movement in the compressed volume a non-uniform background was expected.

In order to visualize the ignition and flame propagation in the pre-chamber as well as the turbulent jet coming into the main chamber and subsequent combustion of the mixture, multiple schlieren arrangements were setup as shown in

Figure 21. To accomplish this, two Xenon light sources were used in conjuntion with a diaphram (0.5mm) in order to generate a focal light source. Two pairs of plano-convex lenses (f=250mm) were applied to generate a collimated beam before entering the combustion chambers and to converge the

collimated beam at the exit. Then a diaphragm placed at the focal point to eliminate the diverging beams and increase the sensitivity to density gradients. The images have been then recorded by two high-speed cameras from LaVision. On the pre-chamber a HSS6 was used with an exposure time of 2us and a resolution of 128x256px; while on the main-chamber a HSSX was used with an exposure time of 1us and a resolution of 640x512px. Both camera are synchronized and recording at 10kFPS.

An additional parallel setup was run to observe the phenomena taking place near the electrodes of the sparkplug. For this a third schlieren setup was implemented in the pre-chamber with a resolution of 128x128px and a frame rate of 100kFPS using a HSS high-speed camera. This setup uses the light source from the pre-chamber schlieren setup and with a second identical plano-convex lens (f=250mm) and a diaphragm. The optical pre-chamber is equipped with the fiber-optic spark plug (FOSP) developed for NRPD ignition and described in Section 2.1.1.

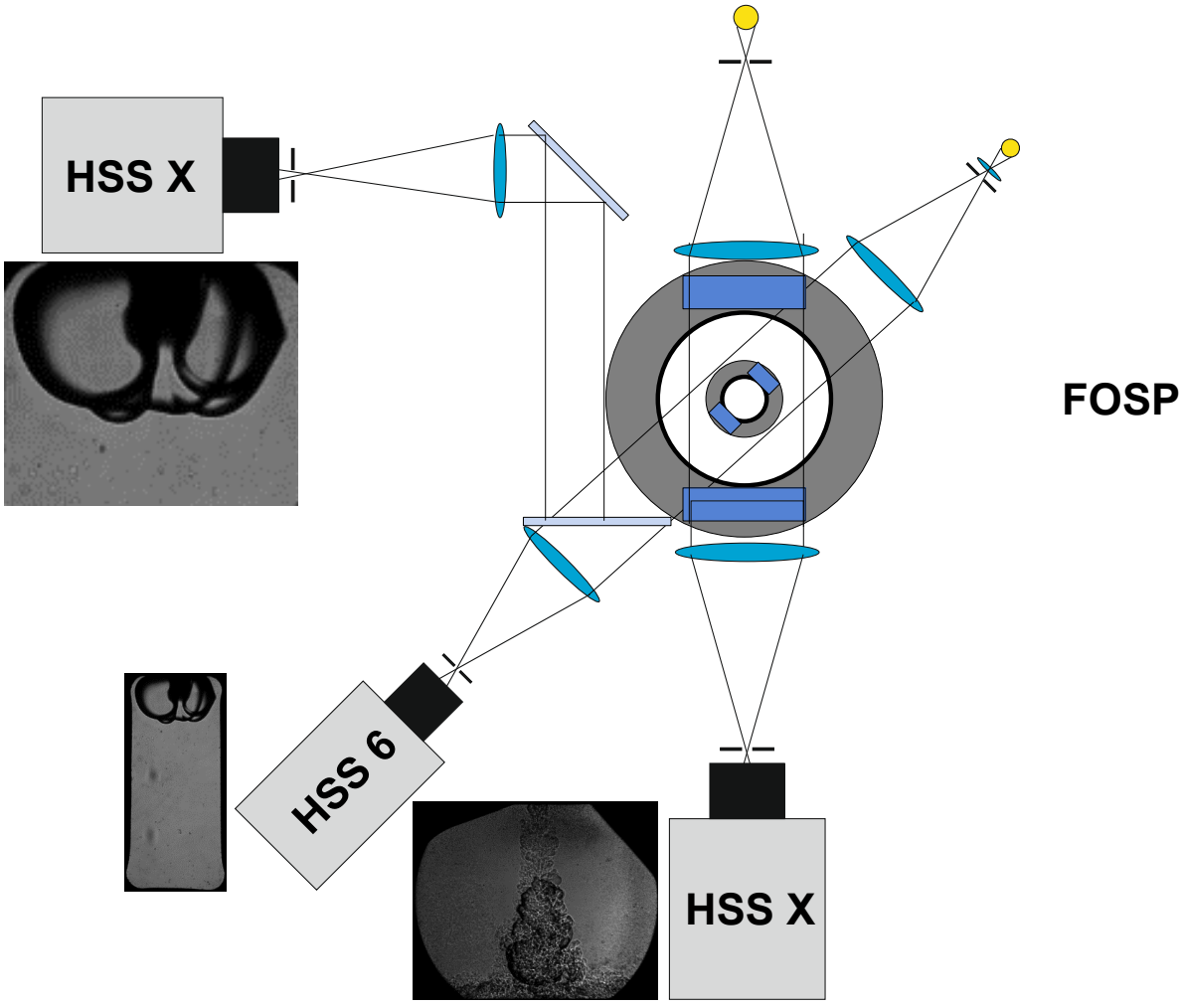

Figure 21: Simultaneous schlieren setup for pre-chamber, main chamber and close up visualization in the optical pre-chamber. The system is equipped with a FOSP (fiber-optic spark plug) for ignition with NRPD systems.

2.3.6 Mie-scattering visualization technique

The penetration of the liquid core of the spray has been captured by Mie-scattering imaging, which relies on the light reflected by liquid droplets. In practice, two types of light scattering are happening. On the one hand, the spherical particles larger than one tenth of the incident wavelength are scattering the light under the hypothesis of kinetic energy conservation, also known as "elastic scattering", and most of it is reflected in the same direction of the incident wavelength; this is Mie-scattering. On the other hand, the particles that are much smaller than the wavelength, even on a molecular scale, are diffusing the light in a more homogeneous way: this is Rayleigh-scattering. Therefore, an evaporating spray presents both types of scattering; nevertheless, the intensity of the light reflected by the vapor phase is so low compared to that of the liquid that their effect is negligible, making this technique appropriate to measure liquid length.

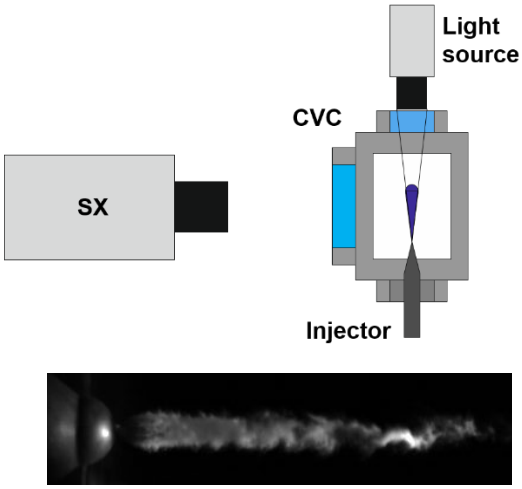

Figure 22: High-speed mie-scattering setup on the CVC.

A schematic of the optical arrangement for the Mie-scattering technique is shown in Figure 22. The spray has been illuminated from the front of the combustion chamber, and the image has been recorded from the right side via a CMOS camera. The light source was a Xenon lamp and was fitted with a lens to focus the beam on the injector tip. On the collecting side, the camera was placed in front of the main window but was tilted downward so it could be above the schlieren optics but still be perpendicular to the spray axis. A 12bit Photron SX CMOS high-speed camera equipped with a Nikkor 100mm f/2.8 lens was used; with an image acquisition frequency of 20000FPS with an exposure time of 3.75µs and 10 of pixel/mm ratio.

2.3.7 Tracer LIF visualization technique

The mass fraction distribution has been quantified by the tracer Laser-induced fluorescence (LIF) method. LIF is an optical technique in which a molecule is excited to a higher energy level by the absorption of laser light, followed by spontaneous emission of light. If a particular substance does not fluoresce, then it needs to be seeded with a fluorescing tracer. In

Figure 23 the optical setup of the applied tracer LIF diagnostics is summarized. The acetone fluorescence is excited at 266~nm by means of a frequency-quadrupled Nd:YAG pulse laser (Quantel Q-smart 850) operated at 10Hz repetition rate with a nominal output energy of 100mJ per pulse. The laser beam is expanded into a collimated light sheet of 40mm height by a combination of cylindrical lenses (f=-50mm, f=250mm). Saturation of the LIF signal is avoided by adding a third cylindrical lens (f=1500mm), so that the waist of the expanded beam is placed outside the CVC. The resulting sheet thickness is estimated below 1mm throughout the visible domain. To monitor shot-to-shot pulse energy fluctuations as well as spatial variations of the laser sheet profile, part of the laser light is deflected by a silica plate and directed onto a fluorescent screen. The laser light sheet then enters the CVC from the left and is directed onto the injector tip. 1-D sheet profile as well as acetone fluorescence are recorded by CCD cameras of the same type (PCO PixelFly). Both cameras are equipped with Schneider-Kreuznach 25mm f/.95 lenses and are operated at 1ms exposure time with 2x2 pixel binning. To block laser stray light in the wavelength range of the excitation, a longpass filter (Schott BG25) is placed in front of the tracer LIF camera. After processing the data, the pixel resolution of the resulting concentration fields corresponds to 4.3 pixel/mm in object space. All tracer LIF images are obtained 2.5ms after start of injection.

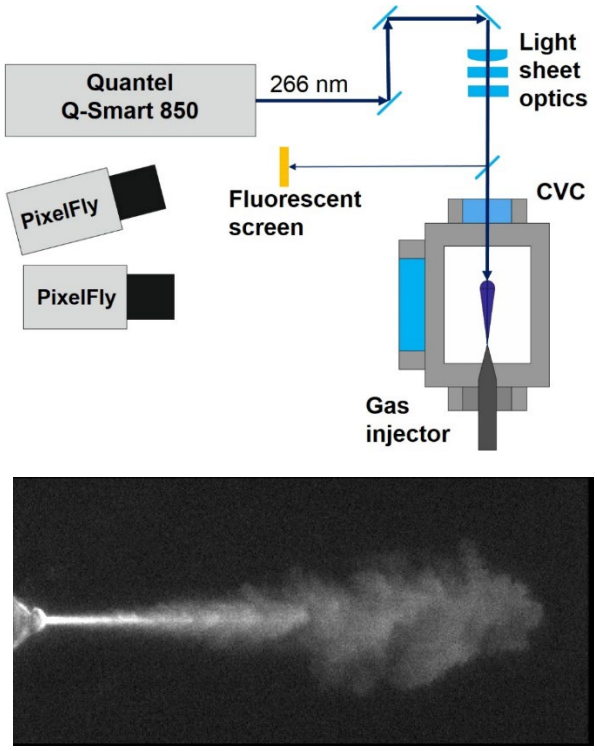

Figure 23: Tracer LIF setup on the CVC.

2.3.8 OH* visualization technique

The lift-off length (*LoL*) and ignition delay (*ID*) were recorded by high-speed OH* chemiluminescence imaging. This technique records radiation at 310nm, which is controlled by the OH* radical, being a marker of the start of ignition and the diffusion flame limits, and thus of the lift-off length for diesel

sprays [29]. Additionally, the wavelength band of 310nm that corresponds to the chemiluminescence of the OH* radical is the strongest one and therefore best for determining the lift-off length [29]. Although soot radiation could also be contributing to the recorded signal in the images, previous studies in the literature [29] also indicate that there should exist a spatial separation in both contributions. Therefore, while the downstream radiation will most probably be dominated by soot, the most upstream one is assumed to be essentially related to OH* chemiluminescence.

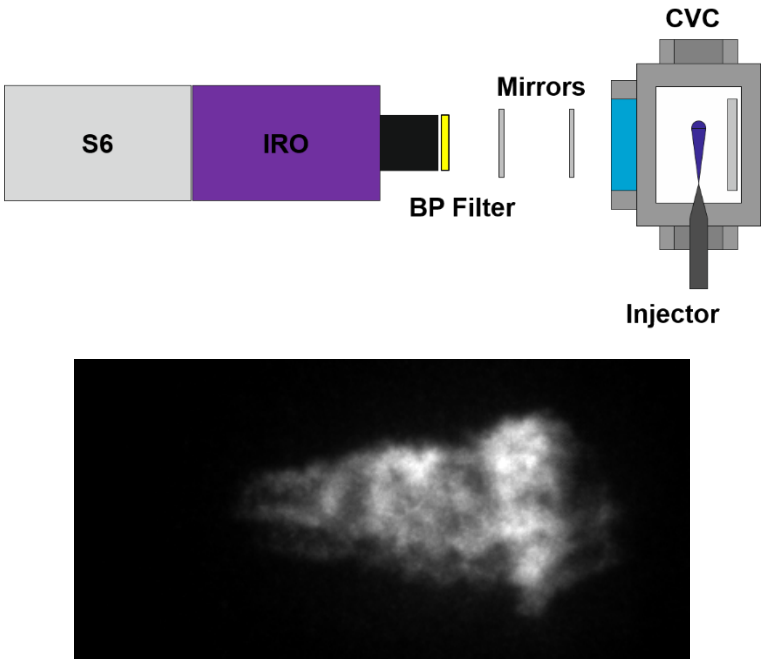

Figure 24: OH* chemiluminescence setup on the Constant Volume Cell.

A schematic of the optical arrangement for the OH* chemiluminescence technique is shown in Figure 24. Two flat UV mirrors are placed in order to redirect the light from the combustion to the camera that is placed below the schlieren optics. Due to the low intensity emitted by the UV radiation from the OH* radical, an image intensifier has been coupled and synchronized to the camera. In order to avoid capturing any other type of radiation, a band pass filter with a center wavelength of 310nm was placed in front of the lens. A 12bit Photron S6 CMOS high-speed camera equipped coupled to a LaVision IRO high-speed image intensifier with a Sodern UV 100mm f/2.8 lens was used; with an image acquisition frequency from 40'000 FPS with an exposure time of 20ms and 6 of pixel/mm ratio.

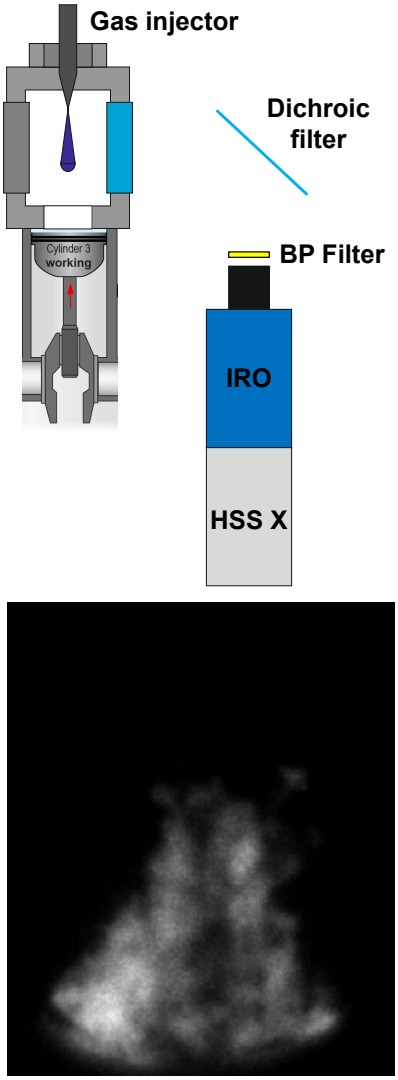

Figure 25: OH* chemiluminescence setup on the optical engine.

Figure 25 shows the schematic layout of the OH* chemiluminescence setup that was used on the optical engine. A dichroic mirror was used to let reflect the UV radiation (below 400nm) and to let through the visible light (above 400nm). The reflected light is then reduced to a specific bandwidth with a band pass filter (310nm) to visualize only the radiation corresponding to OH* radical. The light is focused by UV Hallce Nachfolger 100mm f/2 objective and then multiplied by the IRO image intensifier to be captured by a Photron HSS6 high-speed camera. As the engine runs at 600RPM at a temporal resolution of 0.1° crank angle (CA) a frame rate of 36000FPS is reached. With this setup, a pixel resolution of 9.45 px/mm was reached at a field of view of about 60mm.

2.3.9 Numerical Framework

Due to the complexity and high-resolution demands associated with describing the complex shock structures of under-expanded jets emerging in the near-nozzle area, carrying out numerical investigations at reactive condition is treated as a two-stage process, as shown in Figure 26. In the first stage, a cold flow simulation is carried out with deactivated chemistry. In this stage, the

computational domain consists of the CVC as well as the injector, which in turn contains the nozzle, the stud hole, the needle seat and the inlet, where stagnation conditions are applied. The needle lift is captured through cell stretching in the affected part of the computational mesh, in accordance with the experimentally measured needle lift. Real-gas thermodynamics are employed in the entirety of the domain.

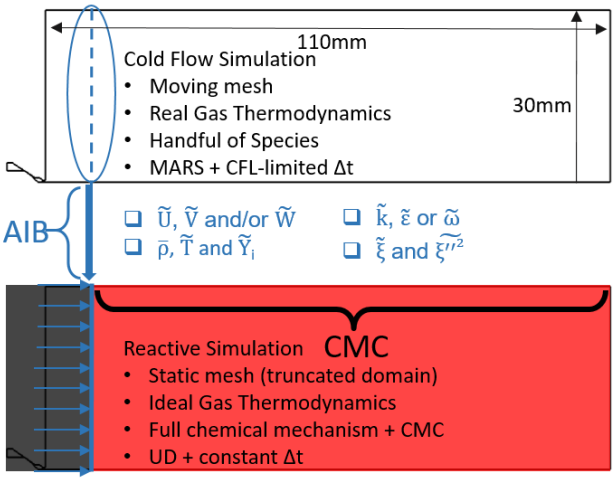

Figure 26: Schematic of the two-stage workflow for carrying out reactive, under-expanded jet investigations.

To this end, the commercial CFD software Star-CD has been interfaced with Chemkin Real Gas, as shown in Figure 27, which enables of non-ideal Equations of State and accompanying pressure corrections in the thermodynamic and caloric properties. Furthermore, Chung's semi-empirical model for transport properties of dense, multi-component fluids has been implemented into the code. The only species accounted for are those comprising the fuel stream and the ambient in the CVC. To render the computational requirements of the simulations more tractable, the RANS framework is opted for and in particular, k-omega SST is chosen as the turbulence model. In this way, the rotational symmetry of the configuration can be exploited to model just a slice of the CVC by applying cyclic boundary conditions and thus a very high spatial and temporal resolution can be targeted, which is necessary for capturing the complex shock structures in the near-nozzle area in the presence of strong under-expansion.

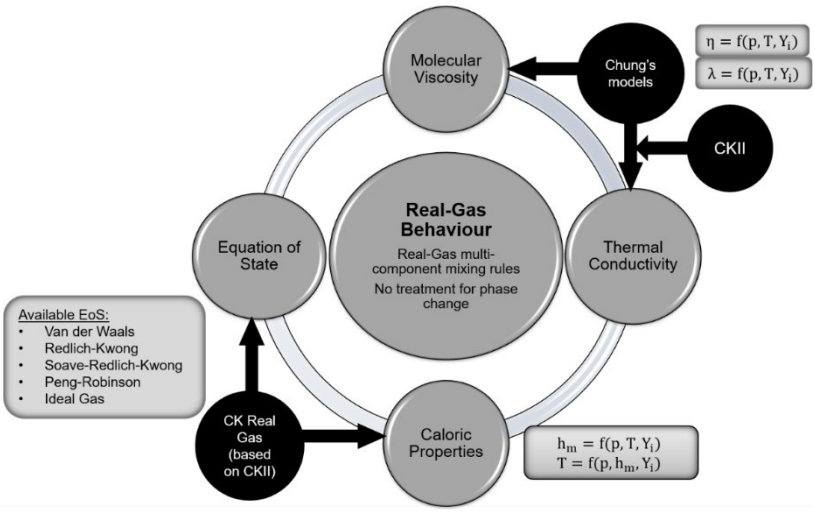

Figure 27: Extension of the CFD code Star-CD (v4.30) to account for real-gas thermodynamics.

In the second stage of the process, the actual reactive simulation is carried out. A truncated computational mesh now represents only part of the CVC. At the truncation cross-section, modified Artificial Inlet Boundary (AIB) conditions are applied, which are extracted from the time-varying flow-field solution in the respective cold flow simulation and are then carried over to the reactive simulation without any adjustments. This technique ensures that inaccuracies inherent in modelling rather than resolving jet injection, as is often the case in practice for the sake of expedience, are avoided. As regards turbulence-chemistry interaction further downstream, the Conditional Moment Closure (CMC) is chosen as the combustion model because of its suitability to non-premixed mode of combustion and highly successful past application in diesel sprays and engines simulations. The coupling to the CFD software is shown in Figure 28.

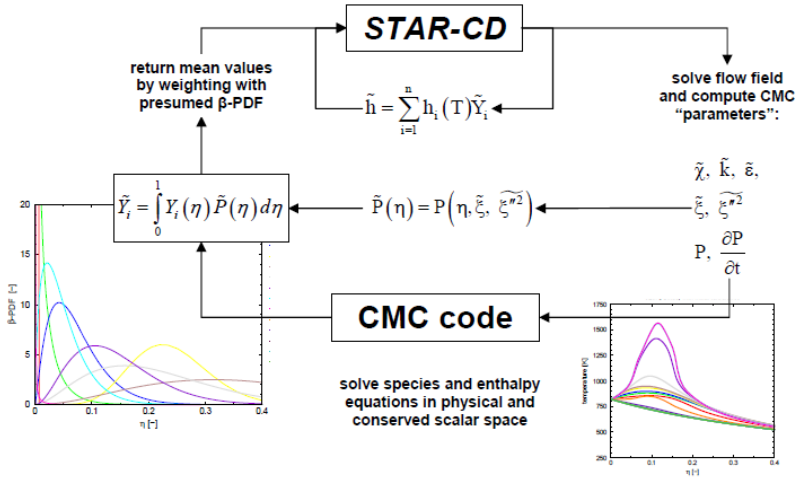

Figure 28: Schematic of the interface between the in-house combustion code CMC and the CFD software.

3 Results and discussion

3.1 WP1: Electrical Ignition Methods

3.1.1 Ignition Cell

Short duration, non-equilibrium plasmas like the ones produced in NRPD (Nanosecond Repetitively Pulsed Discharge) systems lead to efficient deposition of discharge energy in highly non-equilibrium states, including dissociation, ionization and excitation of electronic and vibrational states of molecules. Radical formation is further promoted through collision with excited species, thus leading to very favorable conditions for ignition and combustion [30] [31].

Therefore, the promising potential of NRPD ignition systems includes a decreased energy needed for successful ignition, the extension of engine operation to leaner mixtures, reduced specific fuel consumption and NOx emissions, and the possibility of several ignitions per engine cycle.

Nevertheless, for a successful application of NRPD systems, further investigation is needed for bridging the gap between the fundamental knowledge of the physical phenomena involved in such a discharge, and the practical application. Therefore, a characterization of the discharge was performed in the framework of the REAL project, in order to assess the NRPD parameters for optimizing the ignition in the present application.

After adjustment of the control unit and triggering strategy (Section 2.1.1) to adapt the spectroscopy technique to NRPD-ignition operation, preliminary tests were performed in order to ensure that the technique can be used also with NRPD to characterize the atomic spectral emissions relations to the local λ, as in previous work carried out with standard ignition systems [14]–[16], [32]. Tests were performed at different pressure values, with different pulse sequences and different maximum voltage delivered. Results show (Figure 29) that different spectral features are recognized when comparing standard ignition and NRPD ignition.

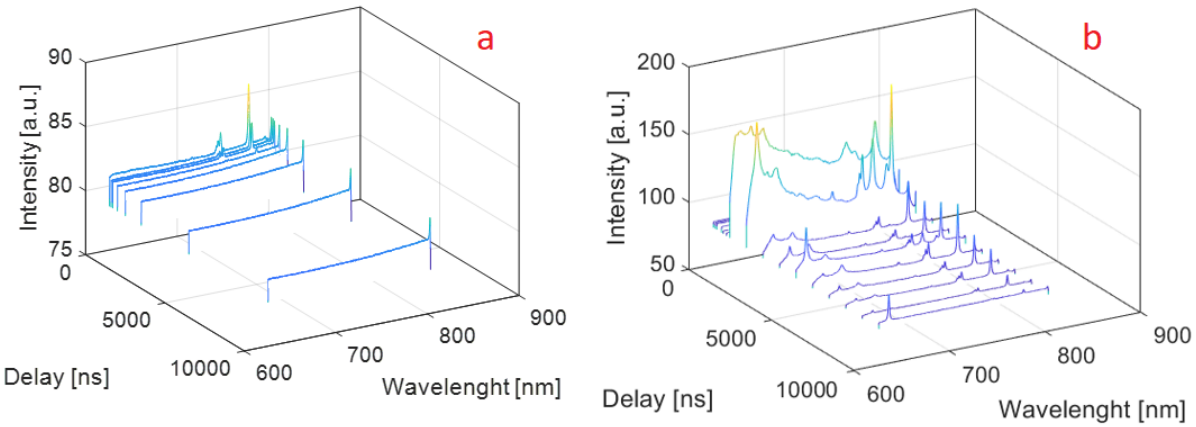

Figure 29: Atomic emission spectra for inductive ignition system (a), and NRPD ignition system (10 pulses) (b). Pressure: 10 bar. Maximum delivered voltage 15-18 kV.

Namely, the atomic emissions corresponding to hydrogen (656 nm), nitrogen (746 nm) and oxygen (777 nm) are clearly identified in all cases, but for inductive ignition (case a in Figure 29) atomic emissions are visible right after breakdown and decay within approximately 1 µs, after which molecular recombination can be identified (not shown here). When NRPD is used (b) in similar conditions of pressure, clear atomic emissions are visible for a longer time (up to 9 µs), thus suggesting plasma recombination. High continuum emissions disturb the peak identification in the early times (between 1 and 3 µs), suggesting that the discharge parameters (frequency, amplitude, pulse number and duration) should be optimized for an improved spectral diagnostics.

In order to optimize the NRPD ignition, an electrical characterization was performed taking into account the discharge dynamics of both a single pulse and a train of multiple pulses. The conditions for breakdown occurrence were investigated, and it was shown that three different types of pulses can be identified in a sequence of pulses. An example is shown in Figure 30 for a train of 10 pulses delivered at a repetition rate of 10 kHz at an operating pressure of 18 bar.

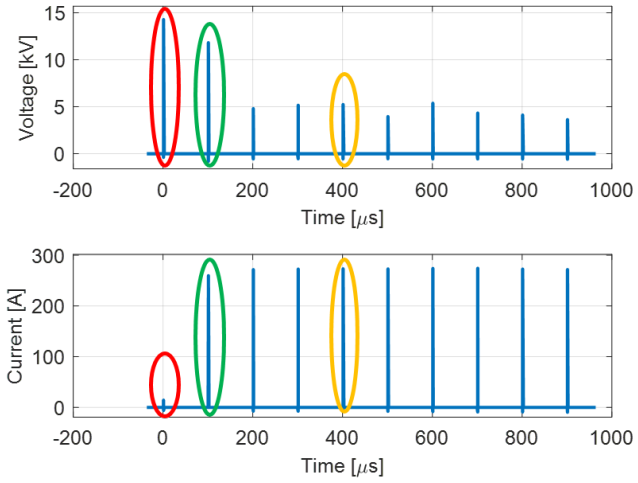

Figure 30: Voltage and current at the spark plug gap for a train of 10 pulses delivered with a repetition rate of 10 kHz at 18 bar.

In the case of the first pulse, high voltage (15 kV) and very low current are detected, and no breakdown occurs. Weak light emission is detected in the first pulse but the voltage or pulse duration is not sufficient to achieve breakdown. The second pulse shows the first occurrence of breakdown, the streamer bridges the gap, and streamer to spark transition occurs. The plasma in the transition from streamer to spark is highly ionized, the current is limited only by the active external circuit at a value of 250 A. The following pulses show a third type of behavior, with lower breakdown voltage (4-5 kV) and high current (always limited only by the electrical circuit at 250 A). The presence of active species between pulses and the local density variation due to the discharge's energy input explain the variation of breakdown voltage.

If only the first pulse is taken into account (no influence of previous pulses) and the conditions for breakdown onset are investigated, it is observed that the classical theories developed for conventional (inductive) ignition system do not apply in this case. Classical theories correlate the breakdown voltage to operating pressure, temperature and electrodes' gap. In the present work, several experiments were performed at different pressure conditions and with different gaps, and the voltage at which breakdown occurred was measured. When such voltage is compared to the theoretical breakdown voltage calculated taking into account the classical theories (Figure 31, a), it is evident that the results do not match, thus suggesting that other parameters play a role in determining breakdown

occurrence when NRPD is used. A better match is obtained when also the discharge dynamics is taken into account. Namely, beside cell conditions, it was found that also the voltage rise time plays a role in determining the breakdown voltage. If the empirical relationship correlating breakdown voltage is adapted taking into account the voltage gradient (Figure 31 b), the agreement with the experimental data improves notably, thus confirming that not only static conditions, but also the discharge dynamics affect the breakdown onset when NRPD is used.

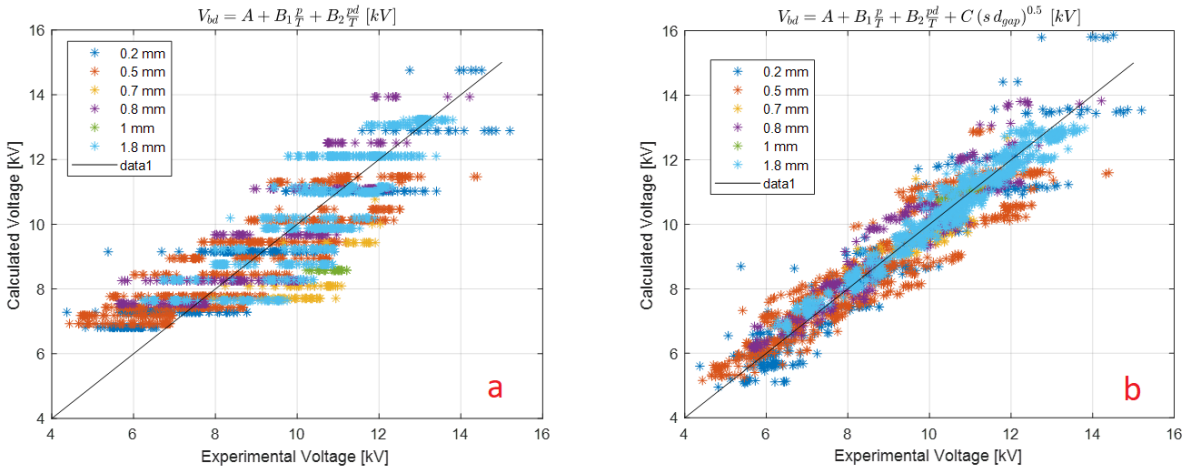

Figure 31: Calculated breakdown voltage vs. experimentally measured breakdown voltage for NRPD. Classical theories (a) are compared to present work results (b).

The results obtained from the gating strategy optimization for spectroscopy-based diagnostics and from the electrical characterization of the nanosecond pulsed discharge allowed designing a fiber-optics equipped spark plug (FOSP) optimized for NRPD ignition investigation (Section 2.1). Preliminary tests confirmed the feasibility of the new device for the present application. Figure 32 shows atomic spectral emissions obtained at two different air to fuel ratios for the lens setup (left) and the FOSP setup (right). Tests were performed using NRPD ignition, 10 pulse sequence, with a repetition rate of 10 kHz and at a pressure condition of 5 bar. The spectra were acquired right after the last pulse reached the spark plug gap, with an exposure time of 500 ns. Figure 32 shows an average over 20 spectra.

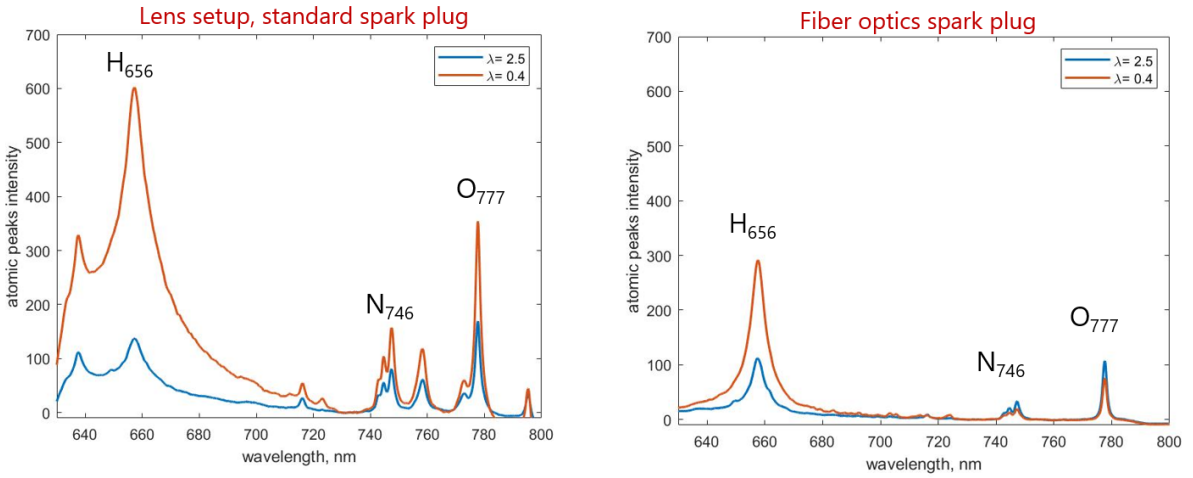

Figure 32: spectral emissions for lens setup and standard spark plug (left) compared to fiber-optics spark plug (right).

It can be seen that both setups allow identifying the atomic emissions of interest. The H-alpha line (656 nm) is a qualitative indicator of hydrogen ionization. A higher ionization level and longer recombination were detected for NRPD compared to the inductive ignition system (not shown here). The lens setup gives higher emission intensities, but displays also a high continuum emission, especially in the wavelengths around hydrogen atomic emission, resulting in lower repeatability of tests. The fiber-optics equipped spark plug, on the other hand, allows obtaining lower intensity emissions (around one half of the lens setup) but highly repeatable spectra are obtained when the light is collected by the fibers in the vicinity of the spark. As a conclusion, the FOSP feasibility for detecting the spectral emissions of interest and correlating their features with the investigated parameters (pressure, air to fuel ratio, etc.) is confirmed, and the same trends (not reported here) were obtained when using FOSP or standard lens setup. The obtained results allow this technique to be ready to transfer to an optically accessible pre-chamber setup (Section 2.3.4) for investigating the ignition and the first phases of flame kernel development using NRPD in both laminar and turbulent conditions. The results of this investigation are useful for transferring the diagnostic technique to a running engine, and are reported in Section 3.3.7. Nevertheless, for accurate control of NRPD ignition in a 4-cylinder running engine, a deeper understanding of the active electrical circuit and of the factors affecting the breakdown was needed.

Therefore, during the last year of the REAL project, an investigation was carried out in the constant volume cell to characterize the influence of pulse rise rate and pulse duration. The results were published in [33].

The electrical circuit active during the nanosecond discharge allows the doubling of the voltage sent by the pulse generator prior to breakdown and a limitation of the current after the discharge. This in turn, leads to the inception of high breakdown voltages, resulting in the formation of a highly ionized plasma and in a limitation of the heating. At the sparkplug, the pulse is partially transmitted and partially reflected depending on the ratio between the cable impedance and gas electrical impedance, as shown in Figure 33. Two discharge regimes are recognizable during this type of discharge. First, the low (displacement) current regime, where a low-conductivity medium (non-ionized gas) is present between the electrodes and the voltage across the gap is twice as high as the pulse voltage due to the pulse reflection. The second regime is the high current regime, in which only the cable impedance limits the maximal current. The voltage and the current magnitude are affected by the pulse voltage and current, by the sparkplug gap capacitance, and by the varying air-plasma electrical resistance (R).

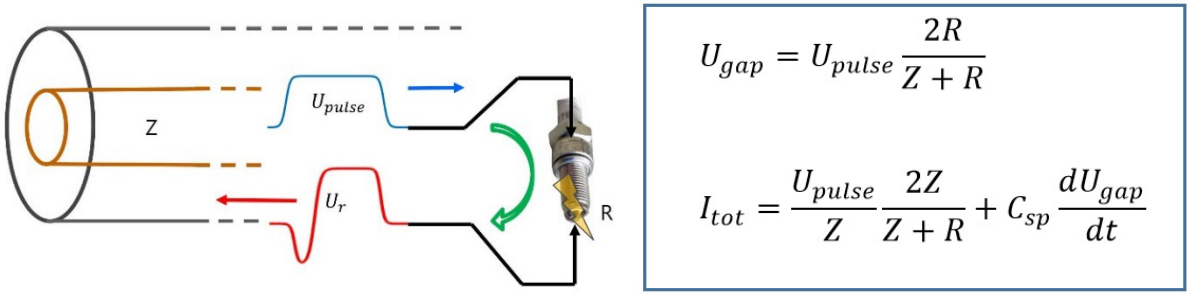

Figure 33: NRPD discharge schematics.

An example of the discharge electrical measurements is shown in Figure 34 for a 50 ns pulse at ambient temperature and a pressure of 1.5 bar with a gap distance of 0.8 mm. Subplot (a) shows the

incident (blue) and reflected pulse (red) current and equivalent voltage, whereas subplot (b) shows the plasma current (red) and the voltage (blue) across the gap. The dashed red line shows the displacement current at the sparkplug magnified ten times. Subplot (c) depicts the plasma resistance calculated as the ratio between the gap voltage and plasma current. The blue line in subplot (b) in relation to the blue line in subplot (a) outlines the voltage doubling before breakdown. As expected, the plasma resistance transitions from high values to low values. The breakdown is the point where the maximal voltage is reached, in this case at 7 ns and 6.4 kV.

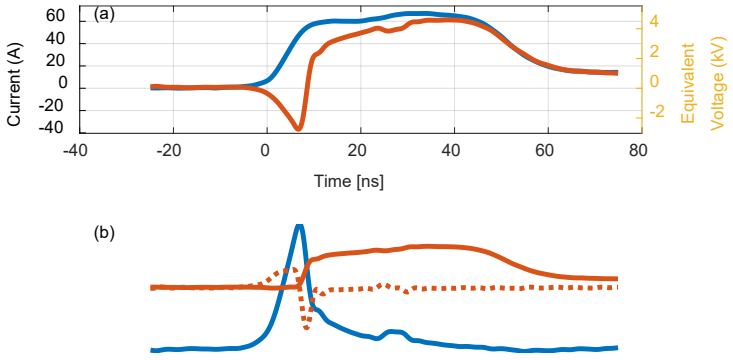

Figure 34: Example of NRPD discharge electrical measurements.

Figure 35 shows the result of the breakdown delay time analysis as a function of the maximal impulse factors (overvoltage compared to static breakdown voltage) reported in [33]. Both the formative and the statistical time decrease for higher maximum impulse factors. For high impulse factors, the delay time levels off at approximately 3 ns with a low statistical variation.

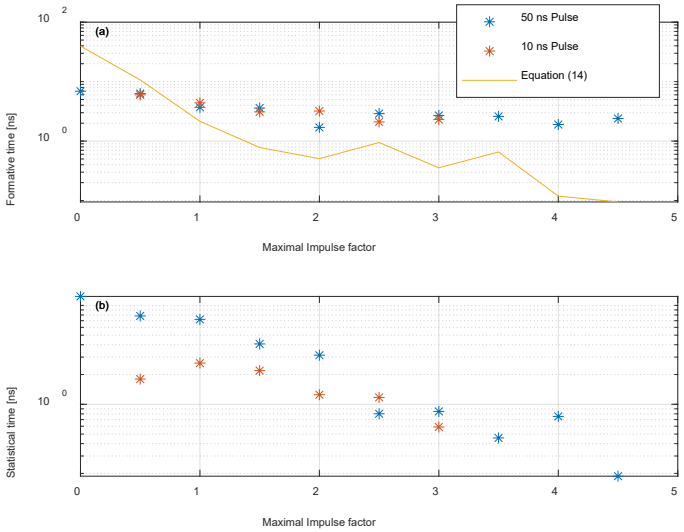

Figure 35: Pulsed discharge formative and statistical delay time

Figure 36 depicts the discharge probability (number of breakdowns divided by number of applied pulses) and the measured impulse factor as a function of the maximal impulse factor in subplots (a) and (b), respectively. For subplot (b), the error bars depict the minimal and maximal measured values. For maximal impulse factors above ~1.25, discharge is always present. When the discharge probability is below 100%, the measured impulse factor is limited by, and closely follows, the maximal possible impulse factor.

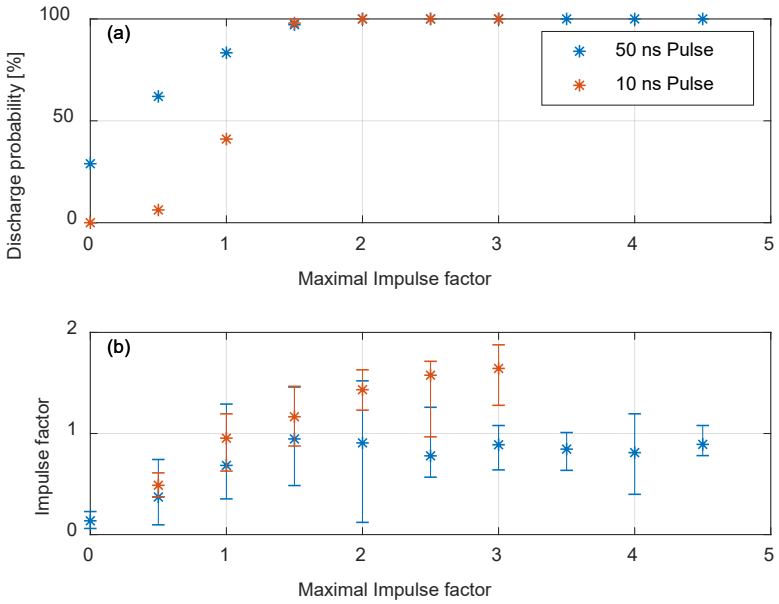

Figure 36: Pulsed discharge probability and measured overvoltage.

The results highlight the important role of seed electron provision for the breakdown under short transient voltages. The generation rate of seed electron is investigated in a controlled geometry. The

statistical time is evaluated as a function of pressure and simulated electric field. Evidence for a field-assisted emission of seed electrons from the cathode surface with a pressure-dependent onset field is found from time lag measurements. An empirical expression is derived to quantify the seed electron generation rate based on the Fowler–Nordheim formula. Figure 37 shows the seed electron generation rate. An open accedd pubication with these results is currently under review [34].

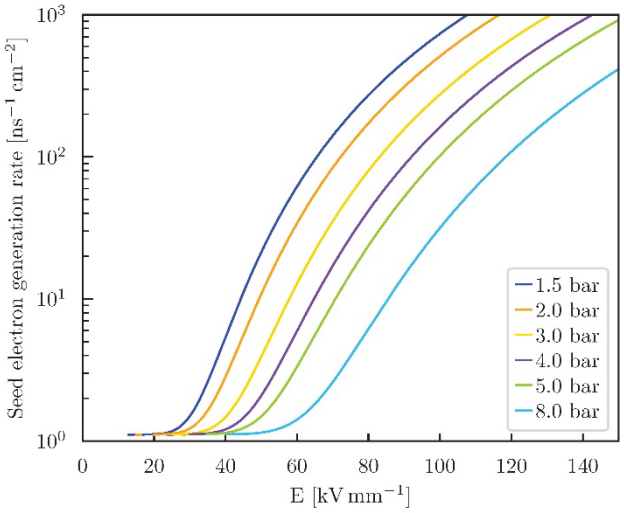

Figure 37: Seed electron generation rate as a function of the electric field

The reported results allowed setting up a proper control for the NRPD-based ignition in the engine setup (Section 2.1.2 and 3.1.2). Additionally, understanding the factors affecting the breakdown has allowed for developing a strategy for early ignition detection (a further paper is in preparation on this topic). The method used for ignition detection is to deliver an additional pulse after the main pulse sequence. After the main pulse sequence, the surrounding gas affects the plasma cooling. If the ignition is successful, lower heat losses are present from plasma to the surrounding gas because the temperature is lower (when compared to the case of failed ignition). The local density variation between the electrodes depends on the local temperature and on the occurrence of ignition or quenching. If enough time passes between the main ignition and the additional pulse (control pulse), variation in breakdown voltage will mirror the variation in local density. This allows for ignition detection.

Figure 37 shows two control pulses for two distinct experiments delivered 3 ms after the end of a sequence of 20 pulses at 10 kHz at 5 bar and λ=1.5. If ignition occurs, the measured breakdown voltage will be notably lower (blue line) than that of the incident pulse. For the other experiment, a high breakdown voltage (red line) signals quenching.

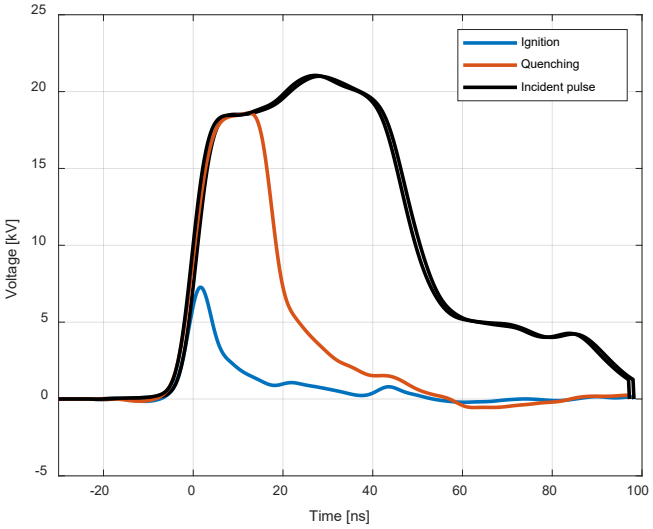

Figure 38: Control pulse gap voltage for an experiment where the ignition was successful (blue) and one experiment where no ignition occurs (red) (5 bar, λ=1.5, 20 pulses in the main ignition sequence, control pulse 3 ms after end of main ignition sequence).

This leads to the interesting possibility for ignition success prediction based on voltage or current measurement, as shown in Figure 39, where the measured breakdown voltage of the control pulse is shown for different delays between the main sequence and the control pulse. For each case shown on the x-axis, the experiments are divided between quenched cases (left) and successful ignition cases (right). In all the experiments, 10 pulses at 10 kHz are used as the main ignition sequence. The delay time between the last pulse in the main sequence and the control pulse is between 0.6 and 0.2 ms.

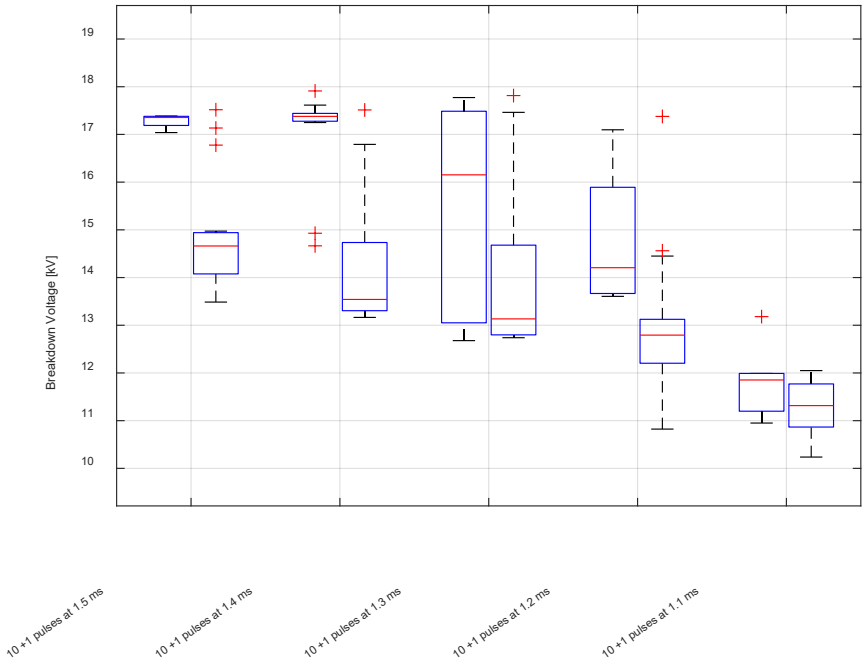

Figure 39: Control pulse breakdown voltage for different delays.

The value of the breakdown voltage predicts fairly accurately the ignition occurrence when the delay between the main sequence and the control pulse is above 0.5 ms. This delay offers a solution feasible for engine application.

Spark plugs were modified for the engine setup. The geometry was selected based on a preliminary investigation carried out in the constant volume cell (Section 2.3.4 and 3.3.7), where the evolution of the voltage between the sparkplug electrodes for two different sparkplugs was investigated [35]. Ten pulses at 10 kHz were applied, and the results are shown in Figure 40. The gap voltage for the first, second, third, and ninth pulses is shown in the upper subplots in different colors. The maximal voltages that would appear across the gap if no discharge were present are shown in black for the same pulses. The cumulative energy deposited into the plasma is plotted for the same pulses with the same color scheme in the bottom subplots. The tests showed that plasma creation efficiency is increased from 20 to 40% by replacing J-shaped sparkplugs with surface discharge sparkplugs.

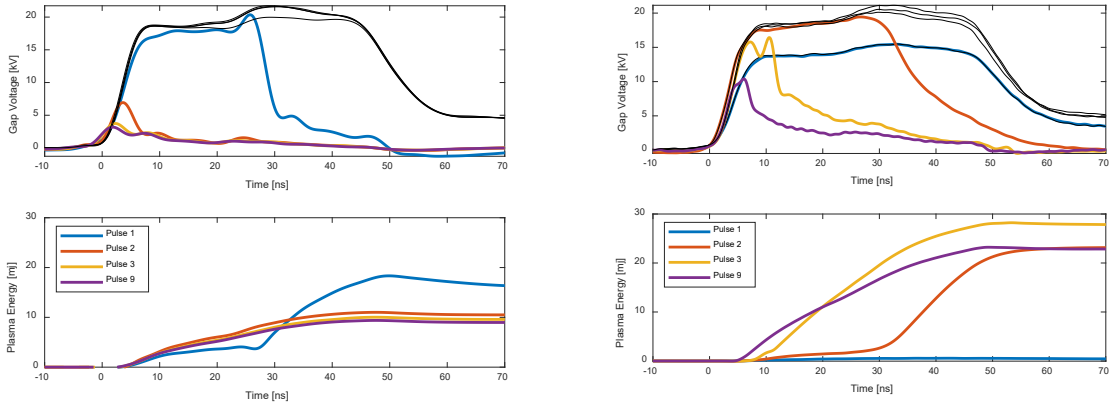

Figure 40: Different pulses voltages waveforms in a ten pulses NRPD at 10 kHz (left: surface discharge sparkplug; right: j-type sparkplug)

Therefore, the results reported in this Section were successfully used to set up the NRPD-based ignition in the running engine (Section 3.1.2).
Additionally, preliminary tests were performed with the aim of assessing the effect of EGR dilution on ignition. The percentage of successful ignition attempts over 40 repetitions was measured and plotted vs. the EGR % content over the total mixture (Figure 41). The tests were performed at 10 bar pressure and ambient temperature conditions. The results show that NRPD ignition extends the ignition limits for EGR diluted mixtures in the constant volume cell. Namely, while 40% ignition attempts are successful for inductive ignition at 20% EGR and no ignition was successful above this threshold, with NRPD it was possible to obtain 30% ignition success at 28.8% EGR. These tests, obtained in the constant volume cell in quiescent conditions and ambient temperature, will be used as a baseline for the evaluation of the ignition limits in the engine setup (Section 3.1.2).

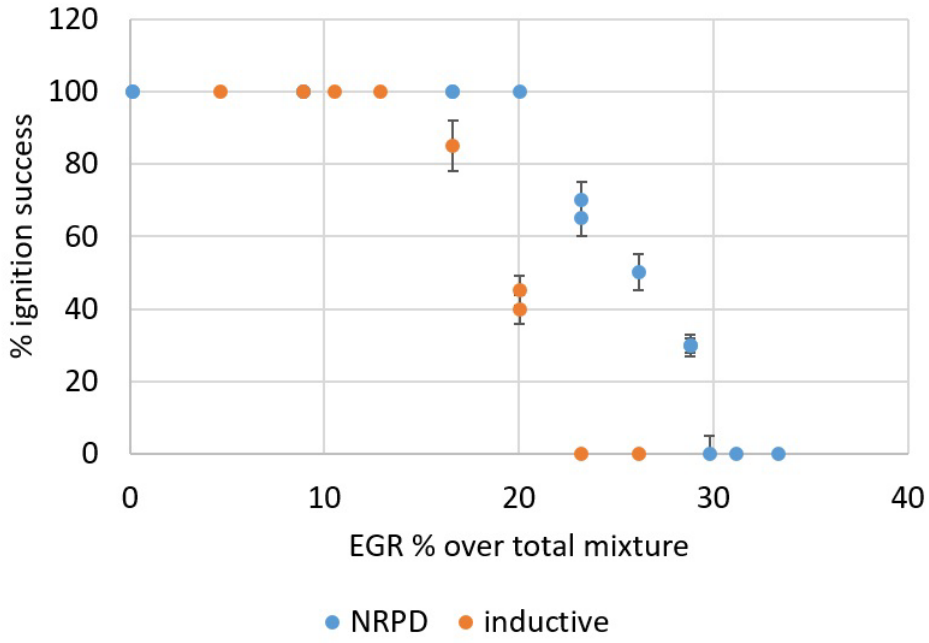

Figure 41: Ignition success vs. EGR content.

3.1.2 Full Engine Experiments

As a starting point and as a reference, the engine (as described in section 2.1.2) was operated with an inductive ignition system. For various relevant operating points, the effects of charge dilution by excess air and by low- and high-pressure EGR on all engine-relevant parameters were assessed. Exemplarily, the operating point with an engine speed of 1500 rpm and a brake torque of 100 Nm is discussed here.

Figure 42 (left) shows, for a standard inductive ignition system, the measured coefficient of variance (COV) of the indicated mean effective pressure (IMEP), evaluated from the cylinder pressure measurement of all four cylinders for 75 seconds. COV IMEP is a very good indication of the cyclic variability of combustion. For the inductive ignition system COV IMEP values below 3-5 % are regarded as stable combustion. At higher COV IMEP values, misfires start to hinder stable operations. Stochastic effects of fuel injection and mixing or stochastic effects in the turbulent flow field can induce cyclic variability. This variability gets critical at the flammability limits due to dilution. As Figure 42 (left) shows, the engine runs, with the classical inductive ignition system, stable until λ of about 1.6, and with higher air dilution, the cyclic variations increase quickly. Figure 42 (right) shows the effects of air dilution on ignition timing and apparent heat release rate for a constant center of combustion (COC) at 8 °CA. With increasing air dilution, the combustion becomes slower, and the ignition timing must be advanced to hold the COC position constant.

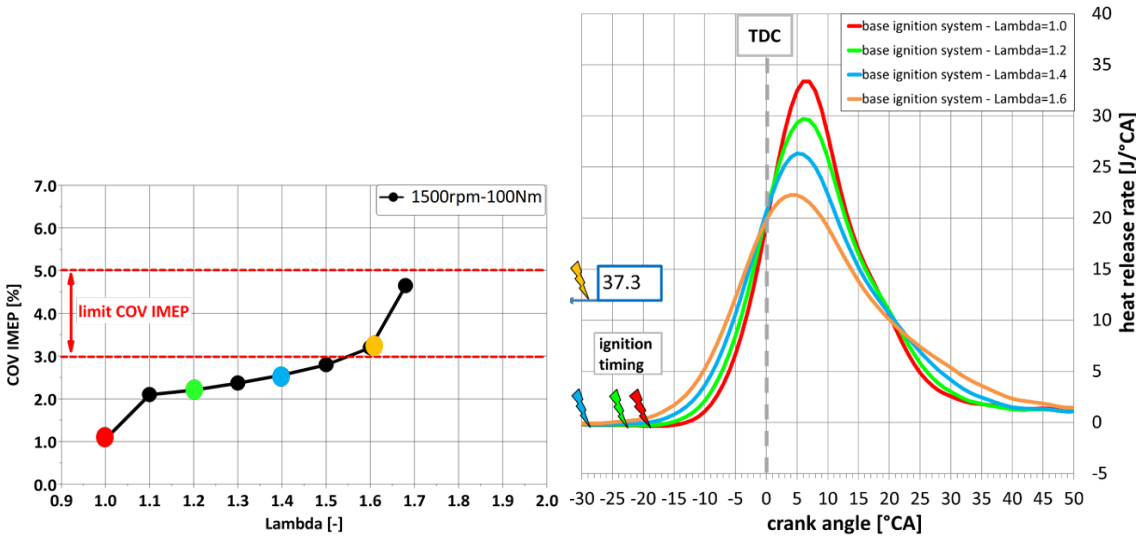

Figure 42: COV_{IMEP} (left) and heat releases (right) for increasing air dilution using an inductive ignition system.

Figure 43 shows the effect of EGR on the cyclic variability. Similarly to air dilution, the cyclic variability remains at good levels until a certain amount of dilution is provided. Interestingly, the EGR tolerance is higher for low-pressure EGR than for high-pressure EGR. Most likely, this effect can be attributed to a more homogeneous mixing of the exhaust gases with fresh air across the cylinders in the low-pressure EGR case. This assumption is supported by the apparent heat release rate evaluations shown in Figure 44.

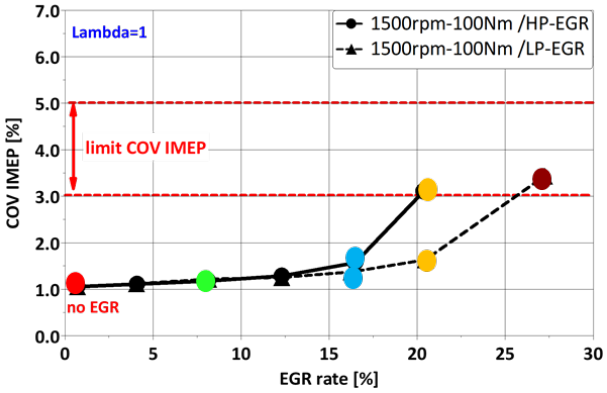

Figure 43: COV_{IMEP} for increasing high- or low-pressure-EGR dilution using an inductive ignition system.

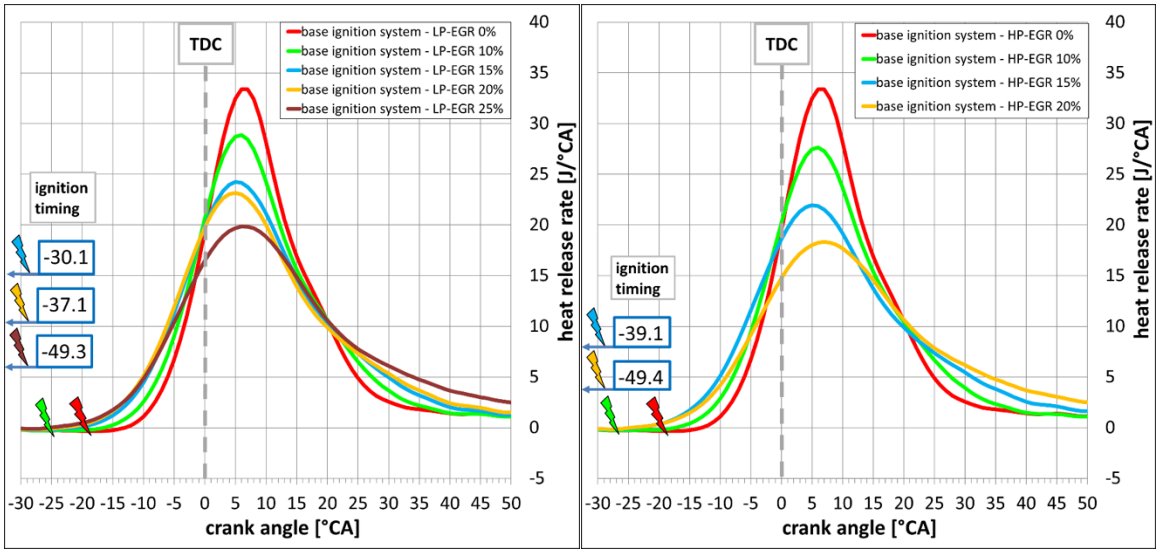

Figure 44: Heat releases for the different high- and low-pressure EGR cases using an inductive ignition system.

The engine setup was adapted to allow ignition by means of nanosecond repetitively pulsed discharge (NRPD), as described in Section 2.1.2. The successful update of the engine test bench for controlling NRPD-based ignition on a 4-cylinder engine is a novelty with respect to the available literature, and it builds the basis for further development, including pre-chamber configuration tests (which are not part of this project).

As mentioned in Section 2.1.2 a new sparkplug without the noise suppressor resistor has been manufactured and used for operation with NRPD. Due to the electrical scheme explained in 3.1.1, the presence of a typical sparkplug resistor (~5 kΩ) on the high voltage side would result in the pulse's complete reflection before the electrodes' gap, resulting in no spark and ignition. Figure 45 shows on the left side the CAD drawing of the modified surface discharge and j-type electrode sparkplugs with the open chamber insert, while on the right, the sparkplug with the resistor that was used for the inductive experiments.

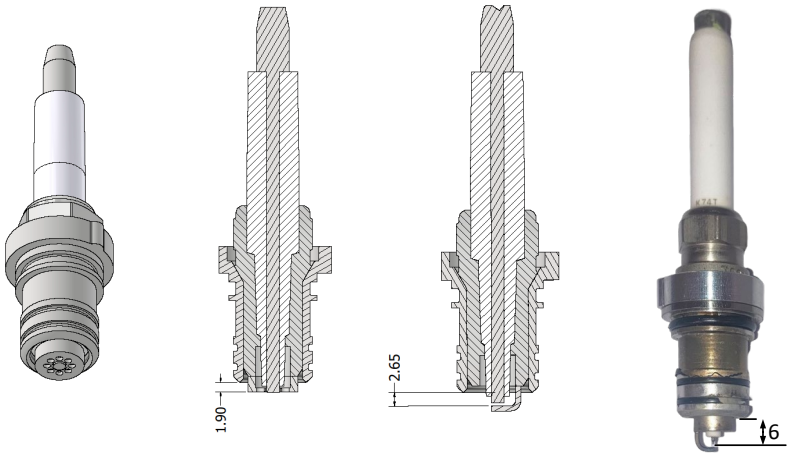

Figure 45: CAD drawings of the NRPD sparkplugs: surface discharge sparkplug and j-type electrode (left) and picture of the inductive sparkplug (right)

As shown in Figure 45, due to the impossibility of finding commercial long-reach sparkplugs without a resistor, the position of the surface discharge sparkplug used for NRPD is closer to the cylinder head than for the properly positioned inductive spark plugs (ca. 4mm). When the NRPD j-type sparkplugs are used, the position difference is approx. 3.5 mm.

The two different NRPD sparkplugs geometries are tested at the same operating point (100Nm and 1500 rpm). Both air and EGR dilution are tested until the ignition limit.

Figure 46 shows the efficiency variation for increasing lambda, and Figure 47 shows the efficiency variation for EGR. Both figures show the effect of inductive and NRPD ignition systems and the influence of different sparkplugs. The PRF for the NRPD ignition is varied from 5-to 100 kHz. Ten pulses are always supplied until lambda 1.7 or until 25% EGR; afterward, the number of pulses is increased to stabilize the combustion. No relevant difference has been recorded in the region where ten pulses were used when a higher number of pulses was used.

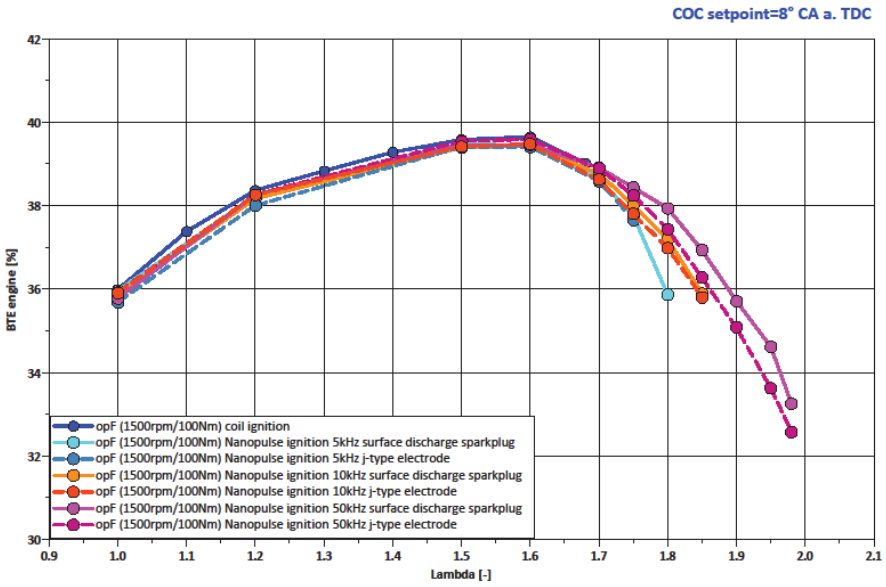

Figure 46: Engine's Brake Thermal Efficiency (BTE) variation versus air dilution

Below λ=1.7, no notable difference between the ignition concepts was present. In fact, changes in the NRPD discharge (number of pulses and PRF) did not lead to an appreciable difference. For λ above 1.7, higher ignition energies provided in a shorter time led to higher efficiency. For the same PRF and number of pulses, the use of surface discharge sparkplugs resulted in higher efficiencies.

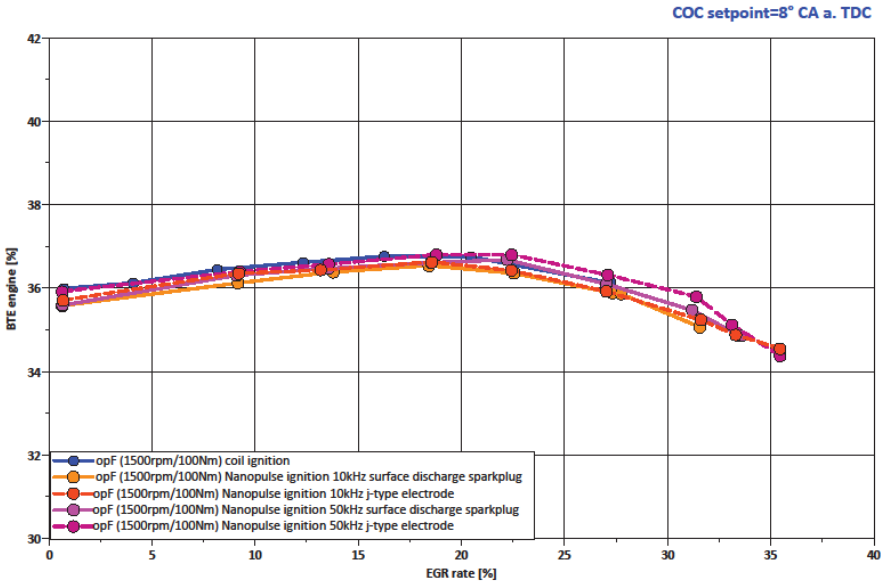

Figure 47: Engine's Brake Thermal Efficiency (BTE) variation versus EGR dilution

For EGR dilution, the differences are less pronounced than for air dilution. Above 20% of EGR, higher PRF resulted in slightly higher efficiency.

The efficiency increase reasons for air and EGR dilution are twofold: first, the pumping losses decrease due to the higher in-cylinder mass, and second, the fuel conversion efficiency increases by increasing dilution because the isentropic coefficient is higher. The fuel conversion efficiency increases more for air dilution than for EGR dilution due to the different isentropic coefficients. A tradeoff between isentropic coefficient increase and combustion stability for increasing dilution is present. In fact, the flame speed and combustion temperature decrease, resulting in lower temperatures and lower fuel conversion. The efficiency peaks at ca 39% for λ 1.6 and 37% for 25% of EGR. Figure 48 shows the total hydrocarbon (bottom) and the nitrogen oxides emissions (top) for air dilution.

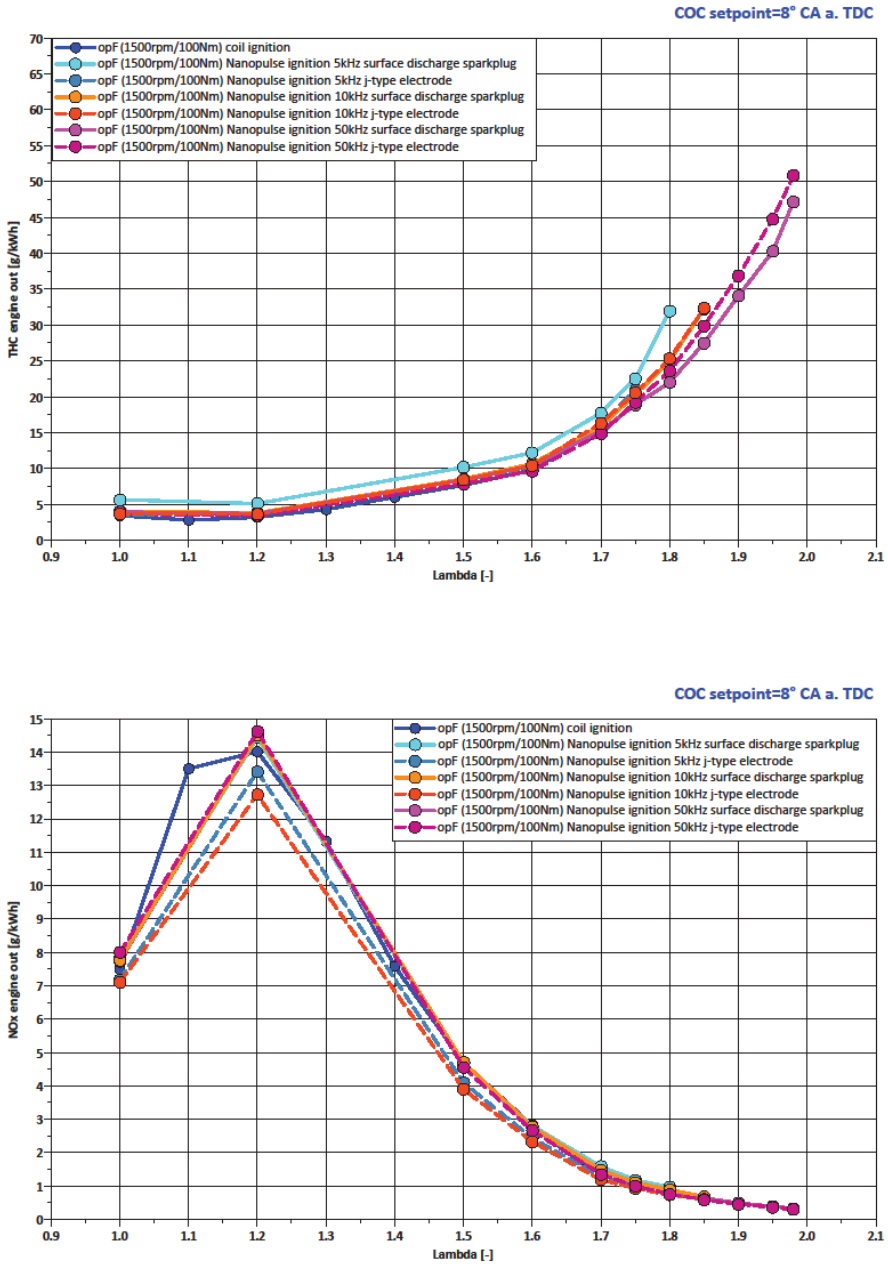

Figure 48: Total hydrocarbon (left) and nitrogen oxides (right) emissions for air dilution

The emission outlines the well-known trade-off with increasing dilution, flame speeds, and flame temperatures decrease. Therefore, the completeness of combustion decreases resulting in higher total hydrocarbon emissions but lower nitrogen oxides. It is interesting to notice that low nitrogen oxides (below 1 g/kWh) are reached above λ=1.8, where NRPD at high repetition frequencies allows for still high efficiencies (~38%). High number of pulses used at high dilution (up to 200) did not show any increase in the NOx level, which could occur in the neighborhood of the sparkplug due to the higher temperatures. The total hydrocarbon emission is nevertheless high (22 g/kWh) coming from a large

amount of air/fuel mixture being quenched in chevies and close to the (comparably cold) walls. It has to be mentioned that the combustion concept used here to determine the potential of NRPD in a running engine is not optimized for such lean operation. A stratified combustion concept could lead to much lower hydrocarbon emission. However, NRPD demonstrated impressively its potential to ignite a far leaner mixture compared to the classical inductive system. Figure 49 shows the total hydrocarbon and nitrogen oxides emissions for EGR dilution. Here again, NRPD showed the potential to ignite a more diluted mixture.

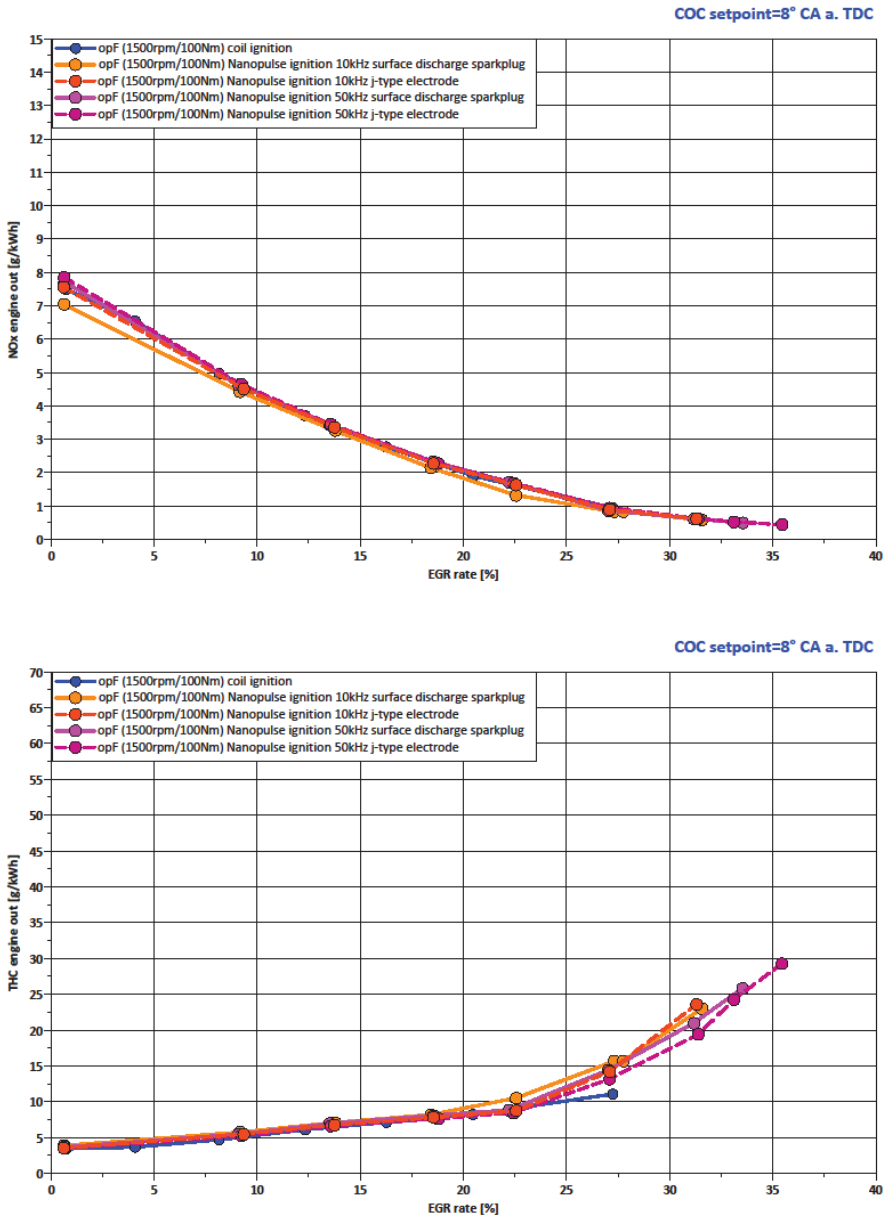

Figure 49: Total hydrocarbon (left) and nitrogen oxides (right) emissions for EGR dilution

Figure 50 shows the COV of IMEP for air dilution. With the inductive ignition system, when COV of 5% is approached, the ignition becomes unstable, and misfires hinder engine operation. In contrast, the

ignition can be stabilized using multiple pulses at high PRF. Even though the COV increases far above 5%, the engine still runs stable and without misfires.

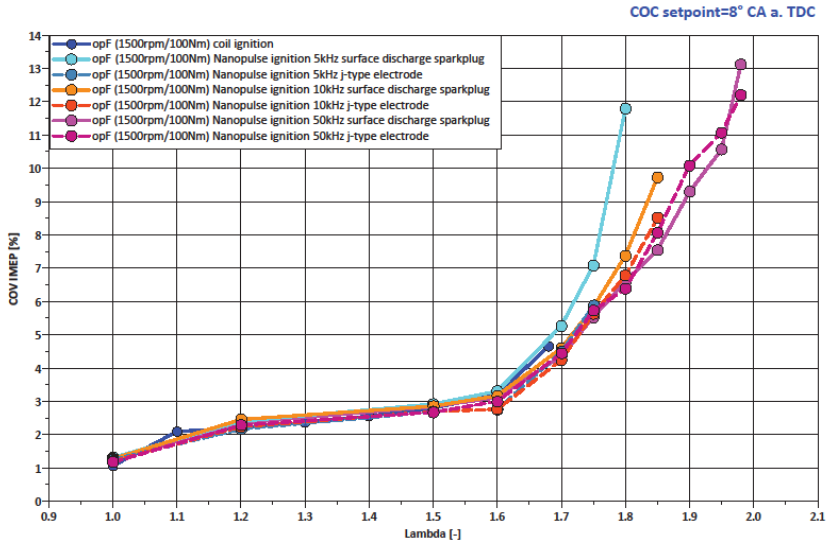

Figure 50: COV of IMEP for air dilution

A slow increasing COV is present between λ=1 and 1.6 where no differences in ignition strategy are present. Above λ=1.6, an abrupt increase in cycle-to-cycle variation is present. Stable engine operations with the inductive ignition system are not possible above λ 1.7. NRPD ignition, with increased pulses, is possible at higher AFR. The higher the PRF is, the lower the rate of increase of COV, which probably increases due to thermodynamic effect not dependent on the ignition. Surface discharge sparkplugs result in slightly higher COV of IMEP, probably due to the sparkplug's position. Figure 51 shows the COV of IMEP for EGR dilution. Where similar trends but less accentuated as the one for AFR variation are present.

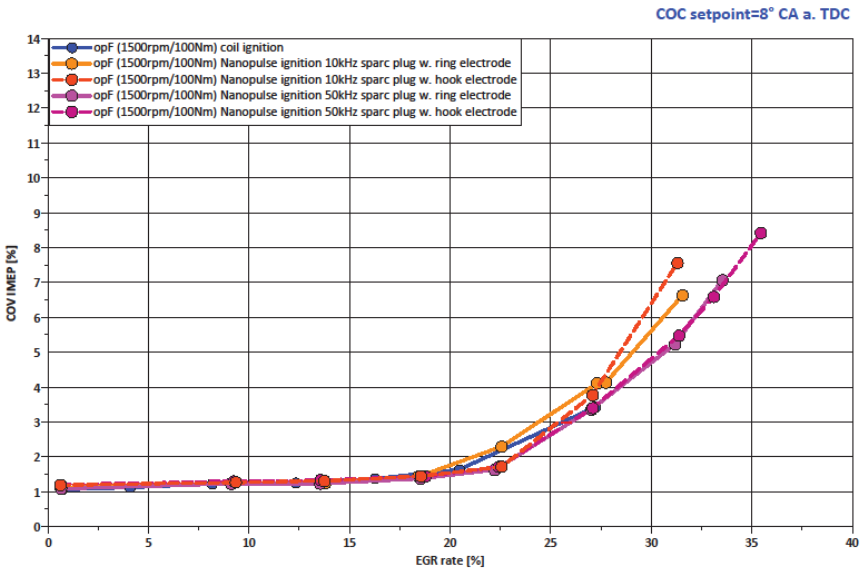

Figure 51: COV of IMEP for EGR dilution

The difference between inductive and NRPD ignition can be mostly seen when analyzing the ignition timing and the combustion delay (0 to 5% of the fuel burned) depicted, for air dilution, in Figure 52. The vertical red line shows the point where a higher number of pulses (>10) is used.

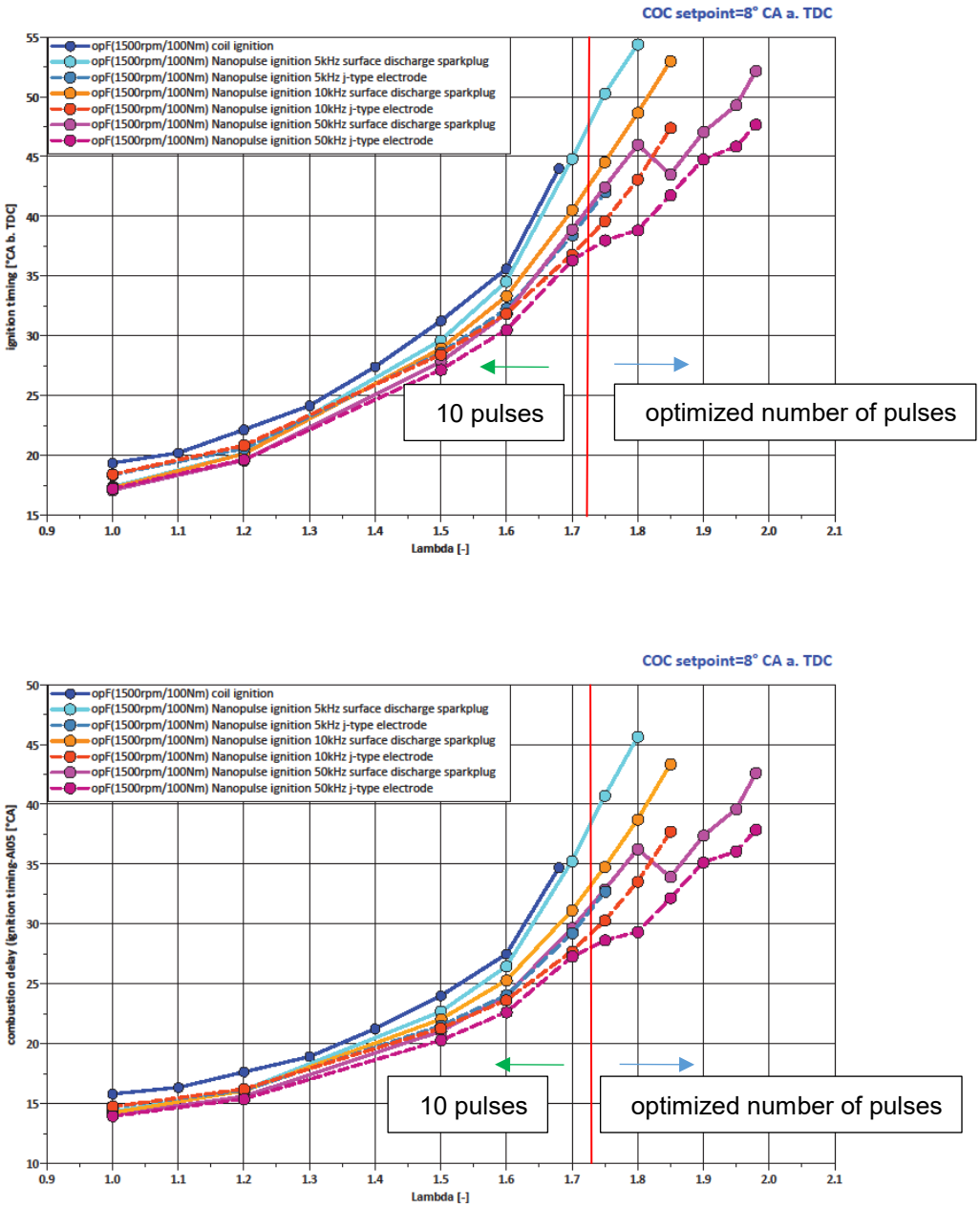

Figure 52: Ignition timing (top) and combustion delay (bottom) at different AFR, different PRF and sparkplugs

The combustion delay increases by increasing the air dilution. NRPD always gives a shorter combustion delay resulting in higher combustion stability. Higher PRF results in shorter combustion delay.

Below the red line, an increase in the number of pulses had a negligible effect. Therefore, the number of pulses was set to 10. Above, the combustion stability could be improved by increasing the number of pulses. PRF of 50 kHz allows reliably igniting very lean mixtures (λ>1.9). Above λ 1.7, high ignition energies provided in a short time (high PRF) are advantageous. At high dilution (λ>1.7) for NRPD ignition, the use of surface sparkplugs results in higher brake thermal efficiencies when compared to j-type ones, even though shorter combustion delays and advanced ignition times are present for the j-type electrode sparkplugs. One possible explanation is that the position of the j-type electrode sparkplug, which is slightly deeper in the combustion chamber, results in a faster inflammation (Figure 45). The advantage in the brake thermal efficiency of the surface discharge sparkplug could be due to the higher plasma creation efficiency presented in Section 3.1.1.
Figure 53 shows the ignition timing and combustion delay (0 to 5% of the fuel burned) for EGR dilution.

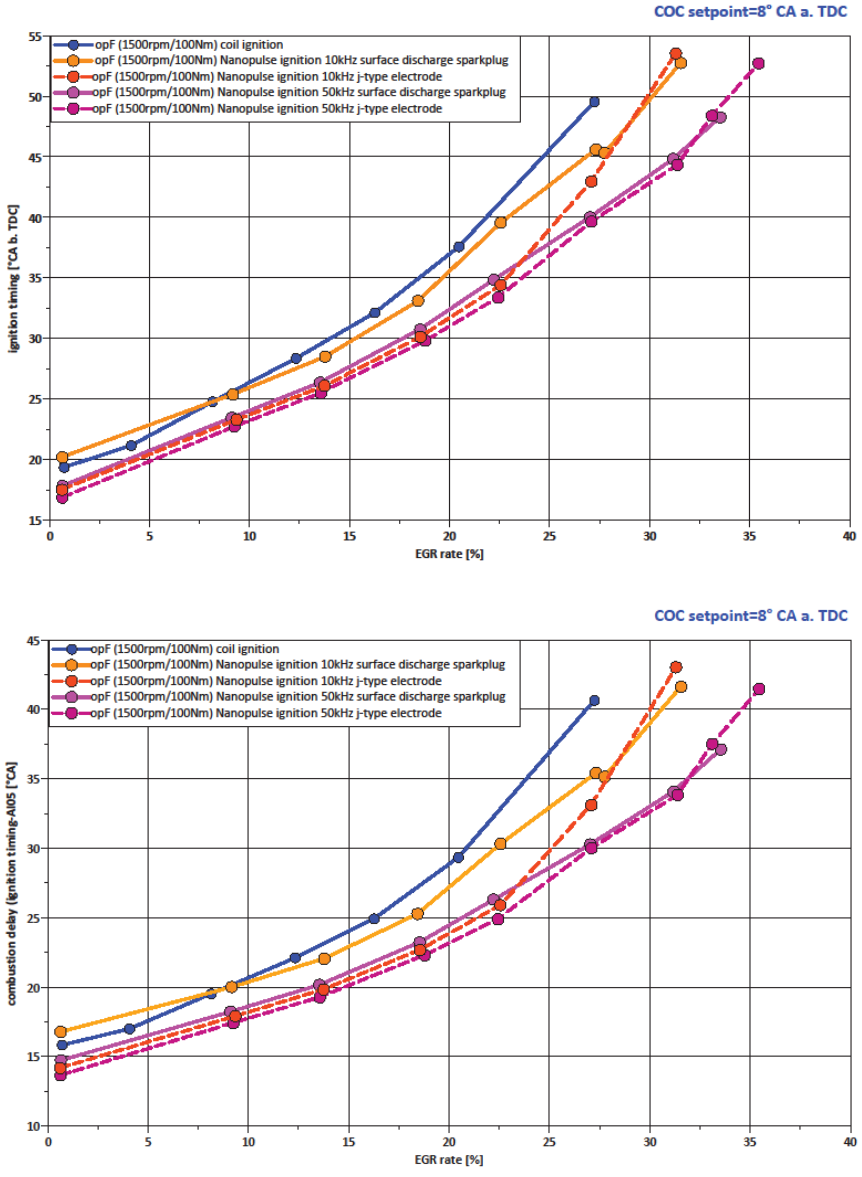

Figure 53: Ignition timing (top) and combustion delay (bottom) at different EGR rate, different PRF and sparkplugs

With EGR dilution, the ignition timing and the inflammation phase (0-5% of fuel mass burned) are shorter when NRPD ignition is used. The only minor exception is at 0% EGR with the surface sparkplug at 10 kHz. With NRPD ignition, a higher PRF results in retarded ignition timing and shorter combustion delay. The j-type sparkplug gives again advanced ignition timings. For EGR rates below 20%, the number of pulses is constant at ten pulses; afterward, the number of pulses is increased to guarantee stable combustion.

The lean limit and the EGR dilution can be successfully extended using NRPD. Operation up to λ of ~2 and 35% of EGR are achieved at high repetition frequencies without detecting any misfire. Minor differences between inductive and NRPD are detected where stable ignition can be guaranteed with the inductive ignition system. The non-optimal location of the sparkplug for NRPD (closer to the cylinder head) could decrease the advantage of NRPD. Further investigations on this topic are planned. In particular, the use of a surface discharge sparkplug with a long reach.

With NRPD ignition, severe sparkplugs erosion has been detected. Figure 53 shows the surface sparkplug electrodes on the top left side before the experiments while on the top right after ca. 30 hours of engine operation at 1500 rpm. The j-type sparkplug is shown on the bottom left side before the experiments and on the bottom right after ca. 10 hours of engine operations.

Figure 54: Sparkplug wear under NRPD ignition for surface discharge sparkplug (top) and j-type electrode (bottom)

The material used is a Nickel alloy which is the material with the lowest specification against erosion used for sparkplugs, experiments using different materials are planned in the future. The erosion is probably caused by the high temperatures created by the high currents present at the end of the nanosecond discharge. One effective way to reduce the discharge currents is to add a resistor on the coaxial cable's shield in the neighborhood of the sparkplug. The effect is like increasing the cable impedance, which results in a limiting of the current. When a low resistive plasma is formed, the current equals twice the pulse voltage over the cable impedance.

A 50 Ohm non-inductive resistor has been connected between the sparkplug hexagon (ground) and the coaxial cable shield in the constant volume cell. Ten nanosecond pulses are delivered to the j-type sparkplug in atmospheric conditions, with and without the resistor. Figure 55 shows the difference during the 10^{th} pulse for both experiments. The top plot shows the current in blue and the voltage in

red, the dashed line is used for the measurement without the current limiter resistor, while the full line is used for the experiment with the resistor. The bottom plot shows the reflected current waveform at the gap.

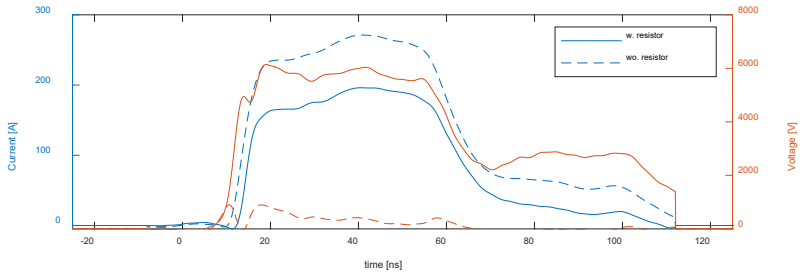

Figure 55: Effect of the current limiting resistor

After a few pulses, all the remaining have similar currents, and voltages waveforms like the one plotted in Figure 55. The resistor can be successfully used to reduce the current (~80 A reduction) at the 10th pulse. The breakdown voltage, which is the point where the minimum of the reflected current is present (bottom plot in Figure 55), is much higher for the case with the resistor (5 kV vs. 1kV). The breakdown voltage correlates with the local density. Since the pressure has enough time to equilibrate between pulses, the temperature is expected to be lower. The ideal resistor value to keep the temperature low is probably around 100-200 Ohm. The resistor dissipates a relevant part of the pulse energy. The energy to the plasma is nevertheless dependent on the multiplication of voltage and current. The higher breakdown voltages present with the resistor could even lead to higher energy deposition to the plasma. The high voltage and lower temperatures result in much higher reduced electric fields (voltage over distance and density). The energy is less channeled into heat and more in excitation, dissociation, and ionization with the resistor. Further analysis and a discharge model are in development to understand these effects.

The decrease in efficiency with NRPD at λ between 1.6 and 1.8 is lower than the one caused by the completeness of combustion decreases (depicted in Figure 56). An interesting combustion concept to follow could be a stratified charge to reduce the THC emission by reducing the fuel present near the walls where quenching occurs while still keeping a low maximal AFR to keep the NOx emission low.

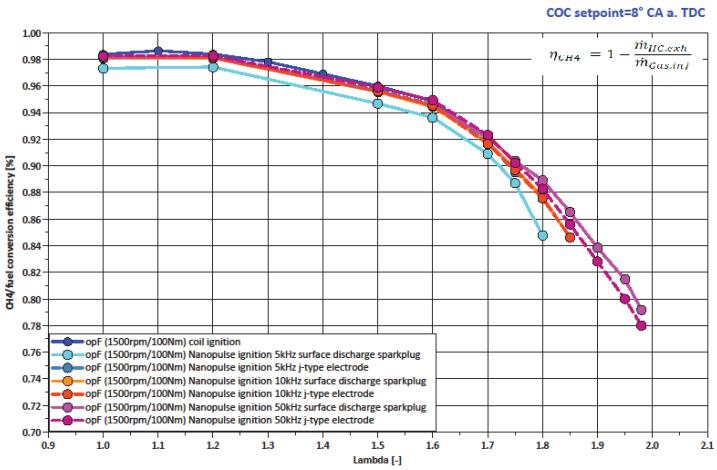

Figure 56: Fuel conversion efficiency

Furthermore, a passive prechamber or a prechamber sparkplug with NRPD could lead to a good ignition concept. With such a concept, very lean mixtures could be ignited thanks to NRPD, and the advantage of turbulent jet ignition on efficiency increase could be exploited with a simple setup.

Further investigations on NRPD to assess the influence of sparkplug geometry, position, and the combination of prechamber and NRPD are still ongoing in the course of the ongoing PhD thesis of M. Balmelli.

3.2 WP2: EGR Control

Following the procedure stated in section 2.2.4, the final project achievements concerning EGR control are the following:

- A library of grey-box models for components of engine air paths has been developed. These are specifically designed for their application in optimization algorithms and algorithmic differentiation. A short overview to the model library is given in section 3.2.1.
- The control structure illustrated in Figure 13 was derived and used to generate controllers for two engines. The light-duty engine was used to demonstrate a pumping-loss optimal air path controller, as described In section 3.2.2. The transfer of an existing algorithm to another engine of different size and air path configuration was demonstrated with the heavy-duty engine. Results are stated in section 3.2.3.
- For the automated C code generation and the deployment of the algorithm to the RCP hardware, the open-source software “acados” is used [36]. In order to fit the requirements of the derived control structure, the functionalities of “acados” were considerably extended in a collaboration with the University of Freiburg, Germany, which developed this software. The derived functionalities are now part of the software and available to everyone.

A publication of the results presented in the sections 3.2.1, 3.2.2 and 3.2.3 is currently under review [17]. Also, in the coming months these results will be published as part of a PhD thesis.

3.2.1 Modeling and Identification

The formulation of the air path component models is the major challenge for optimization based controllers. They considerably affect the control precision, the algorithm robustness and the computational effort of the resulting controllers.

Models were derived for the following components: Control volume, gas transport time delay, throttle valve, engine block (volumetric pump), turbine mass flow, turbine efficiency, compressor mass flow, compressor efficiency, turbocharger speed, and intercooler.

As examples, Figure 57 shows the model functions for the normalized throttle valve opening area (left) and the turbine mass flow (right).

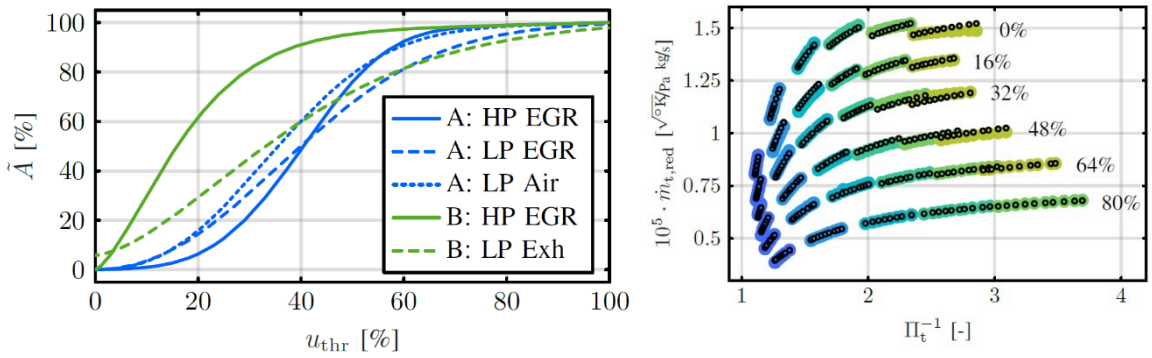

Figure 57: Identified models of the normalized throttle areas of all throttles of both engines (A: light-duty engine, B: heavy-duty engine) (left) and the model of turbine mass flow, identified with turbocharger map data (black: model, colored: map data, numbers: variable turbine geometry position) (right). Graphics are taken from [17] .

Given all these components, the complete air path models for both engines can be derived and identified.

Table 2 states the steady-state accuracy of the two models for the identification as well as for a validation data set. The numbers indicate that the models are precise enough for the determination of control strategies for complex air path systems.

Table 2: R^2 values (upper) and root-mean-square error values (lower) of the intake and exhaust manifold pressure, the oxygen concentration upstream of the compressor, the intake and exhaust oxygen concentration and the turbocharger speed (A: light-duty engine, B: heavy-duty engine). Graphic is taken from [17].

	p_{im} [bar]	p_{em} [bar]	F_{bc} [%]	F_{im} [%]	F_{em} [%]	ω_{tc} [krpm]
A: $\mathcal{D}_{\mathrm{id}}$	99.7	99.0	99.0	98.4	97.7	99.7
$n_{\mathcal{D}} = 323$	0.02	0.06	0.15	0.28	0.50	1.88
A: $\mathcal{D}_{\mathrm{val}}$	98.2	96.5	98.7	90.2	85.0	98.8
$n_{\mathcal{D}} = 89$	0.04	0.14	0.29	0.83	1.21	4.32
B: $\mathcal{D}_{\mathrm{id}}$	99.0	98.1	-	95.4	97.9	99.2
$n_{\mathcal{D}} = 290$	0.05	0.07	-	0.16	0.55	2.31
B: $\mathcal{D}_{\mathrm{val}}$	94.2	96.4	-	96.7	97.9	95.1
$n_{\mathcal{D}} = 67$	0.02	0.05	-	0.20	0.22	2.25

3.2.2 Pumping-Loss Optimal Air Path Control

A comparison of the two steady-state measurement data points of the light-duty engine stated in the table of Figure 9 shows that the choice of the EGR path can have a considerable effect on the engine efficiency. For the specific operation point stated, the use of high-pressure EGR results in a higher exhaust manifold gas pressure, which leads to increased pumping losses and a reduced engine efficiency. The use of an air path controller which tracks the intake manifold gas conditions under consideration of pumping losses would be able to automatically choose the right split between high-pressure and low-pressure EGR. Such a controller can be realized with the proposed control structure.

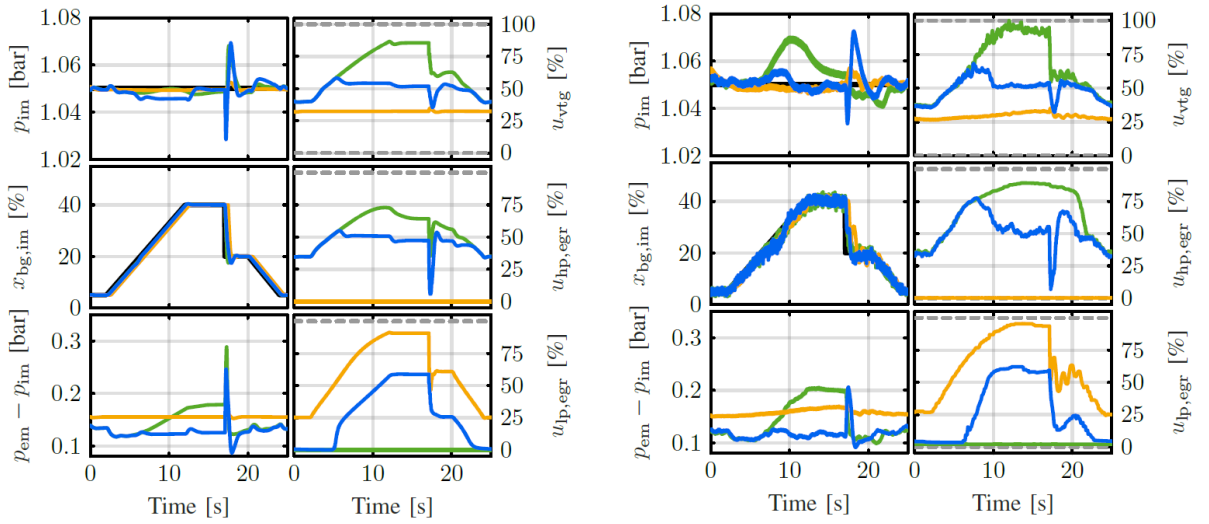

Figure 58: Comparison of a high-pressure EGR controller (green), a low-pressure EGR controller (yellow) and the pumping-loss optimal dual-loop EGR controller (blue) in simulation (left) and on the light-duty laboratory engine (right). The controllers track the two references intake pressure (top left) and burnt-gas ratio (middle left) with the variable turbine geometry actuator (top right), the high-pressure EGR throttle (middle right) and the low-pressure EGR throttle (bottom right). Pumping losses are illustrated in the bottom left corner of the plots. Graphics are taken from [17].

The target selector finds the pumping-loss minimal split, and the NMPC algorithm tracks this split.

In Figure 58, simulative as well as experimental results of the developed controller are illustrated and compared to controllers which only use high-pressure EGR or low-pressure EGR. As shown, the pumping losses are considerably lower with the derived dual loop controller. High- and low-pressure EGR are correctly combined in order to reduce the exhaust pressure as much as possible for given

intake manifold pressure and burnt-gas ratios. A second observation is that the system behavior in simulation is highly similar to the real system, indicating a high model precision intake manifold.

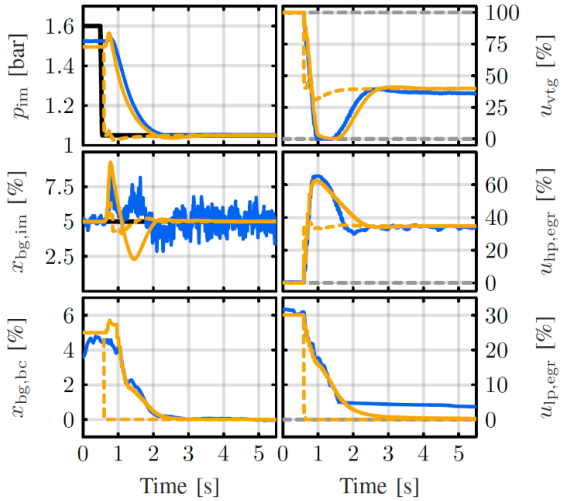

Figure 59: Controller behavior of a step in the intake manifold gas pressure reference, once simulated (yellow) and once measured with the light-duty engine (blue). Graphic is taken from [17].

A further example that demonstrates high model precision as well as the fast and precise air path control is given in Figure 59. For a step in the intake manifold pressure reference, the algorithm actuates the variable turbine geometry as well as the high-pressure EGR throttle at the maximum actuator speed in order to reach the new reference as fast as possible.

3.2.3 Algorithm Transfer and Control Performance

Only a few adaptions were necessary to transform the controller of the light-duty engine to a heavy-duty air-path controller. Namely these were:

- Re-arrangement of individual component models in order to represent the heavy-duty air path configuration.
- Identification of the individual components with measurement data.
- Definition of the control algorithm tuning parameters in simulation.

The resulting algorithm has been implemented on the heavy-duty engine and slightly tuned for multiple operation points. Then the algorithm was compared to a linear control approach which was tuned for the specific engine operation point, and which is sampled 50 times faster than the developed controller based on NMPC. The comparison of these two algorithms is shown in Figure 60 in the left plot. Even though the linear approach is updated much faster and is specifically tuned for the engine operation point, it performs worse than the developed NMPC approach. Cross-couplings are stronger and the tracking of the reference values is slower. These results show the effectiveness of the control approach derived.

A further advantage of optimization-based algorithms is that their behavior can be adapted during operation. This effect is demonstrated in the right plot of Figure 60. During changes of the operation point, once the algorithm was tuned to prioritize the tracking of the pressure, and once it was tuned to prioritize the burnt-gas ratio. As illustrated, the algorithm behavior completely changes depending on the signal it prioritizes.

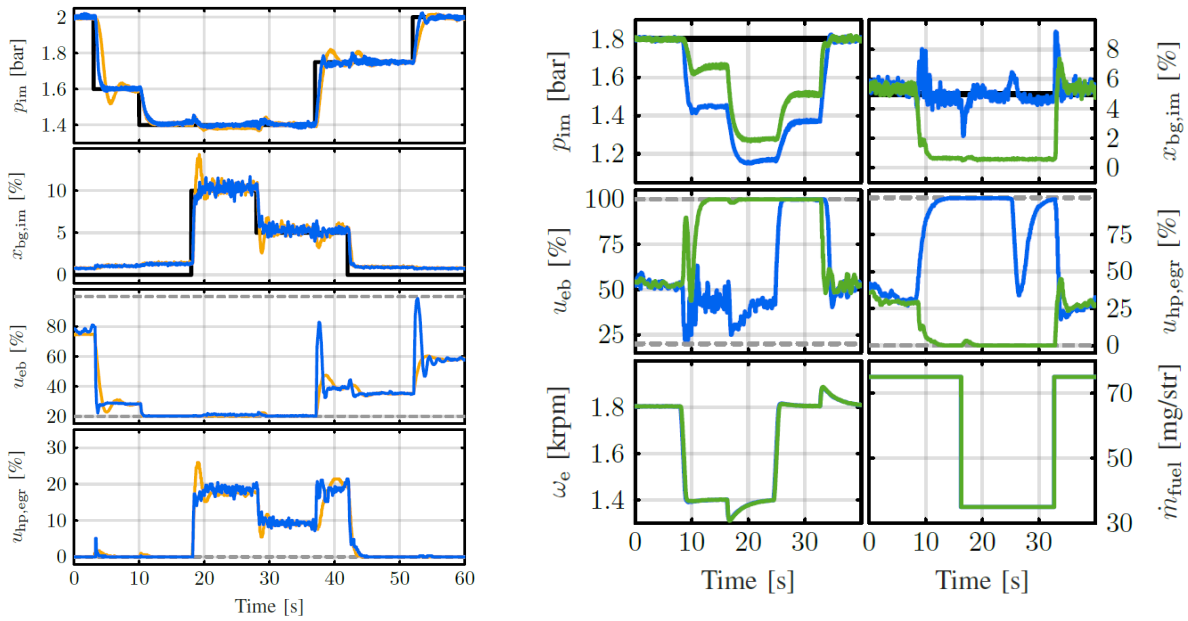

Figure 60: Comparison of the derived controller with a linear control approach (left, NMPC approach in blue, linear approach in yellow), and illustration of the influence of cost weights in the target selector to the control behavior (right, tuning for intake pressure in green, tuning for burnt gas ratio in blue). Graphics are taken from [17].

3.2.4 Intermediate Project Achievements and Teaching

As mentioned in section 2.2.4, the algorithm presented within the last chapters was developed in a two-step process. Within the first step, an algorithm designed to control simple air path structures as well as an own toolchain for the C-code generation and deployment on an RCP were developed. These algorithms are still used to teach nonlinear model predictive control for master students at ETH Zurich. Students use these tools to derive a controller for the light-duty engine air path without considering low-pressure EGR. A model validation as well as an experimental validation of a control algorithm that is derived by students is shown in Figure 61.

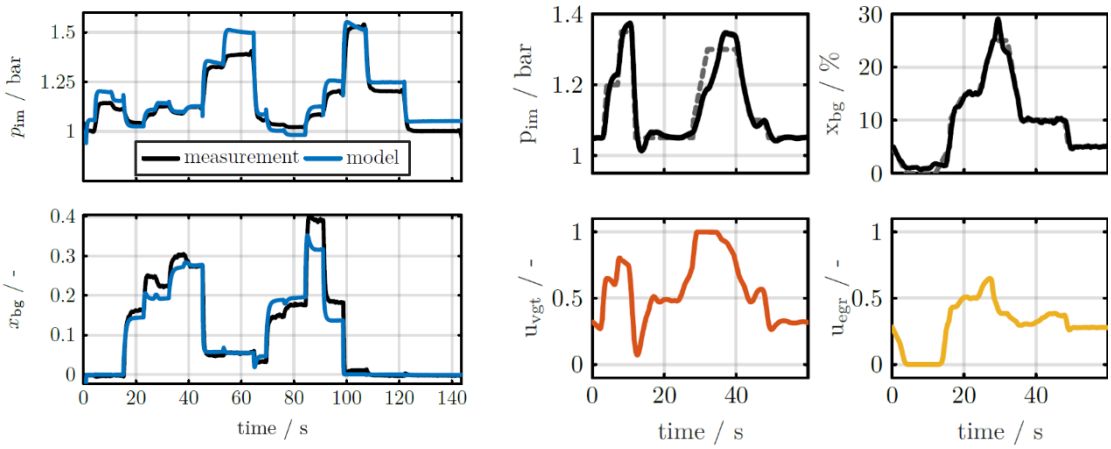

Figure 61: Model Validation (left) and control algorithm validation (right) on the light-duty engine for the simplified control algorithm which only considers high-pressure EGR. This simplified control task is used to teach NMPC in a lecture at ETH.

Two publications address the simplified control problem. A case study of the control problem treated in the lecture exercise can be found in [37]. The general topic of teaching nonlinear model predictive control for engine applications including exercises on an engine test bench is published in [18].

Besides the lecture exercise, the control tasks of the REAL project were the topic of three master theses, two semester theses and one doctoral thesis. The models and software developed are further used in other projects.

3.3 WP3: Optical and Numerical Methods

Measurements in an optically accessible constant volume combustion chamber were performed for a variety of combinations of injection and cell backpressure. The spray penetration was characterized by means of high-speed Schlieren imaging; while information on the state of mixing was obtained using a tracer added to the fuel and Laser Induced Fluorescence (LIF) imaging techniques. Reactive conditions further employed OH* chemiluminescence imaging to provide information w.r.t. high-temperature combustion. At low injection temperatures and high pressure ratios, condensation of the gaseous fuel due to the high pressure drop was observed. At engine relevant temperature/pressure ratios and injection temperatures, such effects were found to be negligible. Different ignition sources to ignite the underexpanded jet were further examined in an engine-like test rig with optical access. These included a glow-plug, a diesel pilot as well as a pre-chamber ignition system. To obtain further insights w.r.t. the processes occurring inside the pre-chamber, an Optical Pre-chamber was further studied for different spark ignition configurations, namely a standard inductive spark plug as well as nanosecond repetitively pulsed discharges, the latter evidencing considerably improved ignition reliability.

These experimental investigations were complemented by three-dimensional Computational Reactive Fluid Dynamics, showing very good agreement with the measurement validation data from the constant volume combustion cell, following the development of a numerical framework capable of taking into account I.) real gas effects for the equation of state (required for accurate predictions of the spray morphology behavior), II.) an enthalpy departure formulation (to reproduce accurately the temperature field) and III.) albeit to a lesser extent, real gas transport properties. At auto-igniting conditions, the results were found to depend strongly on the choice of the chemical mechanism. In addition, the presence of strong temperature stratification due to the pre-combustion event in the constant volume combustion chamber led to strong discrepancies in the predictions. Assessing the

simulation results with shock tube and additional constant volume combustion vessel data from literature showed good predictive capabilities in terms of the trends for the developed numerical framework.

3.3.1 Experimental conditions

The total matrix was composed of multiple different conditions, which included variations in injection pressure from 75-300 bar, chamber pressures of 5-60 bar, which lead to pressure ratios of 2.5-25; and ultimately variations in ambient temperature of 850-1250 K. The study was divided in two parts, which is how the results will be presented.

The experimental campaigns were designed to study specific parameters and to provide validation data for the numerical models presented in the previous chapters. The experimental matrices are presented in Tables and will be discussed in the upcoming sections. The campagins were designed in order to study the following parameters:

- The first studied the effect of the contour conditions on the tip penetration, in this part the injection and chamber pressure will be varied, which will result in different pressure ratios. Two different test rigs were used to study the effect of the penetration under steady and transient conditions (Table 3 and Table 4).
- The second analysed the possibility of re-condensation of the methane and how to eliminate it, for this the injection and ambient temperature were increase (Table 5).
- The third study focused on the mixing and mass fraction distribution, for this the injection pressure and pressure ration were varied under non-condensing conditions (Table 6).
- The fourth and last campaign studied the feasibility of auto ignition of a methane jet without any aids (i.e. spark plug, glow plug, pilot injection). For this, the ambient temperature was changed as well as the injection pressure (Table 7 and Table 8).

The pressure ratio is defined as the quotient between the injection- and the chamber pressure:

$$P_r = \frac{P_{inj}}{P_{ch}}$$

Table 3: Overview of the experimental conditions. Injection and chamber temperature 294K.

Pinj [bar]	**Chamber pressure [bar]**							
75		15	10					
100	40	20		10		5		
125		25						5
150		30			10			
175		35				10		
200		40						
250		50						
300		60		30	20		15	12
	2.5	**5**		**10**	**15**		**20**	**25**
	Pressure ratio [-]							

Table 4: Experimental matrix for the transient environment.

		Pressure ratio [-]			
		4	**6**	**8**	**10**
Pinj [bar]	**300**	75	50	37.5	30
	400	100	66.7	50	40
	500	125	83.3	62.5	50
		Cylinder pressure aSOI [bar]			

Table 5: Matrix of nominal operation conditions for the condensation experiments. Injection and ambient temperatures were changed from 294K to 363K.

		Chamber pressure [bar]				
Pinj [bar]	**200**	40	20	13	10	8
	250	50	25	17	13	10
	300	60	30	20	15	12
	Pratio [-]	**5**	**10**	**15**	**20**	**25**

Table 6: Matrix of conditions for the mixture fraction distribution. Injection and ambient temperatures were set to 363K.

		Chamber pressure [bar]				
Pinj [bar]	**200**	50	40	33	25	20
	250	63	50	42	31	25
	300	75	60	50	38	30
	Pratio [-]	**4**	**5**	**6**	**8**	**10**

Table 7: Experimental matrix for reactive conditions. Ambient temperature were changed according to Table 8.

		Pressure ratio [-]			
		4	**5**	**6**	**10**
Pinj [bar]	**200**	50	40		20
	250		50		25
	300		60	50	30
		Chamber pressure [bar]			

Table 8: Average chamber temperatures achieved at given chamber pressure and density.

	Chamber density [kg/m^3]								
	5.2	**7.5**	**8.0**	**9.8**	**10.3**	**11.7**	**13.3**	**15.2**	**17.0**
Pch [bar]									
20	1132								
25		954	895						
30		1165	1086	917	842				
40			1402	1231	1132	982	885	772	
50					1386	1248	1097	975	870
60							131	1167	1046
	Average chamber temperature [K]								

Table 9: Experimental matrix for ignition strategies in the optical engine.

Case	Tin [°C]	Spark / Pilot [°CA]	SOI [°CA]	Pinj [bar]	ET [us]	Ignition
1	100	-7.8	-6	300	3000	Pre-chamber
2	100	N/A	-6	300	3000	Glowplug
3	100	-5.3	-6	300	3000	Pilot

Table 10: Experimental conditions for tests performed in the optical pre-chamber.

Parameter	Unit	Value
Initial pressure	bar	12
Initial temperature	Kelvin	150
Air-fuel ratio	-	1-1.4-1.8
Dwell	s	0.005-0.5

3.3.2 Spray tip penetration

This section will present the influence of the injection pressure and pressure ratio on the tip penetration.

Figure 62 shows the evolution of the tip penetration at a pressure ratio of 5, while changing the injection pressure from 150 bar to 300 bar, and the chamber pressure from 30 bar to 60 bar. It can be seen that the top three pressures have very similar penetration curves, while the case with 150 bar remains below the others throughout the injection event. As seen on the work presented by Gerold et al. [38], the penetration curves fall on top of each other when the pressure ratio is the same. This seems to also be the case in the present experiments, despite the fact the start of injection is not exactly the same for the presented cases.

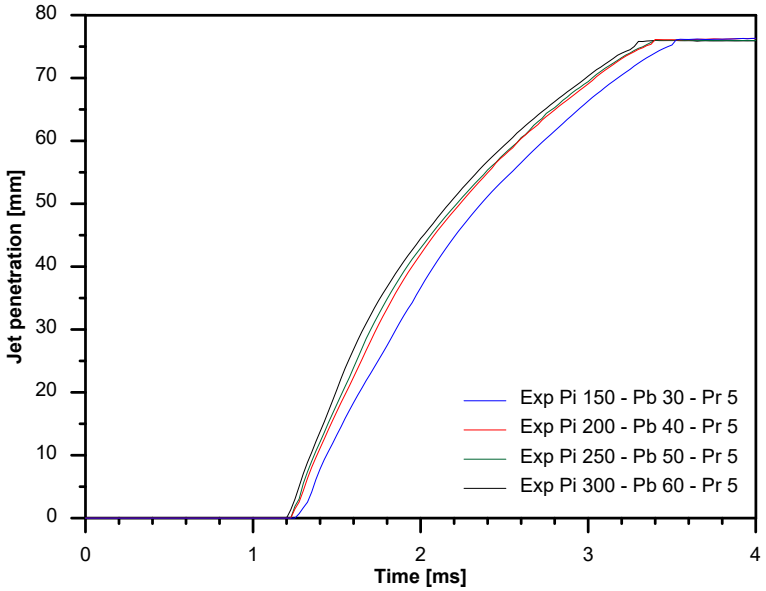

Figure 62: Effect of the injection pressure on the tip penetration.

Figure 63 shows the evolution of the needle movement and the tip penetration at an injection pressure of 300 bar, while changing the pressure ratio from 5 to 25, and the chamber pressure from 12 bar to 60 bar. It can be seen that when the pressure is higher the slope is steeper. This is because a higher pressure ratio leads to a greater nozzle exit velocity, which translates into a faster tip penetration. This trend can also be found in the literature[38], where the cases with higher pressure ratios penetrate faster.

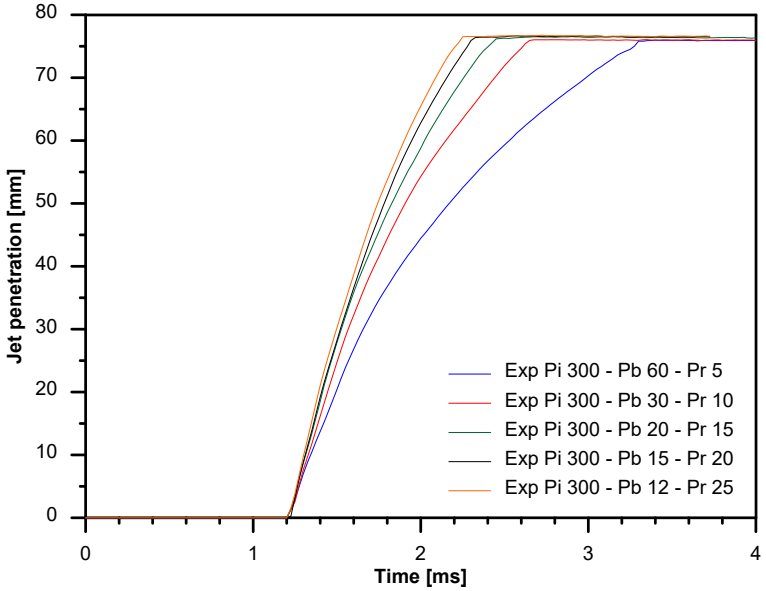

Figure 63: Effect of the pressure ratio on the tip penetration.

Injecting into the transient pressure environment of the optical engine meant that the chamber pressure and conversely the pressure ratio is changing during an injection event. As the back-pressure rises the pressure ration lowers for a given injection pressure as the piston nears TDC.

Penetration curves on Figure 64 (right) and Figure 65 (right) show that in these cases the injection pressure had a more noticeable effect on penetration, although the absolute total jet penetration duration difference between the cases may be too small to affect real life operation in an actual dual-fuel engine. The pressure ratio graphs on Figure 64 (left) and Figure 65 (left) display the variable nature of these values during injection, although for Figure 65 the goal was to have the same pressure ratio on all cases, the different pressure slopes during the compression stroke led to slightly different ratios along time.

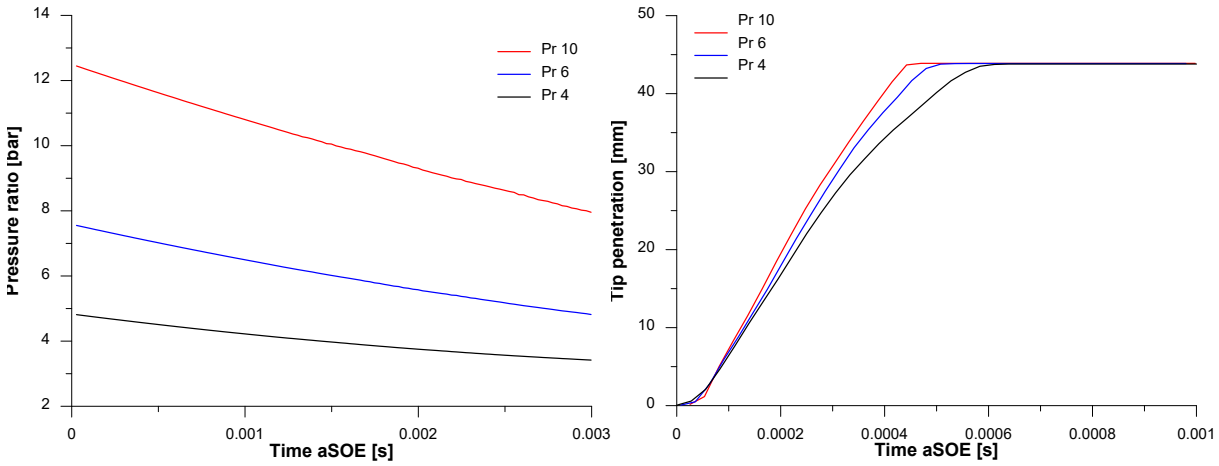

Figure 64: Pressure ratio (left) and tip penetration (right) at 500 bar of injection pressure and pressure ratios from 4 to 10.

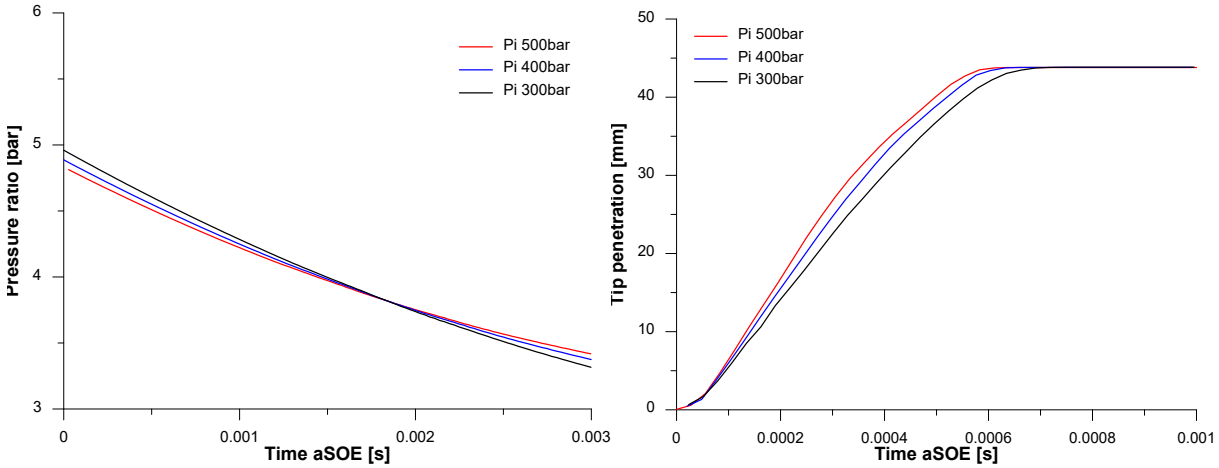

Figure 65: Pressure ratio (left) and tip penetration (right) at pressure ratio 4 and injection pressures and from 300 to 500.

3.3.3 Liquid core

Simulations performed by the UniBwM presented re-condensation of the methane on the near nozzle field at high injection pressures. Therefore, an experimental campaign was performed in order to corroborate such findings under the experimental conditions presented in Table 5.

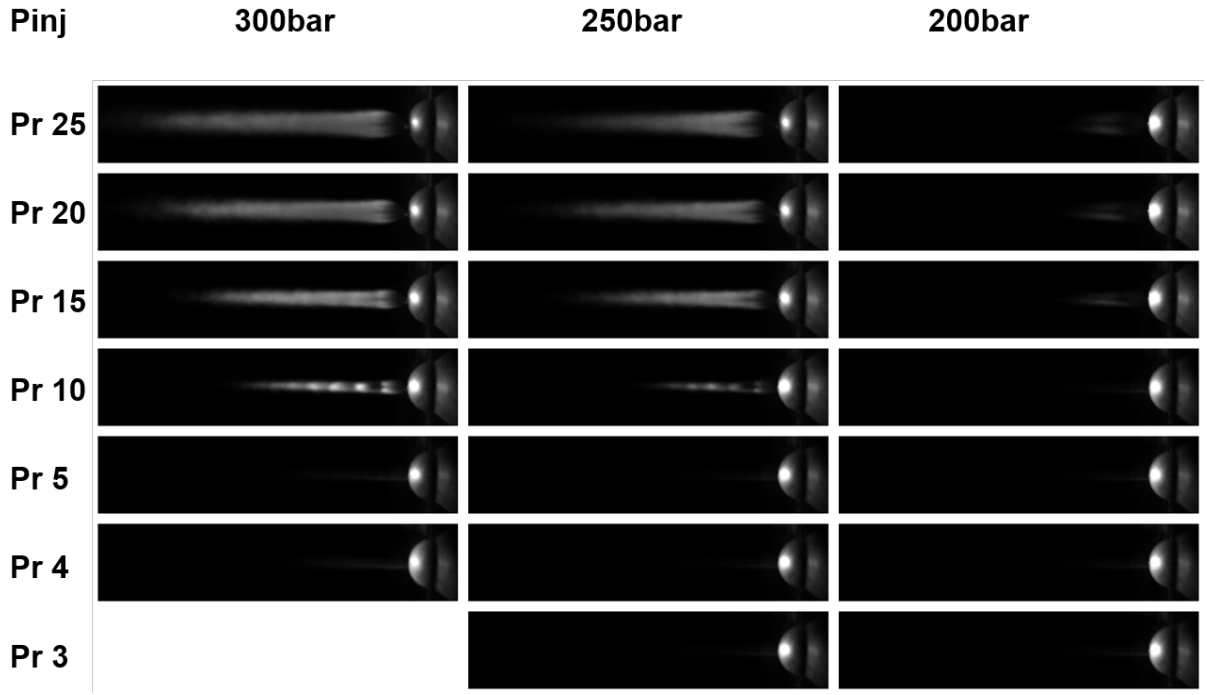

Figure 66: Averaged mie scattering images under variation of injection pressure and pressure ratio at 294 K of injection temperature and 294 K of air temperature.

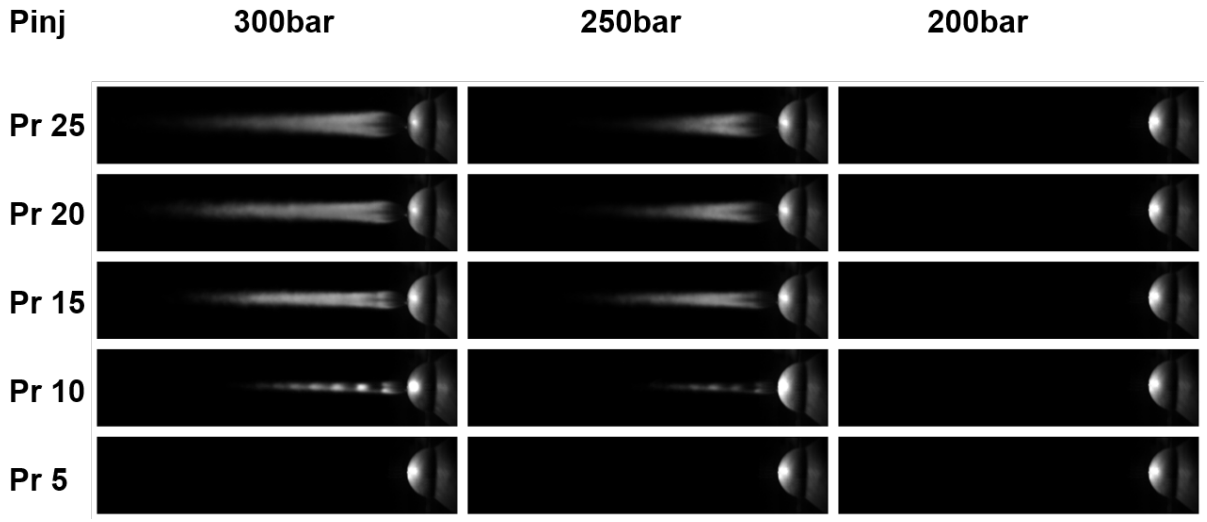

Figure 67: Averaged mie scattering images under variation of injection pressure and pressure ratio at 294 K of injection temperature and 363 K of air temperature.

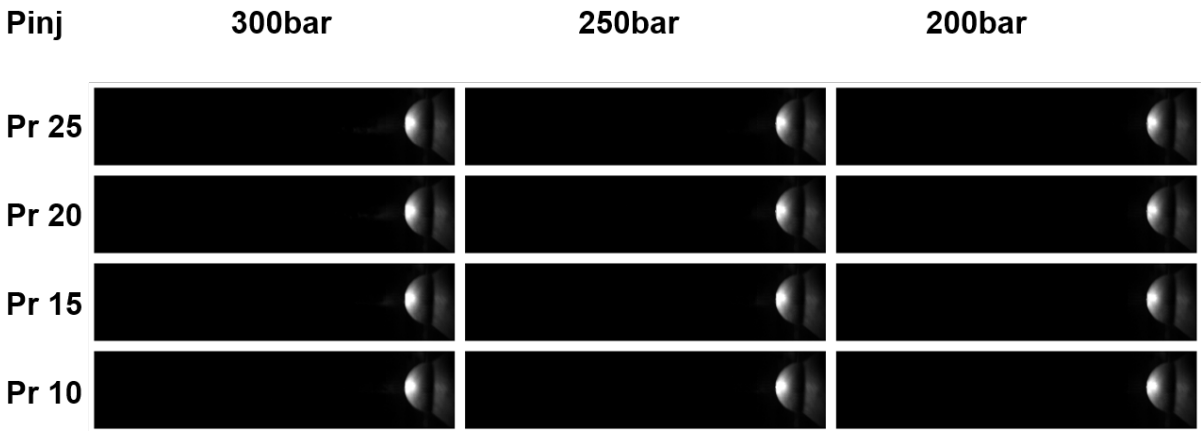

Figure 68: Averaged mie scattering images under variation of injection pressure and pressure ratio at 363 K of injection temperature and 363 K of air temperature.

Figure 66 shows averaged images at different injection pressures and pressure ratios. It can be seen that the higher pressure ratios present a longer liquid core due to the higher injected mass as it needs more time to evaporate, where a similar patter can be seen for the higher pressure ratios in which the liquid is formed to a larger expansion. One attempt to reduce the liquid was to increase the chamber temperature to 363 K, but as shown on Figure 67 it had only a small effect.

From Figure 69 it can be seen that the liquid core grows with the injection pressure up to a certain extent in which it appears to stabilize. On Figure 69 (Left) the injection and chamber temperature have been set to 294 K and it shows the correlation between the injection pressure and pressure ratio, in which the liquid core is larger with higher injection pressure due to the higher amount of injected mass and also grows with the pressure ratio as the expansion is higher. On Figure 69 (right) the injection pressure is set to 300 bar and the ambient temperature is changed. It can be seen that higher chamber temperatures lead to shorter liquid length due to faster evaporation.

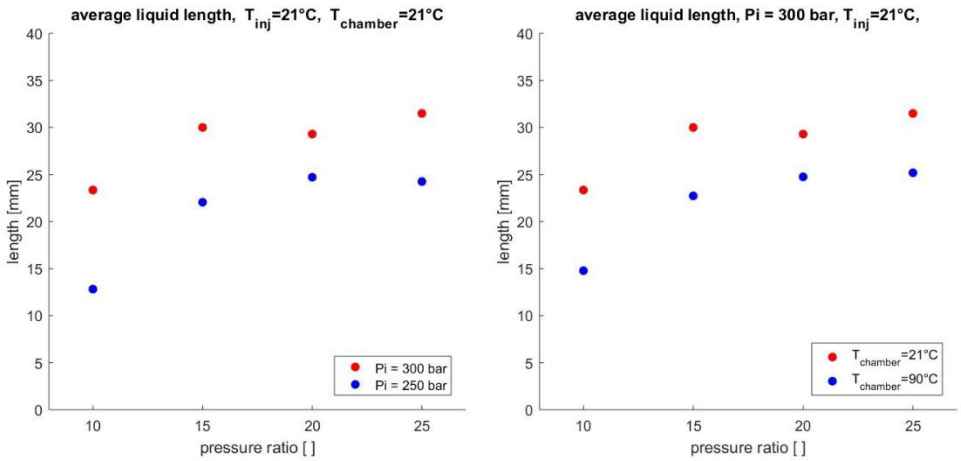

Figure 69: Comparison of stabilized liquid length values at 294 K of injection temperature at 294 K of ambient temperature and 250 bar vs 300 bar of injection pressures (left) and at 294 K of injection temperature at 300 bar of injection pressure and 294 K vs 363 K of injection temperature (right).

Another attempt to eliminate the condensate was to increase the injector temperature to 363 K while keeping the chamber temperature at that same level. On Figure 68 it can be seen that this approach cause the liquid to completely disappear from the combustion chamber, hence setting new temperature levels for the tracer LIF campaign.

3.3.4 Mass fraction distribution

Tracer LIF is applied to experimentally quantify the mixing of injected methane mass and quiescent air inside the CVC. Acetone is chosen as tracer species due to its well-known photo-physical properties, low oxygen quenching rate as well as comparably well characterized properties regarding high pressure environments [39]–[41]. The matrix of operating conditions for this campaign is presented in Table 6. 40 realizations per operating condition have been performed in this campaign.

Figure 70 shows a comparison of the mass fraction distribution at a constant pressure ratio of 5 while increasing the injection pressure from 200-300 bar. It can be observed that the higher injection pressures, which in turn are translated into to a higher injected mass, are leading to richer mixtures while achieving similar tip penetrations at the same instant.

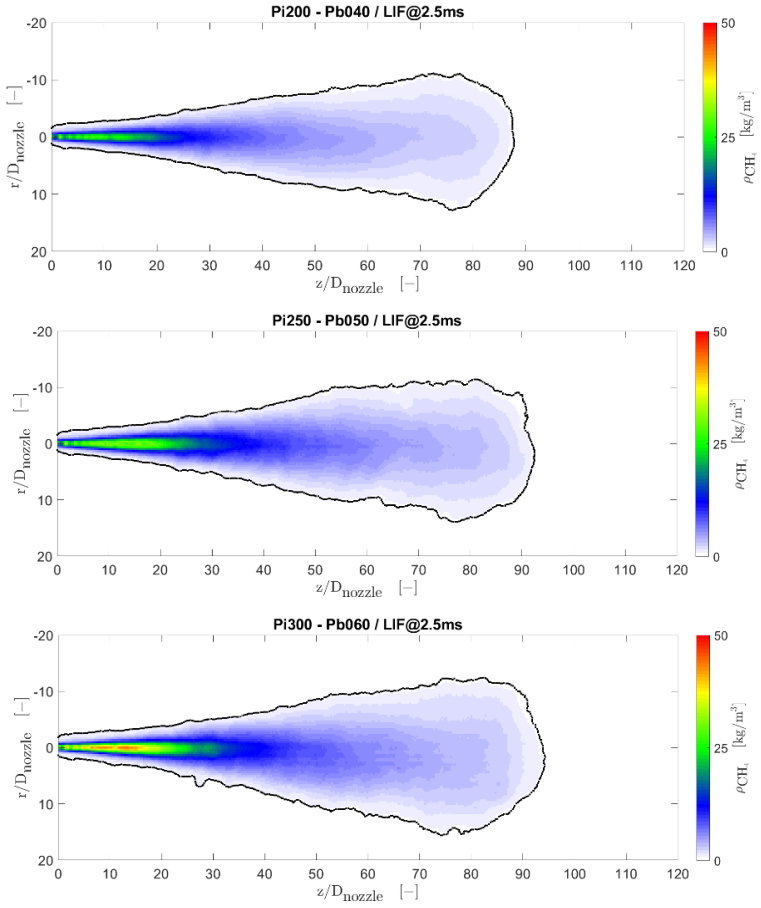

Figure 70: Averaged LIF images taken 2500us aSOE at pressure ratio 5 for injection pressure 200 bar and chamber pressure 40 bar (top), injection pressure 250 bar and chamber pressure 50 bar (middle) and injection pressure 300 bar and chamber pressure 60 bar (bottom).

Figure 71 on the other hand, presents a variation of pressure ratios from 5-8 while keeping the injection pressure at 300 bar. It can be seen that while the pressure ratio is higher and the injected mass is the same it is leading to leaner mixtures caused by the faster penetration of the jet into the chamber, resulting also in longer penetrations.

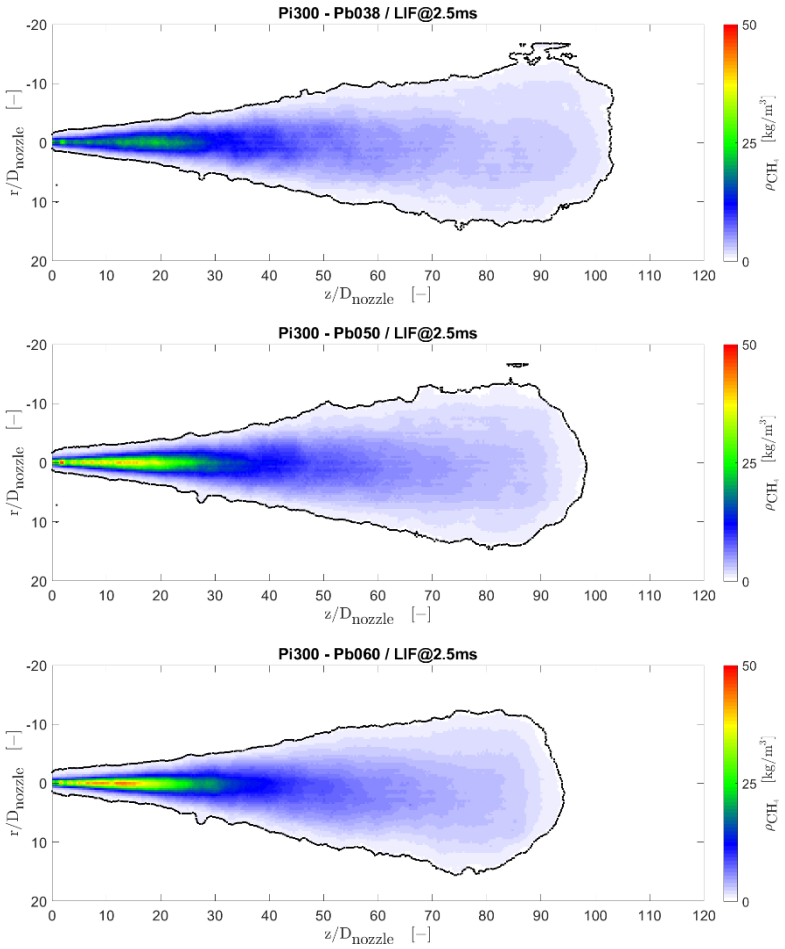

Figure 71: Averaged LIF images taken 2500us aSOE at pressure ratio 5 for injection pressure 300 bar and chamber pressure 38 bar (top), injection pressure 300 bar and chamber pressure 50 bar (middle) and injection pressure 300 bar and chamber pressure 60 bar (bottom).

3.3.5 Auto ignition

For the study of the autoignition a small variation of pressure ratios were studies for the three injection pressure as shown in Table 7. However, for each of the points a variation in temperature was done in order to obtain conditions in which the methane jet would auto ignite within engine relevant times, those temperatures are shown in Table 8.

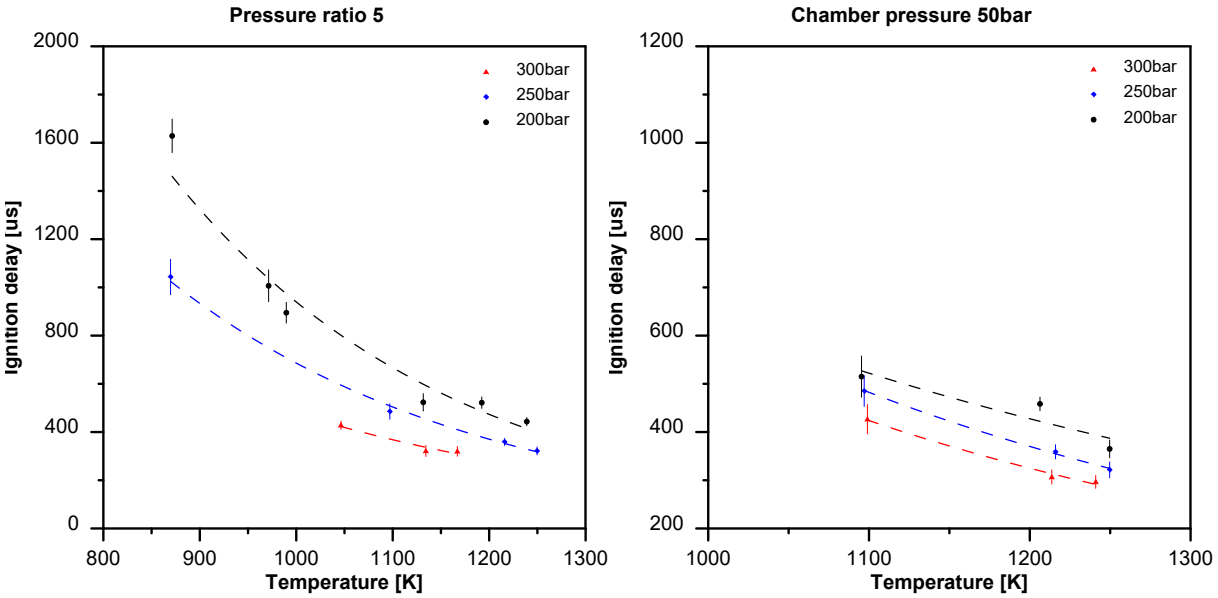

Figure 72: Ignition delay times for injection pressures of 200, 250 and 300 bar under ambient temperatures in the range of 850-125 K at a pressure ratio of 5 (left) and a chamber pressure of 50 bar (right).

Figure 72 (left) shows a variation in ambient temperature (850K-125 K) and injection pressure (200-300 bar) at a constant pressure ratio of 5 and Figure 72 (right) shows a variation in the same injection pressures and ambient temperatures but at a constant ambient pressure of 50 bar. It can be seen that a hotter environment leads to a higher reactivity in the air resulting in shorter ignition delay times, while a higher injection pressure entrains more air because of better mixing, thus leaner mixtures fractions are reached sooner leading to shorter ignition delays.

3.3.6 Ignition strategies

To study the feasibility of igniting a direct-injected high-pressure methane jet in a diesel engine, different ignition strategies were tested. Figure 73 shows the location of the different ignition sources. The pilot injector was located in the center of the combustion chamber with the spray injecting downwards in the same direction of the gas jet, this was done to generate a hot region in the bottom of the combustion chamber. The glow plug was also located in the center of the combustion chamber and generating a local hot spot continuously through the cycle. The pre-chamber was located on the side of the combustion chamber with the nozzle pointing horizontal and therefore the hot jet creates an angle of 90° with the injector axis. For this, a secondary injector was placed inside the pre-chamber to generate a mixture before the injection of the main fuel.

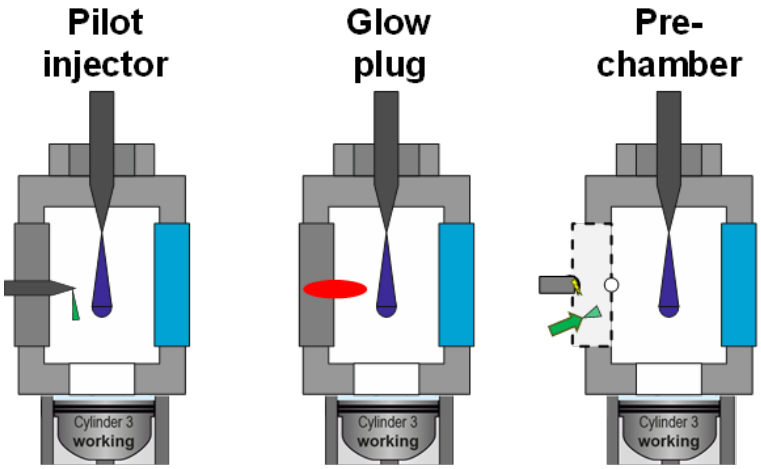

Figure 73: Ignition sources as mounted on the cylinder head. Diesel pilot (left), glow plug (middle) and pre-chamber (right).

Figure 74 presents and ignition sequence of the pilot fuel and subsequent ignition of the main gas jet. The pilot fuel starts being injected from at -8 CAD from the centre of the combustion chamber and it can be seen that it ignites 1CA after in the bottom part of the combustion chamber and the diffusion flame is maintained until -1.5 CAD where injection had stopped. In the meantime, the gas starts being injected at the same time but from the top of the combustion chamber, which allows enough time to mix with the entrained air and reach the bottom of the combustion chamber after the pilot has ignited, thus reaching a hotter zone and igniting at -1CAD. The injection event is much longer than that of the pilot, 3ms vs 0.5ms, therefore the mixing controlled combustion is maintained until 10CA aTDC.

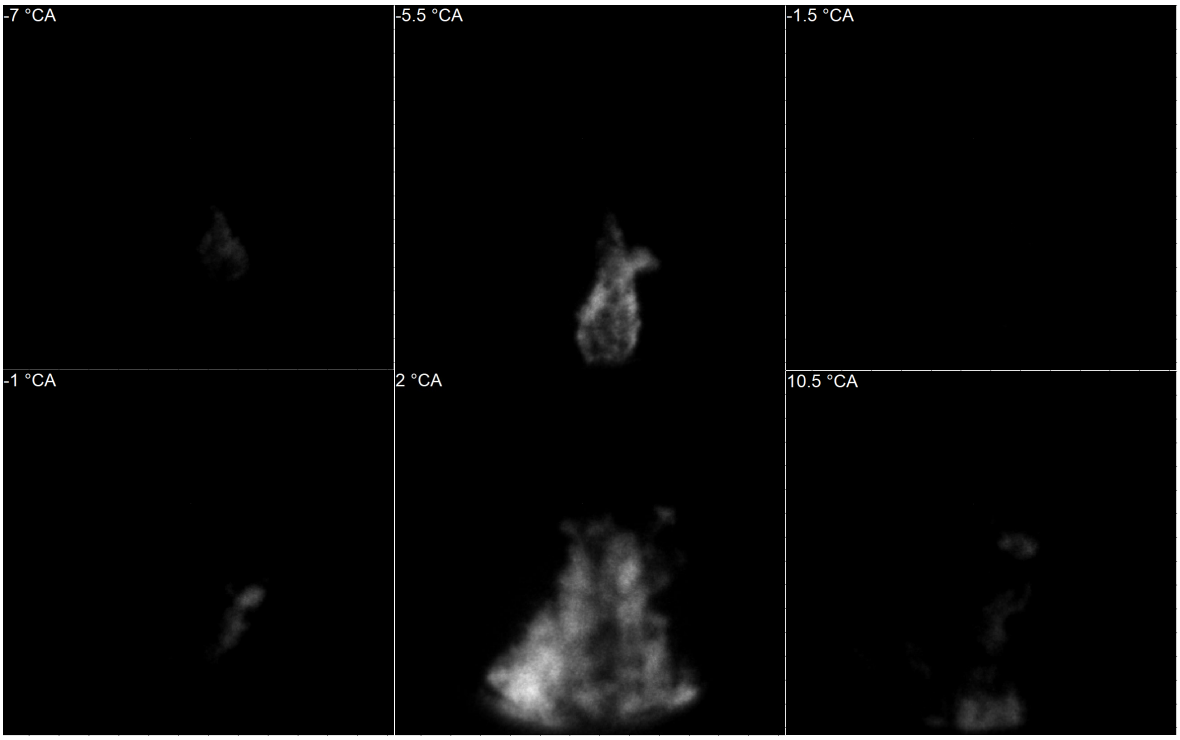

Figure 74: Ignition sequence of diesel pilot extinction of pilot flame and ignition of HP gas jet and combustion.

Figure 75 presents the ignition sequence of the gas jet using the glow plug. With this strategy the jet ignited in the center of the chamber, where the glow plug is located, and slightly earlier than with the diesel pilot. Since the injection duration is also 3ms, the diffusion flame continues until 11CA aTDC.

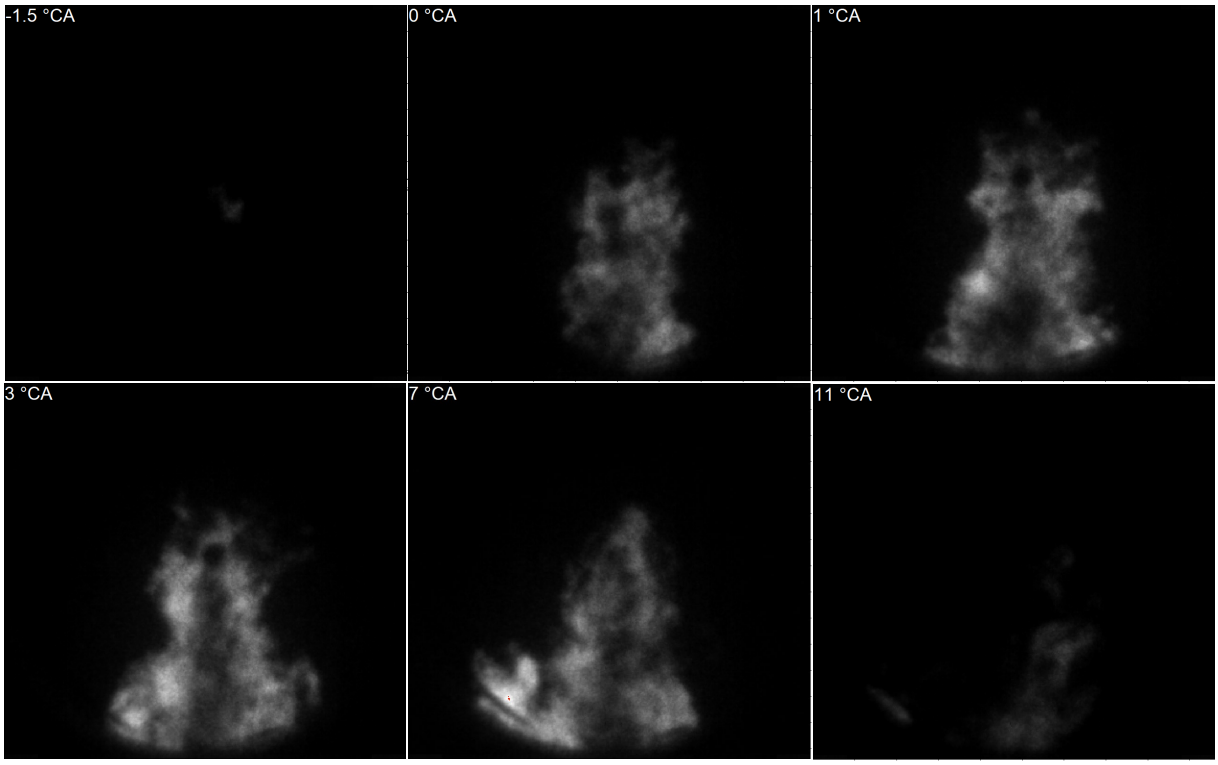

Figure 75: Ignition sequence of HP gas jet at the glow plug location and and combustion.

The ignition sequence of the pre-chamber and subsequent ignition of the main gas jet is shown in Figure 76. In this scenario, a spark plug ignites the mixture inside the pre-chamber, once the flame front reaches the nozzle and comes out the pre-chamber. This results in a reacting hot jet injected into the main chamber that mixes with the fuel being simultaneously injected by the HP gas injector. This results in the jet igniting at -1CA and in the bottom right of the combustion chamber with an increased mixing due to the momentum added by both jets. Accordingly with the pilot and glow plug strategies, the injection duration is the same and therefore the mixing controlled combustion continues until 9CA aTDC.

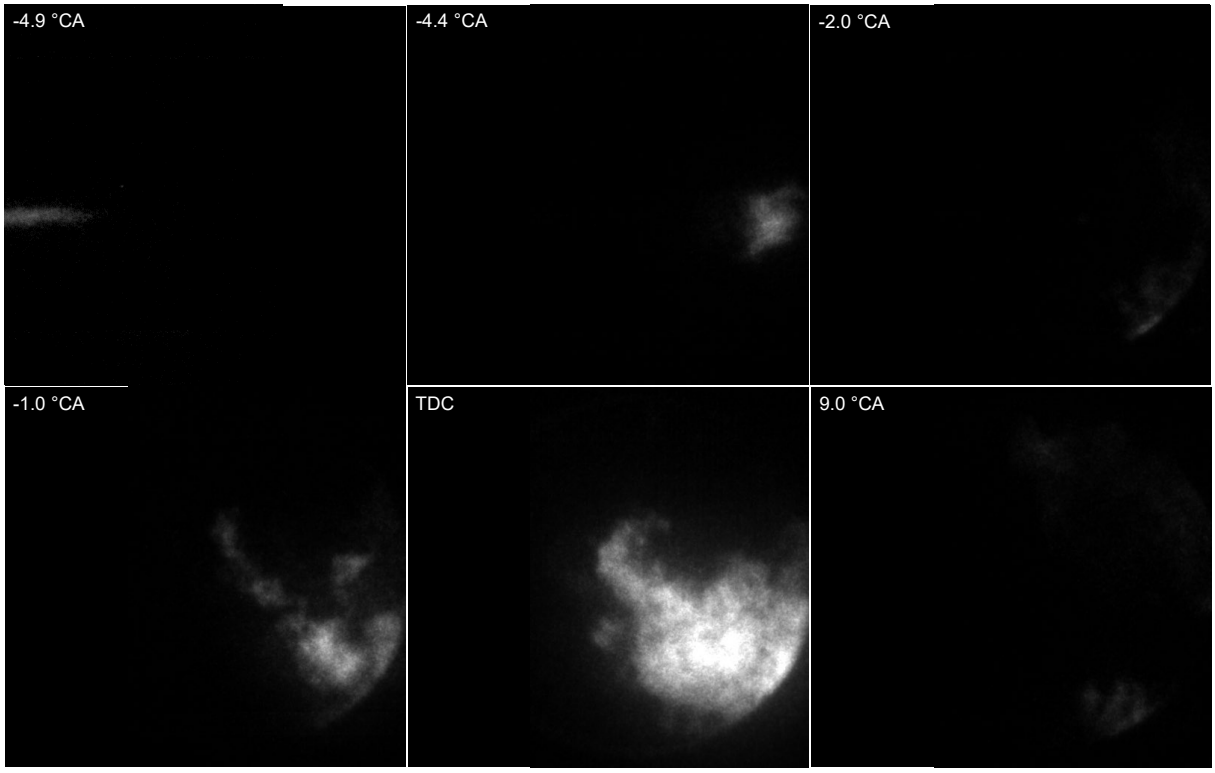

Figure 76: Ignition sequence of PC jet igniting in the main chamber, reignition of the tip of the hot jet, ignition of the HP gas jet at the tip of the hot jet and combustion.

A comparison of the in-cylinder pressure and heat release rate for all three ignition strategies is shown in Figure 77. As previously discussed, the start of ignition is rather similar and the differences can be seen in these plots. The case with the pre-chamber presents the earliest start of combustion, which is caused by the injection of the hot jet from the pre-chamber. The heat release rate and chamber pressure drop slightly during the mixing with the main fuel, only to reignite close to top dead center. The pilot strategy is the second to ignite and the contribution from the pilot can be seen on the heat release rate, but it is not so evident on the pressure trace. Nevertheless, shortly after the gas jet ignites slightly before top dead center. The case with the glow plug is the last to ignite due to the longer time needed to heat up the mixture; however, this results in a high heat release rate due to the premixed combustion. Once the main jet has begun to burn, the ignition source no longer plays a role and the combustion is a process controlled by mixing. This is why the heat release rate curves are rather similar and they all end at the same time.

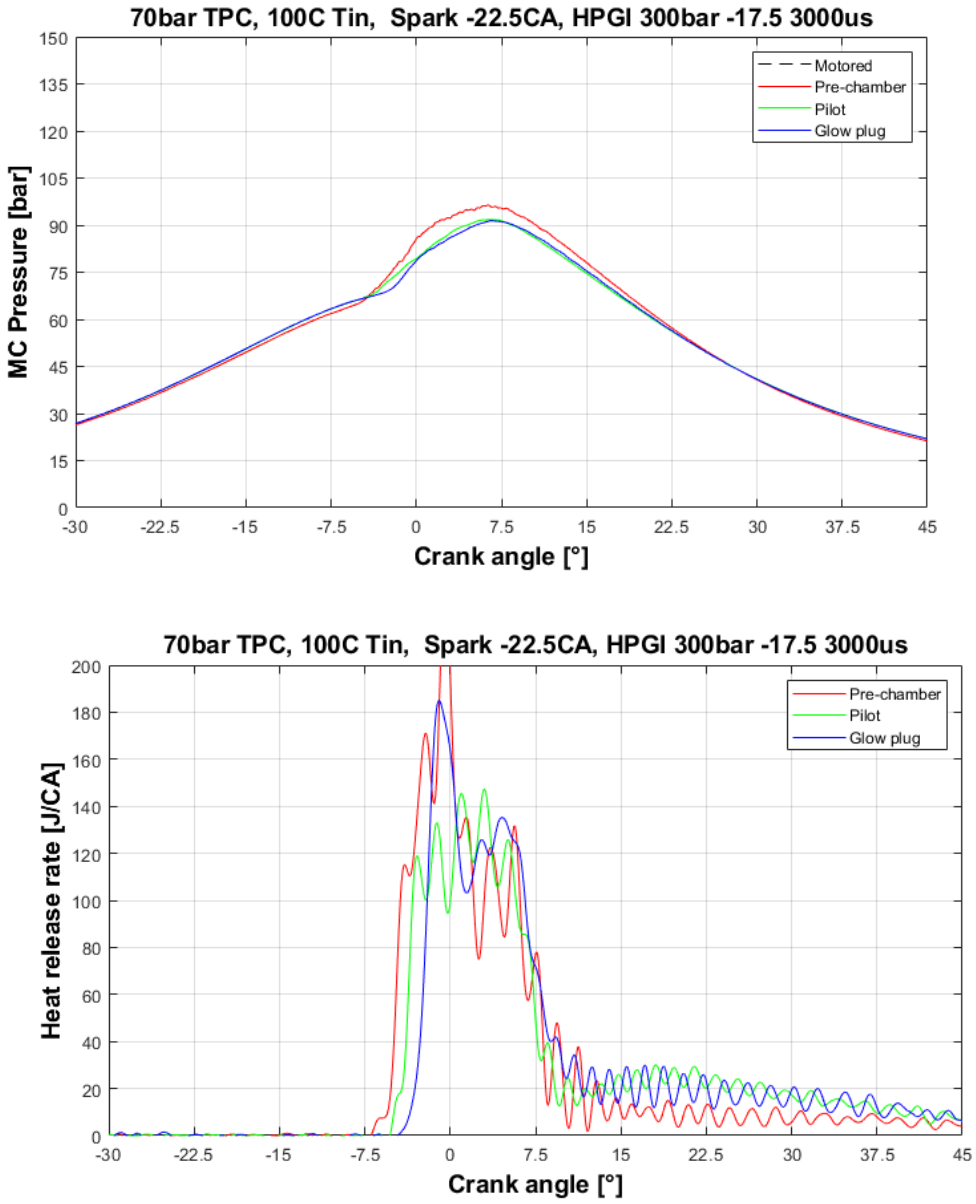

Figure 77: Cylinder pressure (top) and heat release rate (bottom) for all three ignition strategies.

Figure 78 show chemiluminescence images of all three strategies at the same instant, during the mixing controlled combustion. For the case with the pilot, it can be seen that the jet burns in the lower half of the combustion chamber where the temperature is hot enough. This zone is slightly extended with the glow plug, as it is creating a hotter spot in the center of the main chamber and, therefore, extending the burning region. The case of the pre-chamber burns in a similar vertical region as the glow plug as the hot jet is also creating a hotter zone in the center of the chamber, however, the momentum added by it pushes the main jet to the right so the combustion takes place in the bottom-right quarter of the main chamber.

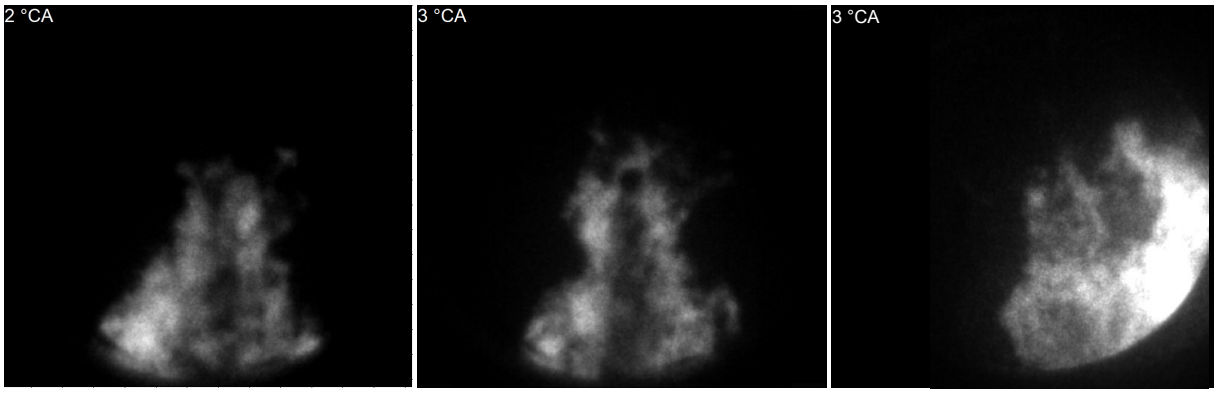

Figure 78: Chemilumincescence images of the HP jet at 3°CA aTDC for pilot (left), glow plug (middle) and pre-chamber (right).

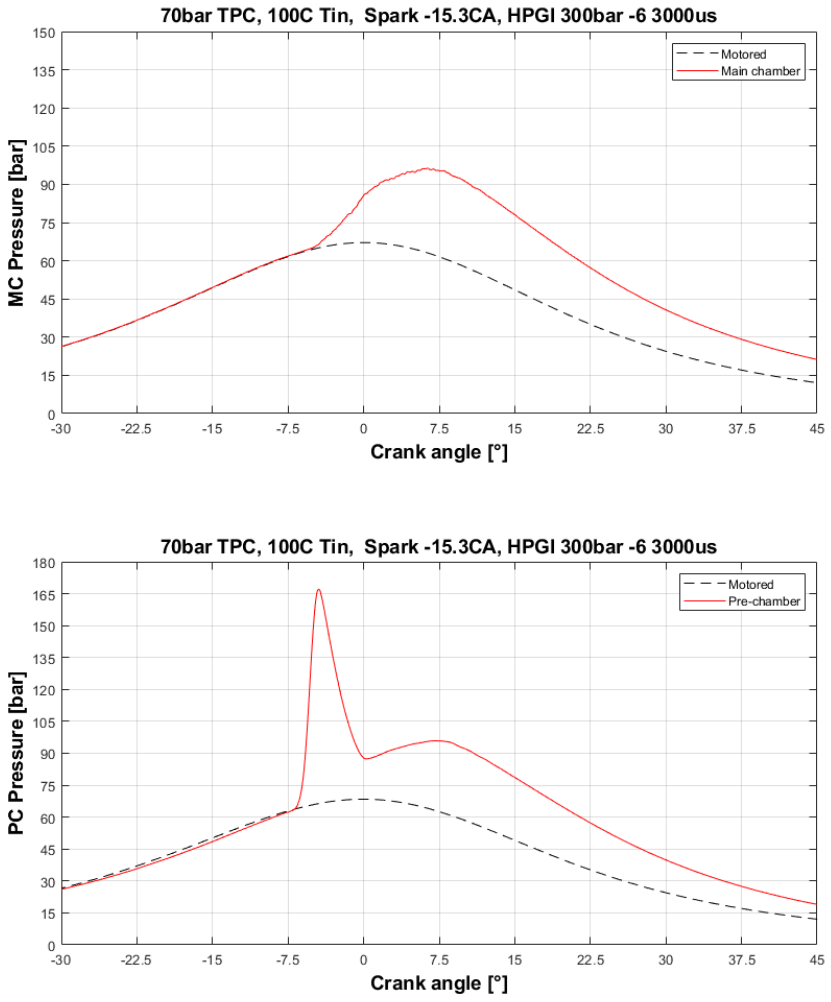

Figure 79: Cylinder pressure traced as measured in the main chamber (top) and in the pre-chamber (bottom) for the reference case.

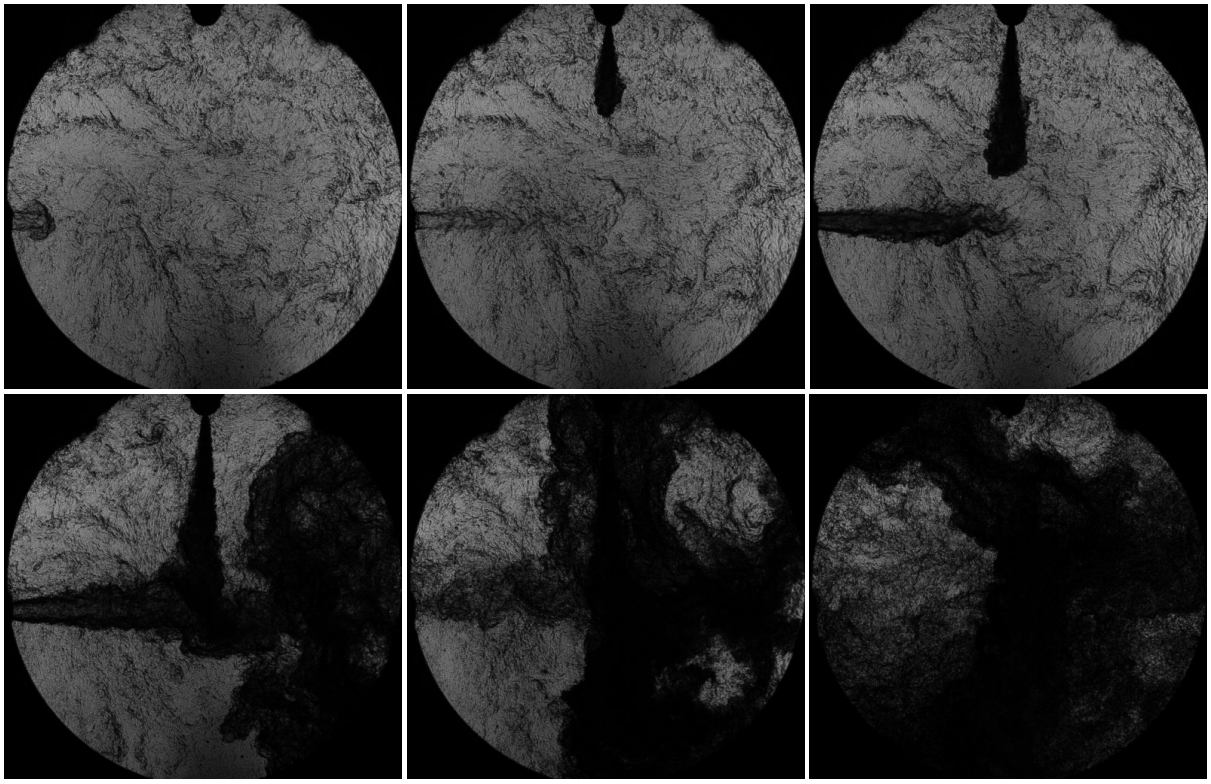

Figure 80: Injection of PC cold and hot jets, mixing with HP methane jet and consequent mixing and ignition.

Finally, Figure 79 and Figure 80 show the pressure traces inside the pre- and main-chamber as well as a sequence of schlieren images with the mixing of the hot and gas jets. The spark is discharged into the pre-chamber at -7.8CA and it can be seen that there is a pressure increase shortly after. Once the pre-chamber pressure starts increases, a cold jet is injected into the pre-chamber, almost at the same time as the start of injection. It is only when the pressure of the pre-chamber reaches its peak that a hot jet is injected into the main chamber, which then encounters the main jet in the center of the combustion chamber. This results in mixing and ignition starting at the lower right of the chamber, as seen Figure 77 and Figure 78.

3.3.7 Ignition and flame propagation in premixed mode: Optical pre-chamber results

In order to visualize the ignition and flame propagation in the pre-chamber as well as the turbulent jet entering the main chamber, and subsequent combustion of the mixture, tests were performed in the optical pre-chamber (OPC) setup described in Section 2.3.4 using schlieren visualization.

The ignition behavior of a standard inductive coil is compared to that of the Nanosecond Repetitively Pulsed Discharge (NRPD) ignition system described in Section 2.1.1. Tests were performed in methane/air mixtures at different air to fuel ratios ($1 < \lambda < 1.8$), at laminar or turbulent conditions, at an initial temperature of 363 K and an initial pressure of 12.4 bar. For the NRPD ignition, different pulse sequences were applied, ranging from 5 to 50 pulses, at a repetition frequency of 10 KHz.

A typical pre-chamber visualization comparing inductive and NRPD (50 pulses at 10 kHz) at laminar and turbulent conditions is shown in Figure 81 and Figure 82 for different times after ignition triggering. The sequence shows the evolution of a very lean case ($\lambda = 1.8$) at 1 ms (Figure 81, left), 2 ms (Figure 81, right), 3 ms (Figure 82, left) and 4 ms (Figure 82, right). Examining the sequence, it can be seen

that at 1 ms (Figure 81, left) a bright spark is visible for NRPD, and a very small initial flame kernel can be recognized in the vicinity of the electrodes, while the inductive ignition displays a fairly more extended flame kernel. A very similar behavior is observed for both laminar and turbulent conditions.

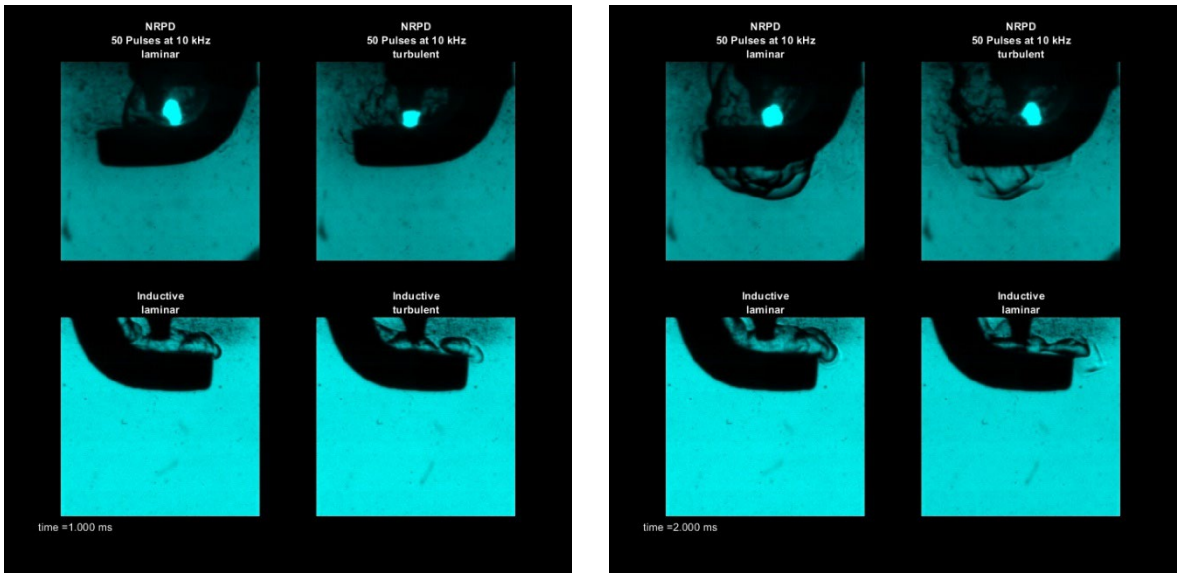

Figure 81: Pre-chamber schlieren visualization of ignition in different conditions. Left: NRPD vs. inductive ignition in laminar and turbulent conditions, 1 ms after ignition triggering. Right: the same test case at 2 ms after ignition triggering.

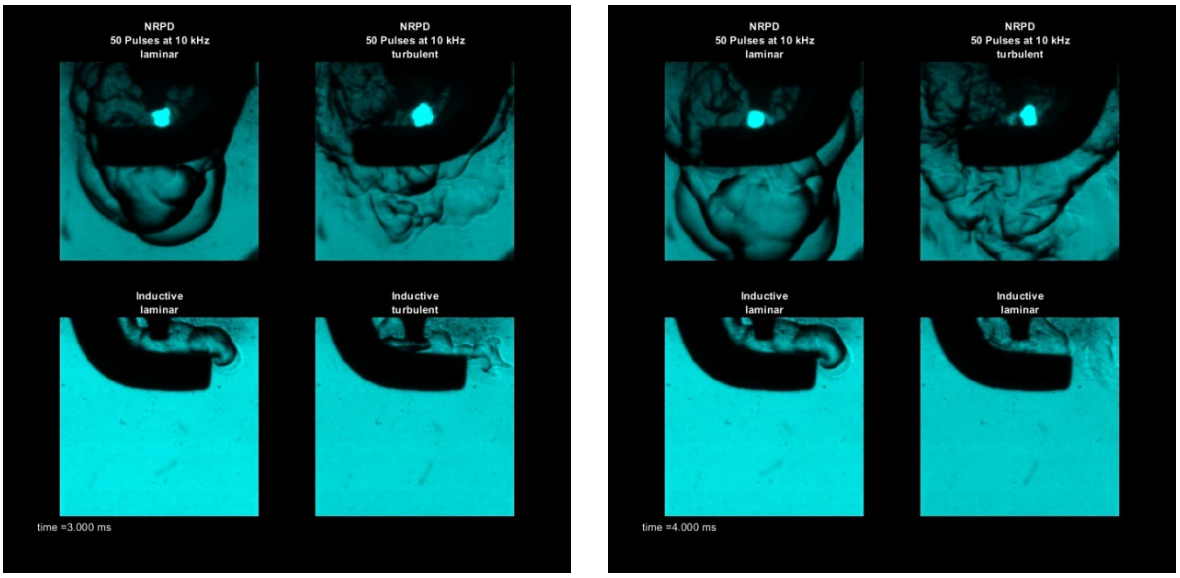

Figure 82: Pre-chamber schlieren visualization of ignition in different conditions. Left: NRPD vs. inductive ignition in laminar and turbulent conditions, 3 ms after ignition triggering. Right: the same test case at 4 ms after ignition triggering.

After this stage, at 2 ms, 3 ms and 4 ms, the NRPD flame kernel quickly develops along the pre-chamber, while the inductive case barely forms a kernel, even in the turbulent condition, and quenches

in the pre-chamber after a few ms (not shown here).The observed behavior is similar for the other cases tested.

In the pre-chamber, a Matlab routine was developed to detect the flame front position. The flame front is chosen as the point on the flame contour that is furthest from the central electrode of the sparkplug. Figure 83 shows the flame front detection at four different time instants (0.4, 0.6, 1.5, and 11 ms) of an experiment in lean condition (λ=1.8) where ten pulses are applied at 12.4 bar and 90°C in laminar condition.

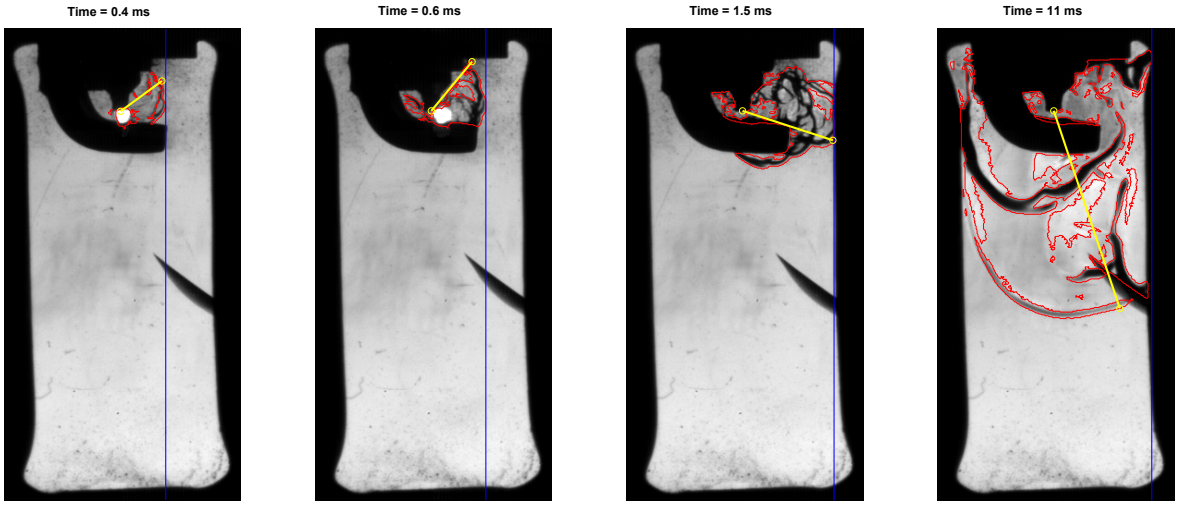

Figure 83: Flame front position measurement

The red surface in figure represents the flame contour detected by the algorithm. For further post-processing, two flame positions are used. The first is the maximal radial distance on the detected contour from the central sparkplug's electrode (the yellow lines). The second is the furthest flame position in the horizontal direction and is represented as blue vertical lines. Figure 84 shows the flame distance as a function of time for different λ values. The experiments are grouped for the different turbulence initial conditions (laminar and turbulent) and different ignition strategies.

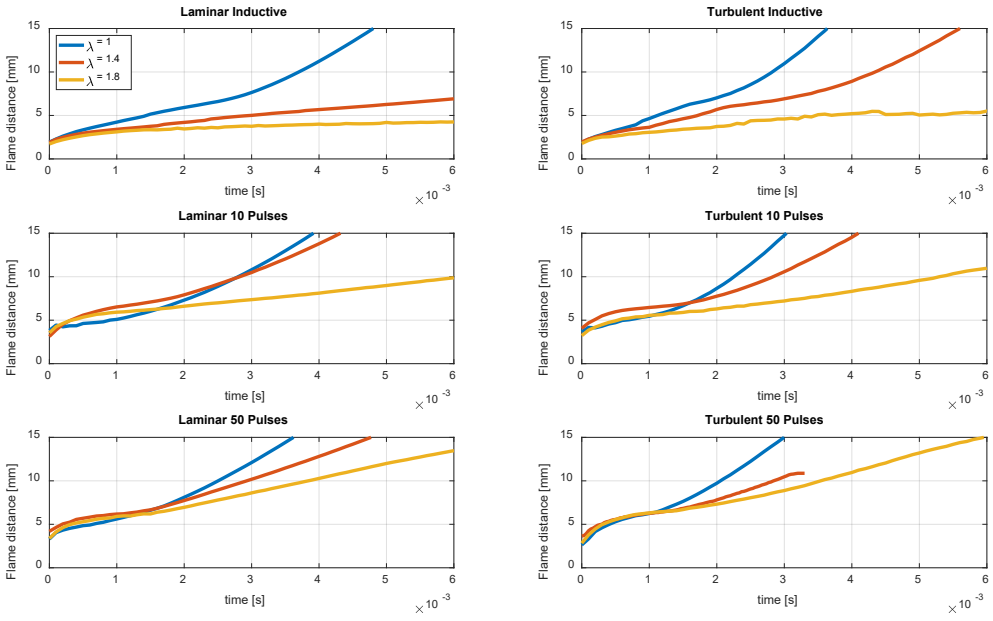

Figure 84: Flame front distance from central sparkplug's electrode lambda variation

For the inductive case (laminar and turbulent conditions), the flame distance starts to vary in dependence of air to fuel ration already after 0.5 ms. For NRPD, the effect on lambdas appears later, at ca. 1.5 ms. Higher pulse numbers reduce the propagation speed loss due to dilution.

Robust ignition in pre-chamber in leaner conditions is obtained when standard inductive ignition is replaced by NRPD [42]. Inductive laminar case shows robust ignition only up to λ =1.5, and has only 30% success rate of ignition at λ =1.8, where NRPD has 75 to 100% ignition success rate. The effect is more prominent in cases where the initial pre-chamber conditions were laminar. The best performance in terms of average flame front propagation speed and ignition success rate are obtained when NRPD is applied with a pulse sequence of 5 to 10 pulses, at 10 kHz pulse repetition rate. Increasing the total energy delivered is not an effective way of improving the ignition success rate, and the role of the competition between the characteristic recirculation time from the discharge-induced flow field and the inter-pulse time is discussed in [42].

When flame front propagation is taken into account, results show that NRPD is advantageous especially in lean conditions, where enhanced local radical concentration at the ignition location plays a major role in terms of inflammation onset. When the energy is supplied in a shorter time interval, higher energy densities and temperature gradients are achieved in the inflammation zone, resulting in NRPD leading to higher peak speed than inductive ignition, and to a higher rate of ignition success at the same operating conditions. The observed advantages of NRPD ignition (higher ignition success rate in lean conditions, increased flame front propagation, advantage of NRPD most prominent in laminar cases) cannot be explained with an increased local turbulence due to repetitive discharge. In fact, the effect of turbulence and mixing due to different dwell times was shown to be independent on the ignition strategy. In order to explain the observed behaviors, and specifically the effect of ignition strategy on early flame development, the mechanism of accumulation due to multiple discharge ignition described in [43], resulting in enhanced local radical concentration at the ignition location, can be taken into account. This mechanism is believed to result in increased peak speed corresponding to the plasma expansion, and ultimately in an increased size of the initial flame kernel [44]. This effect is

more prominent in lean conditions, where a higher energy is needed for ignition onset. After inflammation, additional pulses do not further improve the flame propagation, thus explaining the existence of an optimum number of pulses. The peak speed, the rate of successful ignition and the flame front propagation are all improved when increasing the number of pulses from 1 (inductive ignition) to 10-20, while above this level no further advantage is obtained, because the energy that is supplied after the inflammation occurrence does not contribute to flame propagation. The present findings, compared to available literature results, show that the discussed mechanisms are valid also at high pressure and narrow gaps. This suggests that, also for very lean mixtures and engine-relevant density conditions, ignition can be optimized by tuning the energy per pulse and the number of pulses, the latter becoming relevant only when the delivered energy is close to the inflammation limit.

It is interesting to examine how the observed ignition behavior in the pre-chamber affects the onset of ignition in the main chamber through hot jets [45].

The flame front propagation speed in the pre-chamber increases with increasing number of pulses (Figure 85, left) at the leanest condition (λ = 1.8). This effect is more apparent for laminar initial conditions, but similar observation, albeit with a higher standard deviation, can be drawn from turbulent cases. One might assume that this can be explained with the increased energy deposited in the ignition location, but this is not the case for the richer cases, thus suggesting that the amount of energy alone does not explain the increased flame front propagation speed. In the tested conditions, the inductive ignition delivers 25-50 mJ per ignition event, with a large standard deviation over the tests (±17 mJ), while NRPD ignition delivers 11 ± 1 mJ per pulse. The measured energy delivered for a number of pulses ranging from 1 (inductive) to 50 is similar for the three λ values considered, namely ranging from 25 (inductive) to 467 mJ (50 pulses) for λ = 1.8, from 36 to 456 mJ for λ = 1.4 and from 48 to 453 mJ for λ = 1. Therefore, the amount of delivered energy does not explain the ignition advantage shown by NRPD when compared to inductive systems, and other mechanisms must be considered.

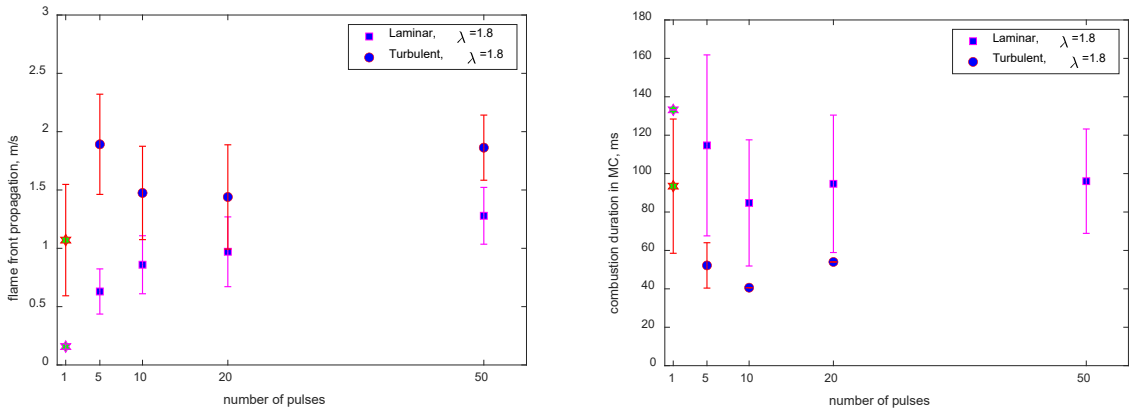

Figure 85: Left: flame front propagation in the pre-chamber vs. number of applied pulses. Right: combustion duration in main chamber vs. number of pulses. NRPD repetition rate 10 kHz, λ = 1.8.

If one considers the combustion duration in the main chamber (Figure 85, right), calculated as the time between 5% and 95% total heat released, it is observed that the combustion duration does not follow the opposite trend as the flame front propagation in the pre-chamber. Namely, the combustion duration is slightly less than 140 ms in the inductive cases, and decreases when NRPD is applied,

reaching a minimum at 10 pulses and then slightly increasing for increasing number of pulses; this pattern can be seen for laminar and turbulent cases. In order to explain this behavior, the mixing in the main chamber has to be considered. Figure 86 shows three typical cases (5, 10 and 50 pulses) and the corresponding ignition sequences are shown in, for the laminar cases. When 5 pulses are delivered (Figure 86, top), the flame front propagation is slow (around 0.6 m/s), resulting in a hot jet entering the main chamber and mixing at a low rate with the colder gases. The result is a slow volume reaction, with low heat release rate and high combustion duration (approximately 115 ms). When 10 pulses are delivered (Figure 86, middle), the jet exiting the pre-chamber is faster (~ 0.8 m/s) and needs a shorter time to mix, leading to earlier ignition in main chamber and faster flame propagation. In this case, the combustion duration in main chamber is lower (~ 90 ms). Finally, when a 50 pulses case is examined (Figure 86, bottom), an even higher flame propagation is reached (~ 1.3 m/s). The higher speeds results in a faster penetration of the hot jets in the main chamber, the jets reach the bottom of the main chamber already at 22.5 ms (50 ms where needed with the 5 pulses case). As a result, the hot jet mixes faster with the rather cold ambient gases, leading to an overall colder mixture. The colder mixture will take longer to ignite and more time to burn (again lower heat release rate and higher combustion duration, around 95 ms). This observation is related to the overmixing phenomenon presented by Vera-Tudela et al. [46]. A similar pattern is seen for the turbulent cases.

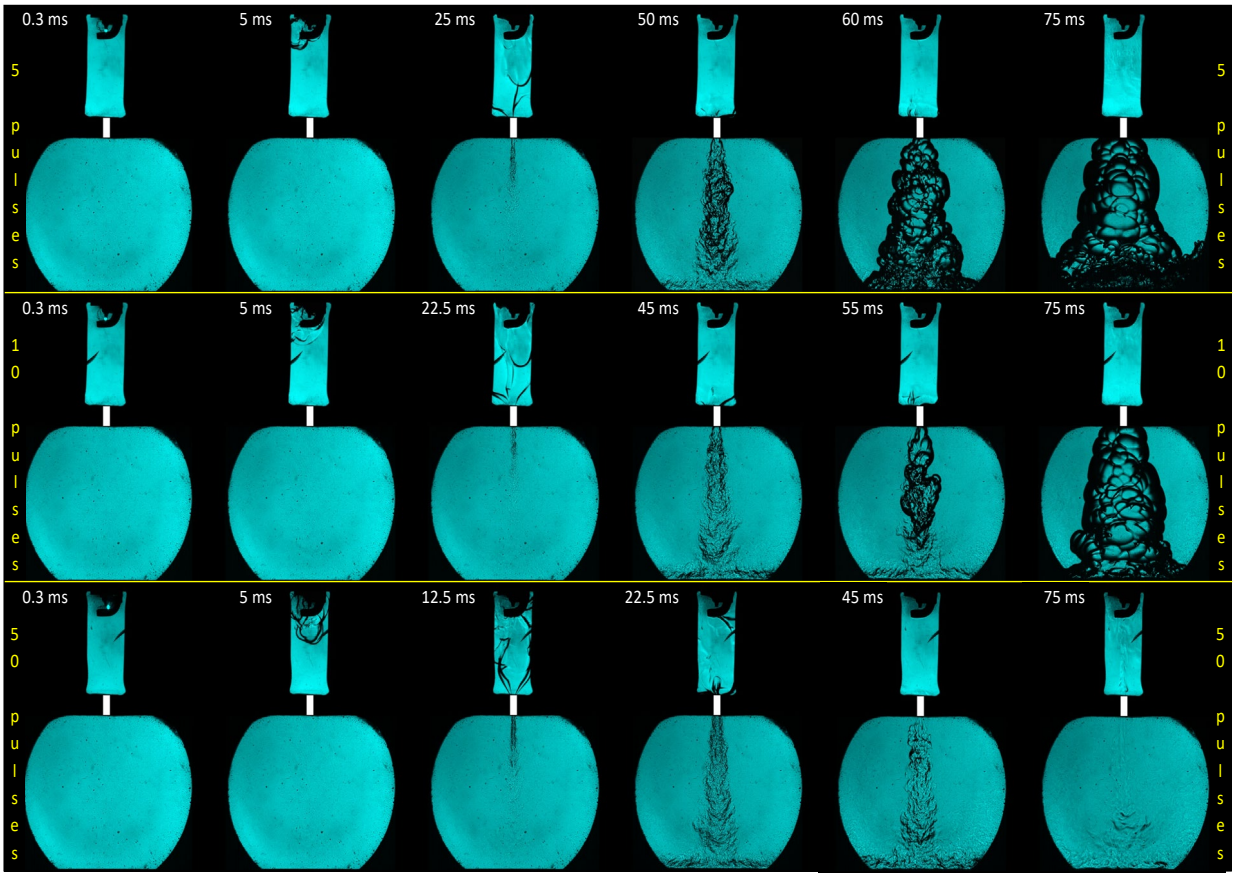

Figure 86: Ignition sequence in the pre-chamber and in the main chamber using the NRPD ignition system with 5, 10 and 50 pulses. 10kHz, 12.4 bar, 90°C, λ = 1.8. Pulse generator: FPG15. Laminar conditions in the pre-chamber.

As a conclusion, the ignition behavior observed in the OPC tests can be summarized as follows [45].

The amount of delivered energy does not explain the ignition advantage shown by NRPD when compared to inductive systems, thus suggesting that the major role in achieving a robust ignition is played by an efficient energy distribution into highly non-equilibrium states. As a consequence, an increased number of pulses only affects the ignition probability at very lean conditions, while 10 pulses are sufficient to ignite all the dilution conditions below λ =1.8.

Examining the heat release rate and the combustion duration in MC, it was shown that there is an optimum range of flame front propagation speed in PC for which the jets entering in the MC ensure adequate mixing with the MC mixture to ensure reliable ignition. Therefore, ignition probability in MC has a maximum in a certain range of flame front propagation in PC, particularly for 10 pulses from the NPRD ignition system. This is related to an overmixing phenomenon, resulting in longer ignition delays and even misfiring. Under the conditions studied, 10 pulses appeared to ignite the MC with the highest reliability.
In laminar PC conditions, a higher pulse repetition rate does not result in higher ignition probability in the MC, even when lower energy-pulses are applied or if the number of pulses is increased. Additionally, it was shown that turbulent PC conditions lead to a reduced ignition probability in MC when compared to laminar PC conditions, for all the pulse number and repetition frequencies investigated. This confirms that, while the NRPD strategy improves the ignition in PC, the role of mixing is then the prevailing effect when TJI comes into play. While NRPD has proved its effectiveness also in a pre-chamber setup, an optimum exists in terms of pulse number and pulse repetition rate that maximizes the probability of jet ignition in MC through optimization of the PC conditions.
The combination of NRPD and pre-chamber concepts proved to be able to ignite extra-lean mixtures under different conditions in a reliable manner. However, just increasing the number of pulses is not the rule of thumb, as it proved to aid ignition in the pre-chamber but led to misfires in the main chamber. Given the potential of combining NRPD and TJI in a pre-chamber and main chamber setup, investigation is ongoing to assess if the benefits can be carried out in a transient environment under engine-like conditions. In particular, while the conditions investigated in the present setup mimic well the engine conditions when considering the density (which corresponds to an engine compression ratio of 10 starting compression at ambient conditions), care has to be taken when the flow field is considered. In a real engine, there is a significant amount of turbulence in the main chamber due to tumble- or swirl motion, therefore resulting in different mixing conditions at the time of jets entering from the pre-chamber. Additionally, the residual gases remaining in the pre-chamber from the previous cycle modify the ignition conditions at a subsequent cycle, thus determining different initial conditions for ignition onset. These different conditions are likely to significantly affect the ignition probability.

The results obtained in the constant volume cell (Section 3.1.1) and in the optical pre-chamber setup (present Section) are therefore used as a guideline for optimizing the tests in the engine setup. An experimental campaign is ongoing in order to assess the effect of NRPD (number of pulses, pulse repetition rate) on the ignition and combustion behavior in the engine in diluted conditions (Section 3.1.2).

3.3.8 Validation of the Numerical Setup – Cold Flow

The schlieren and Tracer LIF optical experiments in the Constant Volume Chamber have been used as benchmark for the cold flow simulations at the corresponding operating conditions. Taken together, they provide a comprehensive set of measurements highlighting both the temporal as well as the spatial evolution of the jets. Figure 87 shows that numerical predictions of jet tip penetration are in

good agreement with experimental throughout the whole injection event, across a variety of pressure ratios and injection pressures.

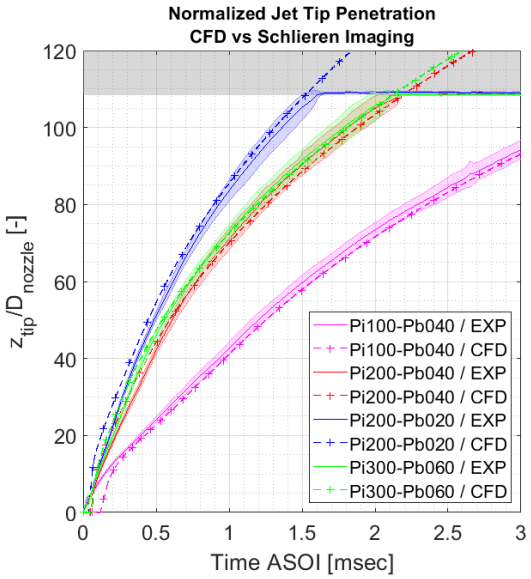

Figure 87: Comparison of normalized jet tip penetration between CFD and Schlieren measurements at selected operating conditions. Both the ensemble-average and the range of ± one standard deviation is shown for the experiments.

The jet tip penetration, after the initial transient phase of needle opening, was found to scale with $z_{tip}(t) = \Gamma\left(\frac{\dot{M}_n}{\rho_{ch}}\right)^{1/4} t^{1/2}$ and the best fit proportionality constant was turned out to be $\Gamma = 3.06$, in line with has been derived in [47] for under-expanded jets. Additionally, approximating jet volume as a cone emanating from the nozzle exit, the volumetric growth of the jets can be predicted as $V_{jet}(t) = K\left(\frac{\dot{M}_n}{\rho_{ch}}\right)^{3/4} t^{3/2}$ with $K = 0.617$, where $\dot{M}_n$ is the momentum flux at the nozzle exit and ρ_{ch} the chamber density.

Figure 88 shows detailed comparisons of radial and axial distributions of partial methane densities between the ensemble-averaged tracer LIF images and the unsteady RANS field for a wide variety of operating conditions. The axial stations are picked to depict the full evolution of the jet. The axial distribution is shown along the jet centerline. The results show very good qualitative and quantitative agreement over the entire plane, with the exception of the near-nozzle area (z ≤ 20D), where the underlying assumptions of the tracer LIF technique are not fully valid due to the large temperature and pressure oscillations caused by the shock diamonds.

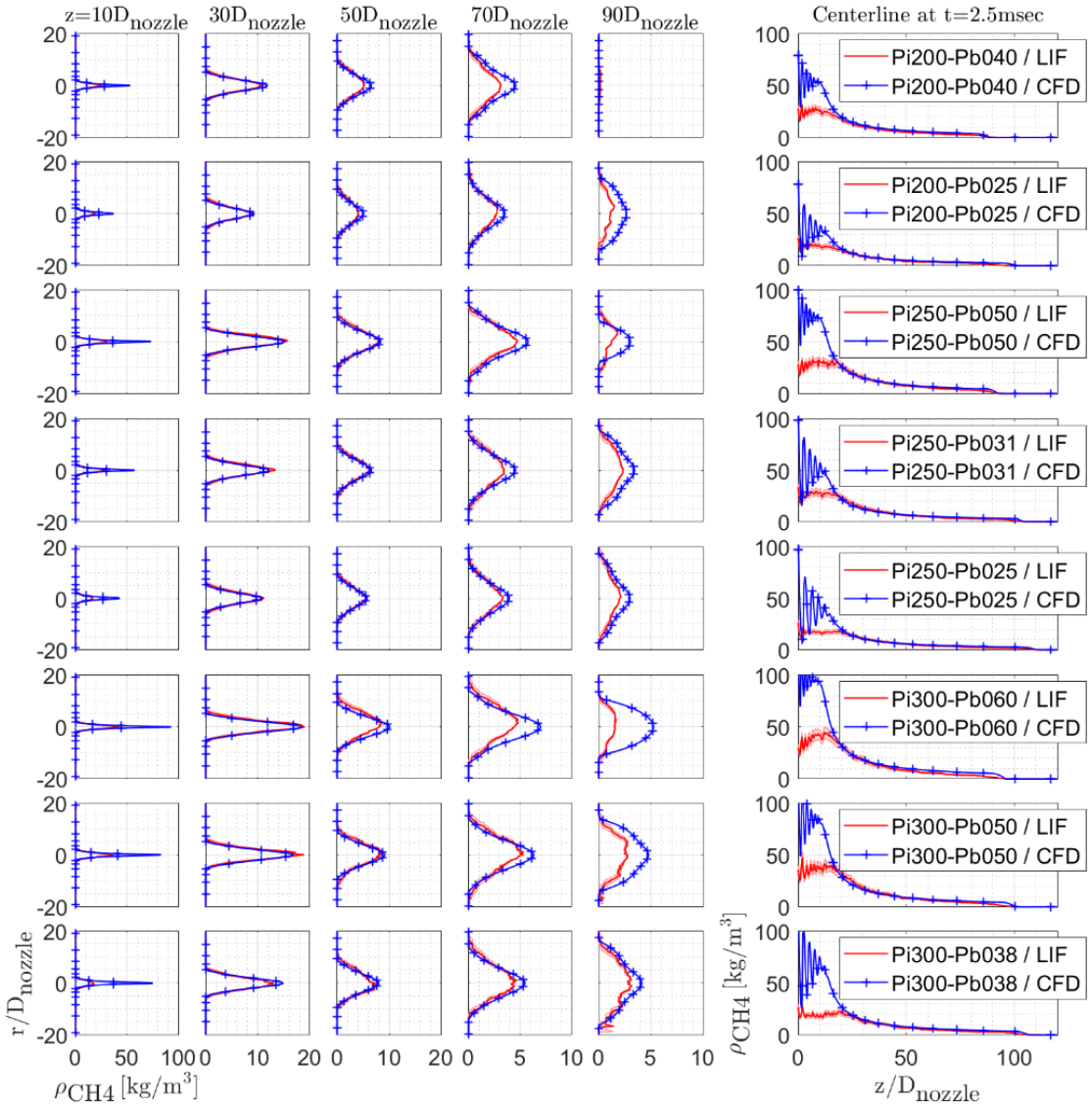

Figure 88: Comparison of radial and axial distributions of partial methane density at 2.5ms after needle actuation between CFD and tracer LIF measurements.

3.3.9 Impact of Injection Strategy on Cold Flow Mixing

The mixing state of the jets is determined by two factors: first, the injected fuel mass, which is governed by the injection conditions, and second, the ambient air mass entrained by the jet, which is governed by its volumetric growth as well as the chamber density and therefore is determined by the interplay of injection and chamber conditions.

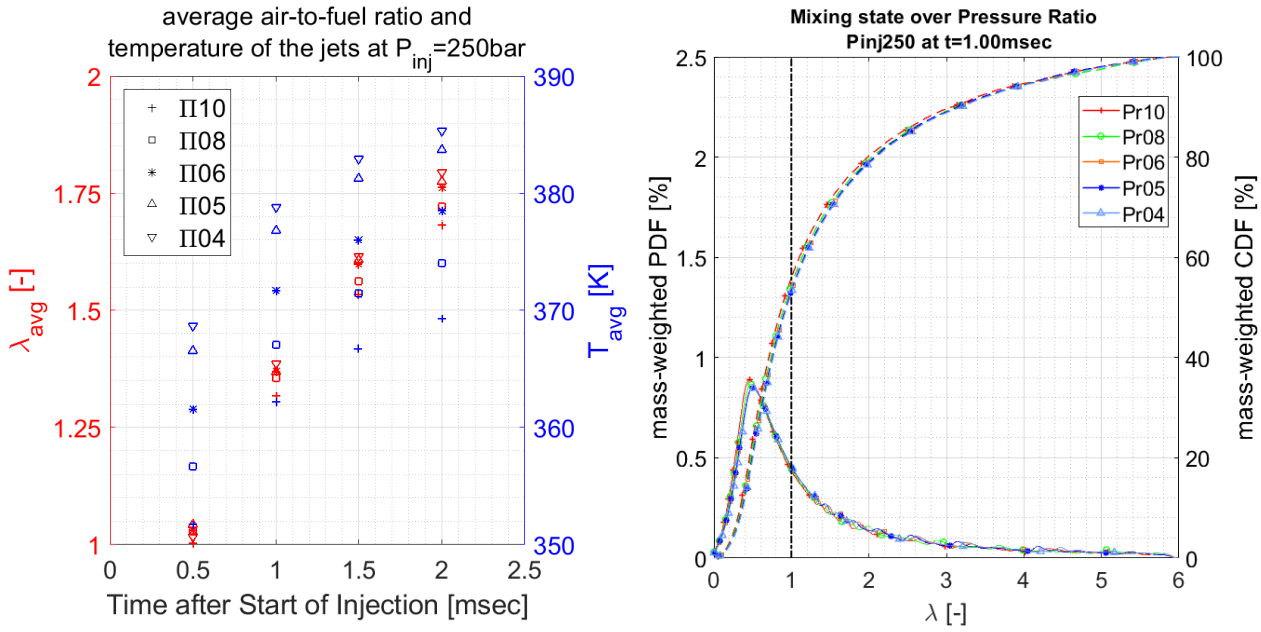

Figure 89: Left: Temporal evolution of the average air-to-fuel ratio and temperature of the jets as a function of pressure ratio, at a fixed injection pressure of 250bar. Right: PDF and CDF of the air-to-fuel ratio of the jets as a function of pressure ratio at the injection pressure of 250bar at 1ms after Start of Injection.

To identify the impact of injection strategy on the mixing state of a jet, one needs to distinguish between two different scenarios:

1. Increasing the pressure ratio, Π, at a fixed injection pressure, P_{inj}, by decreasing the back pressure (i.e. the chamber pressure), P_b.
2. Keeping the pressure ratio, Π, fixed, while increasing the injection pressure, P_{inj}, and the back pressure, P_b.

Figure 78 (left) shows the temporal evolution of the mass-weighted mean air-to-fuel ratio and temperature of jets, at fixed injection pressure and varying chamber pressure. The higher the pressure ratio, the slightly colder and richer the jet becomes on average and, though small, this behaviour can be consistently observed at all time instances and at all injection pressures. Decreasing temperature with increasing pressure ratio can be expected based on the stronger expansion and therefore lower temperatures in the shock cells after the nozzle exit. Decreasing air-to-fuel ratio is brought about by that fact that although the jet volume increases with increasing pressure ratio at a fixed injection pressure, the larger volume of engulfed air is more than offset by its lower density at the lower chamber pressure. This leads to an actual reduction in the entrapped air mass, while the injected fuel

mass remains virtually identical, because the flow is choked and the discharge coefficient remains virtually constant.

Figure 78 (right) shows how the different mean, mass-averaged jet air-to-fuel ratios translate into distributions of local air-to-fuel ratio throughout the jet. At 1ms after injection, the jet has attained the quasi-steady state on all conditions. It can be seen that the Probability Distribution Function (PDF) of local mixing states at the different backpressures is highly similar, the most notable difference being that the larger pressure ratios exhibit slightly higher and richer peaks, which is what ultimately manifests into the slightly less lean global air-to-fuel ratio.

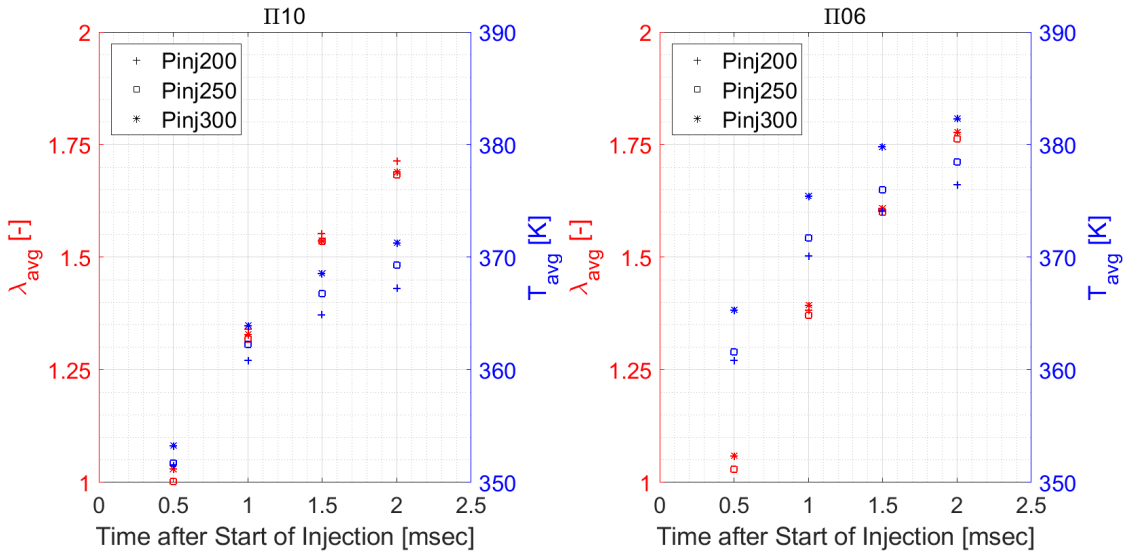

Figure 90: Temporal evolution of the average air-to-fuel ratio and temperature of the jets as a function of injection pressure, at a fixed pressure ratio of $\Pi = 10$ (left) and $\Pi = 6$ (right) at 1ms after Start of Injection.

Figure 79 shows the temporal evolution of mean jet air-to-fuel ratio and temperature at fixed pressure ratios, while varying both injection and backpressure. In this case, the injected fuel mass increases with increasing injection pressure and the entrained ambient air mass increased with chamber pressure, although jet volume remains roughly constant (differences are owed to needle dynamics), because the ambient air density increases. Therefore, the mean jet air-to-fuel ratios are very close to each other at all times for all injection pressures and the very small deviations between them or amongst different pressure ratios reflect random perturbations in the measurements, which are carried over to the CFD boundary conditions.

From an engine operational perspective, it can be concluded that:

1. The mixing state at auto-ignition is essentially determined by τ_{ign}, not Π
2. Increasing the pressure ratio at fixed injection pressure beyond the critical pressure ratio, i.e. the pressure ratio at which the flow becomes choked, by decreasing the chamber pressure does not lead to better mixing. By contrast, it creates slightly richer/less lean on average jets, because the larger jet volume is more than offset by the lower density of the engulfed ambient air. The local air-to-fuel ratio distribution in these jets is very similar, meaning that more mixing sites with conditions favorable to auto-ignition or conditions more favorable to auto-ignition are not created in this way. Moreover, this strategy might prove counter-productive, as increasing the pressure ratio risks causing condensation, wall impingement and cools down the jet due to stronger expansion.

3. Applying the same pressure ratio at different injection and chamber pressure levels (which are varied in a consistent manner, so that the pressure ratio remains fixed) leads to identical global air-to-fuel ratio as well as local distribution of air-to-fuel ratios in the jets. This implies that the pressure levels should be chosen based on the following considerations:
    a. The desired injection mass flow rate, which increases with injection pressure
    b. The desired chamber reactivity, which is partly determined by the chamber pressure
4. Overalll, higher injection pressure is generally desirable, since it allows for applying supercritical pressure ratios at higher chamber pressures, thereby promoting auto-ignition and leading also to a shorter combustion duration.

3.3.10 Impact of Injection Strategy on Auto-Ignition

The auto-ignition delay of turbulent methane jets at different injection strategies can be examined numerically from the standpoint of the interplay between reactivity, represented by a global reaction rate of the form $r_{\mathrm{global}} = k_{\mathrm{global}}[F]^a[Ox]^b$, where the reaction rate constant is expected to have an Arrhenius type of temperature dependence, $k_{\mathrm{global}} = AT^{\beta}\exp(-{E_A}/{RT})$ and jet aerodynamics, represented by jet tip penetration. The scaling has been already explored in Section 3.3.8. In this context, four different variations in parametric space were designed, as shown in Figure 91, which account for changes in the primary control parameters of the injection strategy: injection pressure and temperature, chamber pressure and chamber temperature.

On the left column of Figure 91, it is first verified that the temperature-driven reactivity variation at fixed jet aerodynamics has an exponential impact on the auto-ignition delay. However, auto-ignition delay in the fully turbulent flow-field is prolonged by the requirement for appropriate mixture formation and also the effects of diffusion, stretch and turbulent transport (comparison between CFD/CMC and homogenous reactors). Furthermore, it is verified that the pressure-driven reactivity variation at fixed aerodynamics is has a power-law impact on the auto-ignition delay through the concentration of the reactants (fuel and oxidizer) in the chamber.

On the top right subplot of Figure 91, the effect of jet aerodynamics on auto-ignition delay at constant reactivity is explored. Although not grounded in analytical considerations, it is found that there is a weak linear dependence with pressure ratio, which accelerates auto-ignition delay at higher injection pressures and therefore faster jets. Lastly, in conjunction with the power-law dependence on pressure-driven reactivity, this linear dependence on jet propagation speed can predict changes in chamber pressure at fixed injection pressure very accurately, as shown in the bottom right subplot of Figure 91.

Combining the insight from these four parametric variations, a single functional form for auto-ignition delay in the turbulent flow-field can be constructed $\tau_{\mathrm{ign}}(\mathrm{T_{ch}}, \mathrm{P_{ch}}, \mathrm{P_{inj}}) = \left[\mathrm{D1P_{ch}^{D2}} - \mathrm{C2}\frac{\mathrm{P_{inj}}}{\mathrm{P_{ch}}}\right]\mathrm{e}^{1000\mathrm{B2}/\mathrm{T_{ch}}}$.

Finally, this expression can be expanded to include injection temperature as a control variable, by considering the stoichiometric mixture temperature (at frozen mixing conditions) as the characteristic temperature of the system:

$$\tau_{\mathrm{ign}}(\mathrm{T_{ch}}, \mathrm{T_{inj}}, \mathrm{P_{ch}}, \mathrm{P_{inj}}) = (\mathrm{C_1} - \mathrm{C_2}\Pi)\mathrm{e}^{\frac{\mathrm{E_A}}{\mathrm{RT_{st}}}}\mathrm{P_{ch}^{-n}} - \mathrm{C_3}\Pi + \mathrm{C_4}\Pi^2$$

The four coefficients have been obtained by a least-squares error minimization process, resulting in the following values: C_1=0.001480; C_2=6.85*10^{-6}; C_3=0.027809 and C_4=0.001407. E_A/R=10210 [K], n=0.56. The temperature at stoichiometry T_{st} is obtained as a function of T_{ch}, T_{inj}, P_{ch}, P_{inj} from

adiabatic mixing between the oxidiser side (chamber conditions) and the fuel side. For the latter, an isentropic expansion from the injection conditions to chamber pressure is followed as in the Adiabatic Expansion Approach for under-expanded jets [47], to obtain the “equivalent jet” temperature.

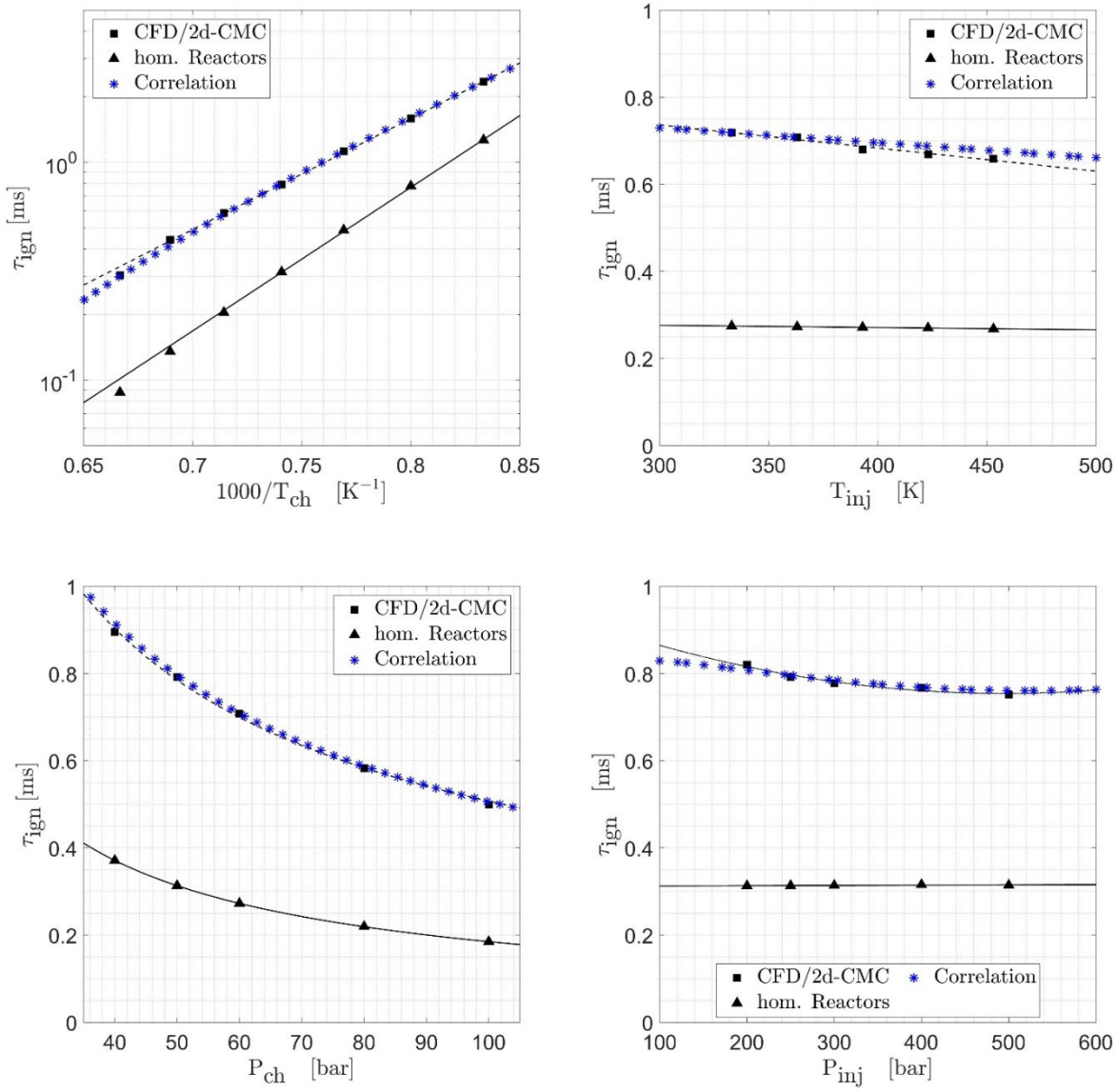

Figure 91: CFD predictions of auto-ignition delay of methane jets as (top-left) a function of chamber temperature, T_{ch} at fixed injection pressure of $P_{inj} = 250$ and $P_{ch} = 50$bar (bottom-left), a function of chamber pressure, P_{ch} and injection pressure, P_{inj} at fixed pressure ratio of $\Pi = 5$ and chamber temperature $T_{ch} = 1350$K (top-right), a function of pressure ratio Π and injection pressure P_{inj} at a fixed chamber pressure of $P_{ch} = 50$bar and chamber temperature $T_{ch} = 1350$K (bottom-right) and as function of pressure ratio Π and chamber pressure P_{ch} at a fixed injection pressure of $P_{inj} = 500$bar and chamber temperature $T_{ch} = 1350$K.

This correlation has finally been assessed using data from the literature, namely measurements from the works of Fraser et al. [48], Naber et al. [48] and Sullivan et al. [48] will be considered. Fraser et al. [48] carried out measurements of ignition delays of underexpanded jets in a CVC with a view to exploring practical ignitability limits in terms of cell temperature and pressure for various CH_4/C_2H_6 blends. They also used a pre-combustion system, albeit with H_2/C_2H_4, for achieving temperatures and

pressures high enough to enable jet auto-ignition, but their CVC additionally featured a fan used to maintain spatially temperature uniform temperature throughout the CVC before fuel injection, limiting non-uniformity to 4% in its core. Naber et al. [48] carried out similar measurements in a CVC with a H_2/C_2H_2 pre-combustion system and a fan to restrict temperature non-uniformity to 2% in the CVC's core. Finally, Sullivan et al. [48] used a shock tube to generate a uniform ambient environment of heated up and pressurized air, into which their natural gas jets were then injected. The aforementioned measurements have been carried out at different injection conditions than which upon the correlation was constructed and with different experimental apparatuses, including different injectors with different designs, nozzle diameters and mass flow rates, which inevitably introduce discrepancies between the measurements themselves, as will be seen further below. However, they do eliminate the main uncertainty associated with the question of temperature homogeneity in the OH* chemiluminescence measurements and, based on the analysis so far, deviations in CVC temperature are expected to have a much more profound effect than any other factor.

The operating points selected from these are restricted to pure CH_4 jets, because variations in chemical composition cannot be captured by the developed correlation, to super-critical pressure ratios, and to vessel temperatures between 1100 K to 1600 K, as the very strong sensitivity of reactivity to temperature, renders the reliability of predictions much beyond the calibration limits dubious. On a related note, data points with P_{ch} between 20 bar to 40 bar have been accepted, and, while P_{inj} in the experiments of Sullivan et al. lies well below the lower limit of the range targeted in this work, their measurements have also been included, partly because the sensitivity is not expected to be as strong in these cases, but mostly because of the relative scarcity of available experimental data, as to the authors' best knowledge, beyond these studies only the work of Ishiyama et al. [49] exists, no data can be drawn from which due to different chemical composition of their natural gas jets.

The comparison of the predictions by the correlation with the independent measurements are shown in Figure 92. In Figure 92a, there is a good match with the general experimental trends over T_{ch} at all P_{ch} levels. Due to the large scatter, the effect of P_{ch}, into which the effect of Π is additionally subsumed, is not easily distinguishable in the measurements. In Figure 92b, the trends at different ρ_{ch} levels are qualitatively well described. By keeping ρ_{ch} and P_{inj} fixed, all T_{ch}, Pch and Π are varied simultaneously. Still, the interlocked effect of P_{ch} and Π is now more clearly identifiable by comparing different ρ_{ch} levels at the same T_{ch}, it is well reproduced. However, a certain consistent underprediction of ignition delays is observed, except at the highest ρ_{ch}. At very high temperatures (over 1450 K), this might be partly owed to the different physical delays associated with the finite rate of injection, which limits the minimally traceable pressure rise in the experiments. In contrast to Figure 92b, in Figure 92c ignition delays are more strongly over predicted at the lower temperature range, but the agreement improves at intermediate temperature levels (over 1350 K). In the context of medium-to-large ICEs, where HPDI of NG is of most interest, deviations of 1 ms, which are the largest observed in Figure 92, might translate into 6° crank angle, and deviations of around 0.2ms, which are typical, into 1.2° CA, assuming a rotational speed of 1,000 RPM.

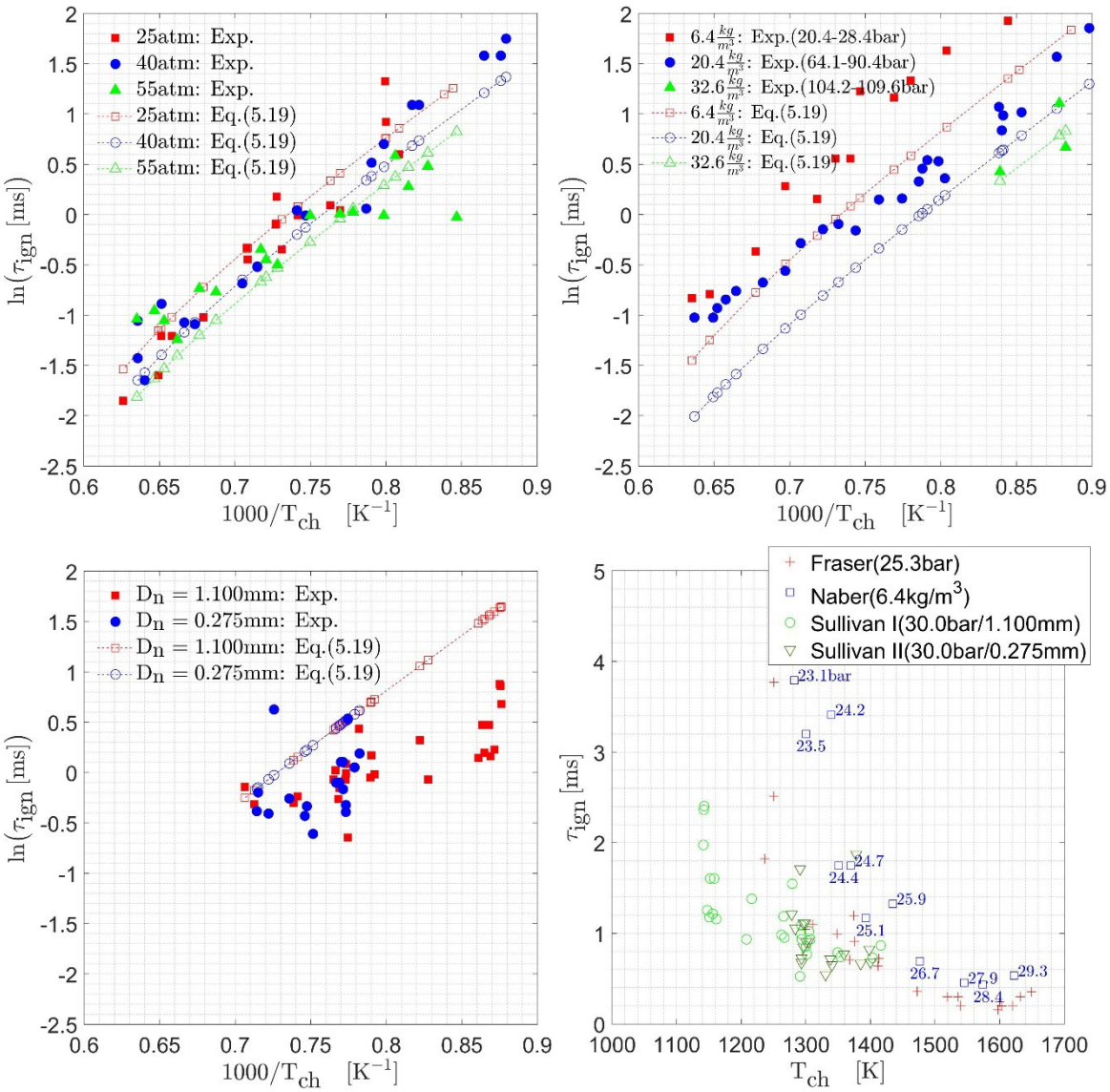

Figure 92: Predictions by the developed correlation compared to the CFD/CMC results: (a) as a function of T_{inj} at constant P_{ch} = 60bar, T_{ch} = 1350 K and P_{inj} = 300 bar, and to the experiments of: (b) Fraser et al. [48] at P_{inj} = 206:7bar, T_{inj} = 444 K, Dn = 0:57mm (c) Naber et al. [48] at P_{inj} = 207bar, T_{inj} = 450 K, Dn = 0:25mm (d) Sullivan et al. [48] at P_{inj} = 75bar, T_{inj} = 300K and P_{ch} = 30bar. In (c) the equation coefficients have been calibrated for identically defined ignition delays (P_{ch} = 14 kPa). (d) Comparison of experimental measurements from different groups at closest operating conditions.

It is likely that the CFD/CMC calculations are less accurate at conditions of low reactivity. This has previously occurred in simulations of diesel sprays by Bolla et al. [49] as well as simulations for methane jets by Sayed and Devaud [49]. The results of the latter showed strong sensitivity to the choice of the kinetic scheme (much improvement was recorded with UBC 1.0 [50] compared to GRI 3.0) and to a lesser extent to the scalar dissipation rate model (AMC better than Girimaji's [49]). Imperfections in the description of the kinetic rates become more pronounced at low reactivity conditions due to the exponential or power dependence and then are compounded by TCI. However, this cannot explain the general tendency of the developed correlation to overshoot the measurements of Sullivan et al. while undershooting the measurements of Naber et al. Juxtaposing measurements carried out at approximately the same T_{ch} span at the closest

available P_{ch} level, the following picture emerges, as can be seen in Figure 92d: the longest ignition delays have been measured by Naber et al. at ρ_{ch} = 6.4 kg/m^3 (translating into pressures ranging between 23.1 bar to 29.3 bar), the shortest ignition delays have been measured by Sullivan et al. at 30 bar (notably, despite their T_{inj} being lower by roughly 140 K than in the other two works), whereas the measurements of Fraser et al. at 25.3 bar lie somewhere in between. Some deviations are to be expected, given that different test rigs and instruments, different measures of ignition delay and different ambient chemical compositions were employed in these works, in addition to uncertainties in the measurements. The effect of different orifice diameters is another thing to consider, but a literature survey yields contradictory conclusions and the work from Sullivan et al. shows minor differences even when a four times larger D_n is used. Another important reason for the deviations could be the use of injectors with substantial disparity in mass flow rates, beyond what is attributable to the different diameters. This implies differences in injector performance and, as demonstrated earlier, injector dynamics can have a strong effect on ignition delay. This likely accounts for some differences between the developed correlation and the experiments as well. For example, the L'Orange injector modeled here needs 0.13 ms to inject 0.33 mg at 200 bar and 363 K, whereas the injector used by Naber et al. needed 0.33 ms at 207 bar and 450 K for the same amount of natural gas. In light of all the uncertainties, the reasonably good agreement with two out of three experimental works and the acceptable accuracy for practical purposes is deemed satisfactory.

4 Conclusions

The overall project could be performed as planned and the project was able to deliver manifold results in the respective fields. Beside of senior researchers, PhD students and master students were involved in a wide variety of topics. Many project results could be published in highly reputable scientific journals by all involved research groups.

In WP1 (Electrical Ignition Methods), the ignition cell setup has been modified and a NRPD system has been integrated. Spectroscopic methods have been established to correctly trigger and gate the measurements, which was a challenging task as the individual pulses are very short (in the order of 50 ns) and timing jitter had to be minimized using sophisticated triggering techniques. The spectroscopic footprints of a NRPD ignition have been recorded and they happen to be, as expected, very different to the spectroscopic footprints of classical inductive or capacitive ignition systems. For accurate control of NRPD ignition in a 4-cylinder running engine, a deeper understanding of the active electrical circuit and of the factors affecting the breakdown was needed. Therefore, an investigation was carried out to characterize the influence of pulse rise rate and pulse duration on ignition attempts.

Experiments on a four-cylinder engine with a high- and low-pressure EGR using a classical inductive ignition system have successfully been performed as the benchmark for the engine experiments using NRPD ignition. The engine test bench was adapted for NRPD ignition with a 4-channels pulse generator. The ignition was investigated at a fixed operating point of 1500 rpm, and 100 Nm with different sparkplugs geometries and pulse repetition frequencies. NRPD allows reliable ignition of very lean mixtures (λ above 2) or high EGR rates (35%). Higher pulse repetition frequency results in higher combustion stability (advanced ignition timing), and faster inflammation. Tests are still ongoing to optimize NRPD ignition. New sparkplug geometries and locations will be tested, and the application of NRPD ignition in a prechamber.

Regarding the air-path control (WP2), a toolchain has been developed, which allows the generation of fast and precise air path controllers for various internal combustion engines of different size and air path configuration. A particular focus was placed on the generation of intelligent control structures that track intake gas conditions in an engine efficiency- or emission-optimized manner. The chosen approach is based on nonlinear model predictive control and a library of models of air path components that can be arranged to represent different air path configurations. The models can be identified with a low amount of measurement data and the NMPC algorithm consists of only few tuning parameters that can be mostly defined in simulation. In order to implement the controllers on an embedded platform, the open-source software “acados” is used. Together with the university of Freiburg, Germany, the functionalities of this software have been considerably extended in order to fit the requirements of the control structure developed. These extended functionalities are now part of the “acados” software package and available to everyone.

The effectiveness of the developed toolchain has been experimentally validated on two laboratory engines. For a turbocharged light-duty engine with two EGR paths, a pumping-loss minimal air path controller is developed, which effectively tracks the intake gas pressure and oxygen concentration under consideration of pumping losses, which reduce the engine efficiency. For a turbocharged heavy-duty engine with high-pressure EGR and an exhaust flap, the developed toolchain is used to derive a controller that outperforms a linear control approach, which is specifically designed and tuned for the chosen engine operation point.

Some algorithms derived within the REAL project are used in a lecture for master students at ETH Zurich. Students learn to design their own nonlinear model predictive controller and have the chance to test and tune it at an engine test bench.

The experimental part performed in WP3 presented a thorough analysis of a high-pressure methane jet under steady, transient and reactive conditions. To accomplish this, different campaigns were performed while applying various optical techniques. An investigation was carried out to study the effects of the injection parameters on the needle lift. The needle dynamics showed to have a strong dependency on the injection and control pressure, especially at lower injection pressures. These effects were attributed primary to the injection pressure, but also to the control pressure. Another campaign was performed to corroborate the trends seen in the literature with the current setup, under conditions where the effects of the needle dynamics can be safely neglected. The parameter which affect the jet penetration is mainly the pressure ratio. Experiments under transient conditions also followed the previously observed trends, although the increasing back pressure led to a continuously decreasing pressure ratio which affected the behaviour of the jet.

A NRPD setup has been realized on the optical pre-chamber which was equipped with schlieren technique as well as with spectroscopy. The tests show that the NRPD ignition is able to establish a much more robust flame kernel compared to inductive ignition systems. An in-depth analysis of the results was performed and three publications were prepared summarizing the findings, which guide the planned NRPD engine tests. The early flame front propagation was examined and the influence of the observed ignition behavior in the pre-chamber on the onset of ignition in the main chamber through hot jets was investigated. Examining the heat release rate and the combustion duration in main chamber, it was shown that there is an optimum range of flame front propagation speed in pre-chamber for which the jets entering in the main chamber ensure adequate mixing to ensure reliable ignition. The results, useful for guiding the engine tests design in WP1, were summarized in two journal publications and in a conference contribution.

Simulations performed by the Universität der Bundeswehr München (within the accompanying FVV Project) suggested that liquid methane may form in the near nozzle region at low injection temperatures and high pressure ratios. Therefore an experimental campaign applying Mie-scattering was carried out, confirming the numerical observations. Higher injection pressures and higher pressure ratios cases presented the most liquid. Although increasing the ambient temperature reduced the liquid length, condensation was still present under most conditions; however, increasing the injection temperature completely eliminated the liquid methane from the jet meaning that condensation should not be an issue under engine conditions.

A tracer LIF campaign was performed to validate the models developed and the mass fraction distribution within the jet was characterized under the most relevant operating conditions. Higher mixtures fractions were found closer to the nozzle at higher injection pressures and lower pressure ratios, the former caused by the higher injected mass and the later by the wider jet angle.

Finally, a reactive campaign was carried out to study the feasibility of methane auto ignition in a hot environment under engine relevant conditions.

The conclusions drawn from this investigation are as follows:

- Keeping the pressure ratio constant while increasing the injection pressure would result in the needle opening faster but had no effect on the jet tip penetration. This is because the injection pressure affects the needle dynamics, causing it to open at different rates and then affecting the start of injection and the shape of the tip penetration curve. However, for the cases where the effects on needle dynamics are negligible, there was virtually no difference on the penetration curves at different injection pressures. On the other hand, increasing the injection pressure while keeping the pressure ratio constant would lead to a higher amount of condensate due to the larger injected mass of methane. Although the liquid was eliminated by increasing the ambient and injection temperature, a higher injected mass would also lead to

overall richer mixtures in the jet. Last, higher injection pressures would lead to shorter ignition delay times as the air would be entrained faster and the premixed phase of the combustion would take place sooner.

- Keeping the injection pressure constant while increasing the pressure ratio had no effect on the needle opening but would result in a faster penetration of the jet tip. The effects of the pressure ratio are consistent with the literature, where a higher pressure ratio while cause the exit velocity to be higher and the jet to penetrate faster through the chamber. This would also lead to a larger amount of condensate within the jet due to a larger expansion, such effect was also eliminated by increasing the fuel temperature.

Three-dimensional Computation Fluid Dynamic (CFD) tools were developed and it was found, that accounting for real gas effects is indispensable towards accurate predictions of spray penetration, mixing and temperature distributions. Validation of the mixing and temperature fields by means of the experimental data showed excellent agreement for wide ranges of operating conditions. Combining the experimental and numerical insights, scaling laws were subsequently developed which can be employed for engine design. Simulations of auto-igniting under-expanded jets have been performed using the in-house Conditional Moment Closure combustion model. Operating conditions were specifically varied to design matrices that enabled the development of a correlation for the auto-ignition delay as a function of all injection parameters. This correlation was subsequently assessed by means of experimental data from literature for two campaigns in a Constant Volume Combustion chamber as well as data acquired in a shock tube. Good agreement is reported for the former two while fair agreement is observed for the trends of the latter.

5 Outlook and next steps

The development of internal combustion engines for alternative low-ractivity-fuels has gained on importance over the course of this project. Especially the on- and off-road long-haul sectors have increasingly started to develop alternatives to classical diesel technologies. Additionally, the role of combined heat and power technologies is being discussed due to an increasing decentralization in the power sector and foreseeable challenges regarding seasonal imbalance of production and demand. Therefore, gaseous fuels have come more in the focus, especially methane and hydrogen.

Many results from this project can help for these new technologies. Some can be implemented in the short term (for example the model predictive EGR control strategies which were developed in this project), some need further research before implementation (for example nanosend repetitively pulsed ignition or diffusion-controlled combustion of low-reactivity fuels).

The research groups have identified research needs and initiated follow-up project on several aspects of technologies for alternative fuels. For example in the fields of

- low-temperature combustion (IDSC in the FOR2401 framework[2]),
- fuel-flexible engine technology (Empa and IDSC in cooperation with two industrial partners),
- fundamentals of hydrogen direct injection and diffusion controlled combustion (Empa in cooperation with the University of Stuttgart),
- ignition methods for non-premixed combustion of high-pressure direct injected gas in heavy-duty engines (Empa in cooperation with the University of applied Science North Western Switzerland FHNW and with the Karlsruhe Institute of Technology KIT).

As the pure consideration of efficient engine technologies is an important but not the only aspect for future-proof approaches, Empa is performing R&D in the field of renewable methane production technologies, methane-pyrolsis-based pathways for negative greenhouse gas emissions, energy system modeling and real-time logistics planning.

6 National and international cooperation

WP1 (Empa): The Volkswagen Group Research provided engine hardware and technical support. Empa had exchange in the field of NRPD ignition with the Argonne National Laboratory (Lemont, Illinois), with Kistler (Winterthur) in the field of optical spark plugs, with FPT Motorenforschung (Arbon) and has started a cooperation with a globally active manufacturer of large engines in the field of ignition.

WP2 (IDSC): Within the project FOR2401 which is supported by the “Deutsche Forschungsgemeinschaft”, ETH IDSC collaborated with the RWTH Aachen university, the university of Freiburg and further project partners in order to develop optimization-based combustion control algorithms for low temperature combustion. Synergies arise for many aspects of the control development, especially for the optimization formulation. The FOR2401 project coordinator, employed at ETH IDSC for two years supervised the control algorithm design for the REAL air-path control.

[2] https://www.for-2401.de/

WP3 (LAV): Work package 3 was co-funded by the German Research Association Combustion Enginges FVV e.V. and an associated working group consisting of the majority of the German automotive and heavy-duty industry. Work was carried out in collaboration with the Armed Forces University Munich (UniBW, Prof. Pfitzner) and the high pressure gas injector as well as the pressure amplifier (Maximator) were provided by Woodward l'Orange. Experiments in the optical engine (FlexOeCoS) were carried out in collaboration with the group of Prof. Kai Herrmann at the University of applied Science North Western Switzerland (FHNW).

7 Publications

Here, we list all scientific publications that were performed within the framework of this project.

2022 (including submitted/accepted publications)

- L. Merotto, M. Balmelli, W. Vera-Tudela and P. Soltic, "Comparison of ignition and early flame propagation in methane/air mixtures using nanosecond repetitively pulsed discharge and inductive ignition in a pre-chamber setup under engine relevant conditions", Comb. And Flame, vol. 237, 111851, 2022.
- M. Balmelli, L. Merotto, and P. Soltic, “Plasma to Early Flame Kernel Transition under Nanosecond Repetitively Pulsed Discharge in an Optical Accessible Pre-chamber,” in 5th International Conference on Ignition Systems for Gasoline Engines, Berlin 13th-14th September 2022, 2022.
- M. Balmelli, Y. Lu, R. Färber, L. Merotto, P. Soltic, D. Bleiner, J. Biela, C. Franck, “Breakdown of synthetic air under nanosecond pulsed voltages in quasi-uniform electric fields“, IEEE Access (accepted for publication)
- S. Hänggi, J. Frey, S. van Dooren, M. Diehl, C. H. Onder, “A Generic Approach for Engine Air Path Control Based on Nonlinear MPC”, IEEE Transactions on Control Systems Technology (under review)

2021

- W. Vera-Tudela, L. Merotto, M. Balmelli, and P. Soltic, "Experimental study of the ignition of lean methane/air mixtures using inductive and NRPD ignition systems in the pre-chamber und turbulent jet ignition in the main chamber", Energy Conversion and Management, 115012, 2021.
- M. Balmelli, R. Färber, L. Merotto, P. Soltic, D. Bleiner, C.M. Franck, & J. Biela, "Experimental Analysis of Breakdown with Nanosecond Pulses for Spark-Ignition Engines". IEEE Access, 9, 100050-100062, 2021.
- T. Albin, “Nonlinear Model Predictive Control of Combustion Engines”, Springer International Publishing, 2021
- D. Sakellarakis, Y.M. Wright, W. Vera-Tudela and K. Boulouchos , “Numerical investigation of the autoignition of underexpanded methane jets”, FUEL 291, 2021.
- D. Sakellarakis, W. Vera-Tudela, U. Doll, D. Ebi, Y.M. Wright, K. Boulouchos , “The effect of high-pressure injection variations on the mixing state of underexpanded methane jets”, International Journal of Engine Research 22(9), 2021.

2020

- Vera-Tudela, W., Sakellarakis, D., Wright, Y.M., Boulouchos, K., Banholzer, M. /Pfitzner, M.: Final report FVV project 1236 "Gas-Diesel Combustion", 2020
- M. Keller, D. Ritter, L. Schmitt, S. Hänggi, C. Onder, D. Abel, T. Albin, “Teaching Nonlinear Model Predictive Control with MATLAB/Simulink and an Internal Combustion Engine Test Bench”, IFAC World Chinese Control Conference, 2020

2019

- L. Merotto, T. Kammermann, and P. Soltic, “Ignition Diagnostics in EGR and Air-Diluted Methane/Air Mixtures using Spark Induced Breakdown Spectroscopy”, Combustion Science and Technology, 2019, pp. 1-16.

- T. Kammermann, L. Merotto, P. Soltic, and D. Bleiner, “Spark-Induced Breakdown Spectroscopy for Fuel-Air Equivalence Ratio Measurements at Engine-Relevant Conditions”, Spectrochimica Acta Part B: Atomic Spectroscopy, 155 (2019), 79-89.
- M. Banholzer, W. Vera-Tudela, C. Traxinger, M. Pfitzner, Y. Wright, K. Boulouchos , “Numerical Investigation of the flow Characteristics of Underexpanded Methane Jets”, Physics of Fluids, Vol 31, 056105, 2019.
- W. Vera-Tudela, P. Kyrtatos, B. Schneider, K. Boulouchos, M. Willmann, “An experimental study on the effects of needle dynamics on the penetration of a high-pressure methane jet”, Fuel, Vol 253, pp. 79-89, 2019.

2018

- T. Kammermann, W. Kreutner, M. Trottmann, L. Merotto, P. Soltic, D. Bleiner, “Spark-induced breakdown spectroscopy of methane/air and hydrogen-enriched methane/air mixtures at engine relevant conditions”, Spectrochim. Acta Part B At. Spectrosc. 148 (2018) 152–164. doi:10.1016/j.sab.2018.06.013.
- L. Merotto, T. Kammermann, D. Bleiner, and P. Soltic, “Ignition Diagnostics based on Spark-Induced Breakdown Spectroscopy for Gas-Engine Applications”, in: International Conference on Ignition Systems for Gasoline Engines, Berlin, 6-7 Dec. 2018, 2018.
- M. Banholzer, M. Pfitzner, D. Sakellarakis, Y. Wright, W. Vera-Tudela, K. Boulouchos, “Numerical investigation of nozzle-geometry variations and back-pressure changes on high-pressure gas injections under application-relevant conditions", SAE World Congress 2018 – Detroit, U.S.A., SAE Technical Paper Nº 2018-01-1138.
- D. Sakellarakis, M. Banholzer, D. Llugaliu, Y.M. Wright, M. Pfitzner and K. Boulouchos: “Assessment Of Real-Gas Effects In High-Pressure Gas Injection At Engine-Relevant Conditions”, proceedings of the 12th ERCOFTAC Symposium on Engineering Turbulence Modelling and Experiments (ETMM), Montpellier, France, 26th – 28th September 2018

8 References

[1] DNV AS, “Maritime Forecast To 2050. Energy Transition Outlook 2021,” p. 118, 2021.

[2] R. Anghilante *et al.*, “Innovative power-to-gas plant concepts for upgrading of gasification bio-syngas through steam electrolysis and catalytic methanation,” *Energy Convers. Manag.*, vol. 183, no. December 2018, pp. 462–473, 2019.

[3] G. Kalghatgi, “Is it really the end of internal combustion engines and petroleum in transport?,” *Appl. Energy*, vol. 225, no. April, pp. 965–974, 2018.

[4] R. D. Reitz *et al.*, “IJER editorial: The future of the internal combustion engine,” *Int. J. Engine Res.*, p. 146808741987799, 2019.

[5] K. Maus, A.-K. Faust, A. Eckmans, M. Wirz, S. Nowak, and C. Alles, “Energy research Masterplan of the Federal Government 2021-2024,” *Fed. Energy Res. Comm. CORE*, 2020.

[6] M. Mittelviefhaus, G. Georges, and K. Boulouchos, “Electrification of multi-energy hubs under limited electricity supply: De-/centralized investment and operation for cost-effective greenhouse gas mitigation,” *Adv. Appl. Energy*, vol. 5, no. October 2021, p. 100083, 2022.

[7] “2020 Gas Vehicles Statistics,” *https://www.ngva.eu/wp-content/uploads/2021/04/NGVA-Europe_PRESS-RELEASE_2020-gas-vehicle-statistics.pdf*, 2021. .

[8] F. Zurbriggen, R. Hutter, and C. Onder, “Diesel-minimal combustion control of a natural gas-diesel engine,” *Energies*, vol. 9, no. 1, 2016.

[9] R. Hutter, J. Ritzmann, P. Elbert, and C. Onder, “Low-Load Limit in a Diesel-Ignited Gas Engine,” *Energies*, vol. 10, no. 10, pp. 1–27, 2017.

[10] P. Soltic, T. Hilfiker, S. Hänggi, R. Hutter, and M. Weissner, “Ignition- and combustion concepts for lean operated passenger car natural gas engines,” in *12. Conference on Gaseous-Fuel Powered Vehicles, October 24-25 2017, Stuttgart*, 2017.

[11] P. Soltic, T. Hilfiker, R. Hutter, and S. Hänggi, “Experimental comparison of efficiency and emission levels of four-cylinder lean-burn passenger car-sized CNG engines with different ignition concepts,” *Combust. Engines*, vol. 176, no. 1, pp. 27–35, Mar. 2019.

[12] P. Soltic, T. Hilfiker, and S. Haenggi, “Efficient light-duty engine using turbulent jet ignition of lean methane mixtures,” *Int. J. Engine Res.*, 2019.

[13] R. Hutter, L. De Libero, P. Elbert, and C. H. Onder, “Catalytic methane oxidation in the exhaust gas aftertreatment of a lean-burn natural gas engine,” *Chem. Eng. J.*, vol. 349, no. January, pp. 156–167, 2018.

[14] T. Kammermann, L. Merotto, D. Bleiner, and P. Soltic, “Spark-Induced Breakdown Spectroscopy for Fuel-Air Equivalence Ratio Measurements at Internal Combustion Engine-Relevant Conditions,” 2019.

[15] L. Merotto, T. Kammermann, and P. Soltic, “Ignition Diagnostics in EGR- and Air-diluted Methane/Air Mixtures Using Spark Induced Breakdown Spectroscopy,” *Combust. Sci. Technol.*, vol. 00, no. 00, pp. 1–16, 2019.

[16] T. Kammermann, L. Merotto, D. Bleiner, and P. Soltic, “Spark-induced breakdown spectroscopy for fuel-air equivalence ratio measurements at internal combustion engine-relevant conditions,” *Spectrochim. Acta Part B At. Spectrosc.*, vol. 155, pp. 79–89, May 2019.

[17] S. Hänggi, J. Frey, S. van Dooren, M. Diehl, and C. Onder, “A Generic Approach for Engine Air Path Control Based on Nonlinear MPC,” *under Rev.*, 2021.

[18] M. Keller *et al.*, “Teaching Nonlinear Model Predictive Control with MATLAB/Simulink and an

Internal Combustion Engine Test Bench," *IFAC-PapersOnLine*, vol. 53, no. 2, pp. 17190–17197, Jan. 2020.

[19] J. B. Rawlings, D. Q. Mayne, and M. M. Diehl, *Model Predictive Control: Theory, Computation, and Design*, 2nd ed., vol. 197. Nob Hill Publishing, LLC, 2019.

[20] Y. M. Wright, O. N. Margari, K. Boulouchos, G. De Paola, and E. Mastorakos, "Experiments and simulations of n-heptane spray auto-ignition in a closed combustion chamber at diesel engine conditions," *Flow, Turbul. Combust.*, vol. 84, no. 1, pp. 49–78, 2010.

[21] K. Boulouchos., O. Margari., A. Escher, G. Barroso, B. Schneider, and S. Kunte, "Optical Diagnostic on Diesel Sprays for the Validation of Computer Aided Simulation," in *6. Internationales Symposium für verbrennungsdiagnostik, Baden-Baden, June 2004*, 2004.

[22] B. Schneider, "Experimentelle Untersuchung zur Spraystruktur in transienten, verdampfenden und nicht verdampfenden Brennstoffstrahlen unter Hochdruck," Swiss Federal Institute of Technology (ETHZ), 2003.

[23] B. Schneider, K. Boulouchos, and B. Ineichen, "Experimental Investigation into Diesel-Sprays under Evaporating and Non-Evaporating Conditions in a High Temperature and High Pressure Cell," in *3rd Meeting of the Greek Section of the Combustion Institute, Patras, 7-8 November*, 2003.

[24] R. S. G. Baert, P. J. M. Frijters, B. Somers, C. C. M. Luijten, and W. de Boer, "Design and Operation of a High Pressure, High Temperature Cell for HD Diesel Spray Diagnostics: Guidelines and Results," *SAE Tech. Pap.*, no. 2009-01–0649, 2009.

[25] S. Iannuzzi, C. Barro, K. Boulouchos, and K. Burger, "Combustion behavior and soot formation/oxidation of oxygenated fuels in a cylindrica constant volume chamber," *Fuel*, vol. 167, pp. 49–59, 2016.

[26] C. Barro, P. Meyer, and K. Boulouchos, "Optical investigation of soot reduction mmechanism using post-injections in a cylindrical constant volume chamber (CCVC)," *SAE Tech. Pap.*, no. 2014-01–2839, 2014.

[27] G. S. Settles, *Schlieren and Shadowgraph Techniques: Visualizing Phenomena in Transparent Media*. Berlin, Germany: Springer-Verlag, 2001.

[28] L. M. Pickett, S. Kook., and T. Williams, "Visualization of diesel spray penetration, cool-flame, ignition, high-temperature combustion, and soot formation using high-speed imaging," *SAE Int. J. Engines*, vol. 2(1), no. 2009-01–0658, pp. 439–459, 2009.

[29] B. Higgins and D. Siebers, "Measurement of the Flame Lift-Off Location on DI Diesel Sprays Using OH Chemiluminescence," *SAE Tech. Pap.*, no. 2001-01–0918, 2001.

[30] S. V. Pancheshnyi, D. A. Lacoste, A. Bourdon, and C. O. Laux, "Ignition of propane-air mixtures by a repetitively pulsed nanosecond discharge," *IEEE Trans. Plasma Sci.*, vol. 34, no. 6, pp. 2478–2487, 2006.

[31] S. M. Starikovskaia and A. Y. Starikovskii, "Plasma-Assisted Ignition and Combustion," in *Handbook of Combustion*, American Cancer Society, 2010, pp. 71–93.

[32] T. Kammermann, W. Kreutner, M. Trottmann, L. Merotto, P. Soltic, and D. Bleiner, "Spark-induced breakdown spectroscopy of methane/air and hydrogen-enriched methane/air mixtures at engine relevant conditions," *Spectrochim. Acta - Part B At. Spectrosc.*, vol. 148, pp. 152–164, 2018.

[33] M. Balmelli *et al.*, "Experimental analysis of breakdown with nanosecond pulses for spark-ignition engines," *IEEE Access*, vol. 9, pp. 100050–100062, 2021.

[34] M. Balmelli *et al.*, "Breakdown of synthetic air under nanosecond pulsed voltages in quasi-

uniform electric fields," *IEEE Access, under Rev.*

[35] M. Balmelli, L. Merotto, and P. Soltic, "Plasma to Early Flame Kernel Transition under Nanosecond Repetitively Pulsed Discharge in an Optical Accessible Pre-chamber," in *5th International Conference on Ignition Systems for Gasoline Engines, Berlin 13th-14th September 2022*, 2022.

[36] R. Verschueren *et al.*, "Towards a modular software package for embedded optimization," in *IFAC-PapersOnLine*, 2018, vol. 51, no. 20, pp. 374–380.

[37] T. Albin, *Nonlinear Model Predictive Control of Combustion Engines*. Springer International Publishing, 2021.

[38] J. Gerold, P. Vogl, and M. Pfitzner, "New correlation of subsonic, supersonic and cryo gas jets validated by highly accurate schlieren measurements," *Exp. Fluids*, vol. 54:1542, 2013.

[39] A. Lozano, B. Yip, and R. K. Hanson, "Acetone: a tracer for concentration measurements in gaseous flows by planar laser-induced fluorescence," *Exp. Fluids*, vol. 13, no. 6, pp. 369–376, 1992.

[40] M. C. Thurber and R. K. Hanson, "Pressure and composition dependences of acetone laser-induced fluorescence with excitation at 248, 266, and 308 nm," *Appl. Phys. B*, vol. 69, no. 3, pp. 229–240, Sep. 1999.

[41] S. Faust, M. Goschütz, S. A. Kaiser, T. Dreier, and C. Schulz, "A comparison of selected organic tracers for quantitative scalar imaging in the gas phase via laser-induced fluorescence," *Appl. Phys. B*, vol. 117, no. 1, pp. 183–194, 2014.

[42] L. Merotto, M. Balmelli, W. Vera-Tudela, and P. Soltic, "Comparison of ignition and early flame propagation in methane/air mixtures using nanosecond repetitively pulsed discharge and inductive ignition in a pre-chamber setup under engine relevant conditions," *Combust. Flame*, vol. 237, p. 111851, 2022.

[43] M. Castela, B. Fiorina, A. Coussement, O. Gicquel, N. Darabiha, and C. O. Laux, "Modelling the impact of non-equilibrium discharges on reactive mixtures for simulations of plasma-assisted ignition in turbulent flows," *Combust. Flame*, vol. 166, pp. 133–147, 2016.

[44] R. Maly, "Spark Ignition: Its Physics and Effect on the Internal Combustion Engine.," in *Fuel Economy*, H. J.C. and S. G.S., Eds. Springer, Boston, MA, 1984, pp. 91–148.

[45] W. Vera-Tudela, L. Merotto, M. Balmelli, and P. Soltic, "Experimental study of the ignition of lean methane / air mixtures using inductive and NRPD ignition systems in the pre-chamber and turbulent jet ignition in the main chamber," *Energy Convers. Manag.*, no. in press, p. 115012, 2021.

[46] W. Vera-Tudela, C. Barro, and K. Boulouchos, "Investigations on spark pre-chamber ignition and subsequent turbulent jet main chamber ignition in a novel optically accessible test rig," *Int. J. Engine Res.*, pp. 1–13, 2021.

[47] P. G. Hill and P. Ouellette, "Transient turbulent gaseous fuel jets for diesel engines," *J. Fluids Eng. Trans. ASME*, vol. 121, no. 1, pp. 93–101, 1999.

[48] R. A. Fraser, D. L. Siebers, and C. F. Edwards, "Autoignition of Methane and Natural Gas in a Simulated Diesel Environment," in *SAE Technical Paper*, 1991.

[49] T. ISHIYAMA, M. SHIOJI, T. IHARA, T. INOUE, and N. TAKADA, "Characteristics of Spontaneous Ignition and Combustion in Unsteady High-Speed Gaseous Fuel Jets," in *SAE Technical Paper*, 2003.

[50] J. Huang, P. G. Hill, W. K. Bushe, and S. R. Munshi, "Shock-tube study of methane ignition under engine-relevant conditions: Experiments and modeling," *Combust. Flame*, vol. 136, no.

1–2, pp. 25–42, 2004.